

Title	グラフェン-グラフェンナノ電子機械スイッチデバイスの研究
Author(s)	Kulothungan, Jothiramalingam
Citation	
Issue Date	2017-12
Type	Thesis or Dissertation
Text version	ETD
URL	http://hdl.handle.net/10119/15079
Rights	
Description	Supervisor:水田 博, マテリアルサイエンス研究科, 博士

Doctoral Dissertation

Graphene-to-Graphene
Nanoelectromechanical (NEM) Switching
Devices

Kulothungan Jothiramalingam

Supervisor: Prof. Hiroshi Mizuta

School of Materials Science

Japan Advanced Institute of Science and Technology

December 2017

DECLARATION

I, Kulothungan Jothiramalingam, hereby declare that this thesis, which is submitted for the assessment of my research leading to the degree of Doctor of Philosophy, entirely originated from my own study. It includes nothing, which is taken from the work completed by other researchers without proper citation and acknowledgment. This thesis has not been previously submitted, in part or whole, to any University of the institution for any degree, diploma, or other qualification.

Signed: _____

Date: _____

Kulothungan Jothiramalingam

Japan Advanced Institute of Science and Technology

ABSTRACT

Energy and Environment Research Division

School of Material Science

Mizuta Laboratory

Doctor of Philosophy

Graphene-to-Graphene Nanoelectromechanical Switching Devices

BY KULOTHUNGAN JOTHIRAMALINGAM

The Nanoelectromechanical (NEM) contact switches can offer low leakage current, abrupt switching and high ON/OFF ratio. Due to these superior characteristics, NEM contact switch has become one of the demanding candidate to overcome the limitations, such as high off-state power consumption, of conventional CMOS technology. Conventional NEM contact switches exhibit disadvantages such as high pull-in voltage, and interfacial stiction. One of the most promising materials to overcome the demerits of conventional for the NEM contact switch is graphene. Graphene, a single layer of a carbon atom, has excellent electrical and mechanical property. The graphene based NEM contact switches can offer low pull-in voltage switch for ultra-low power application and can also achieve abrupt subthreshold swing ($SS < 60 \text{mV/dec}$).

The graphene based NEM contact switch is facing contact adhesion problems as the suspended graphene beam is struck to the metal contact surface (Au, Cr/Cr₂O₃) after the pull-in operation. The gold and the carbon atoms form the chemical bonding, and this leads to the stiction of the graphene in the gold surface. In addition, the amorphous and disordered surface of the Cr/Cr₂O₃ also leads to the highly uncontrolled pull-out operation and subsequently results the stiction of the graphene beam to the surface of Chromium oxide Cr₂O₃ contact.

The aim of this study is to achieve clear pull-in and pull-out operation of the graphene based NEM contact switches. To avoid the direct contact between the graphene to metal, a graphene layer is used as the contact material. The suspended graphene can contact with the contact graphene layer in the pulled-in state. The graphene is used as the anti-stiction material to reduce the stiction.

At first, in order to study the structural dimension graphene NEM contact switches, we conducted the Finite Element Method (FEM) based simulation of doubly clamped graphene based NEM contact switches. Firstly, we performed the FEM simulation of the switch with dimensions adapted from our earlier experimental device, based on nanocrystalline graphene (NCG). The results obtained in FEM simulations are consistent with the experimental results. Based on this, the FEM simulation for graphene NEM contact switches are carried out. Pull-in and Pull-out characteristics are analyzed for graphene NEM contact switches with different dimensions. This numerical model is used to study the scaling nature of the graphene NEM contact switches. We have found out the structural dimensions to achieve the possibility of sub-5 V and sub-1V graphene NEM contact switches.

We studied the interlayer resistance between the two graphene layers to understand the static graphene-graphene contact characteristics. Incoherent conduction between the graphene layers has observed. Interlayer tunneling between the two graphene layers is the fundamental conduction mechanism. We have studied the effect of in-situ annealing on the interlayer conduction. The interlayer resistance shows the significant reduction after the in-situ annealing. The interlayer resistance values at low temperature (5 K) is 4.8 k Ω and 800 Ω for before and after the in-situ annealing, respectively. This is attributed to the decrease in the interlayer distance after in-situ annealing.

Finally, we succeeded to demonstrate a graphene-to-graphene NEM contact switches with clear pull-in/pull-out characteristics. We achieved a graphene-to-graphene NEM contact switch with low pull-in voltage of <1 V, the steep switching slope of <10 mV/dec and high ON/OFF ratio >10⁵. Owing to the high restoring force double clamped graphene beam the clear pull-out was achieved. And we have demonstrated the switches with more than 15 switching cycles. Due to the smooth atomic level contact between graphene-graphene layers, these remarkable graphene NEM characteristics were achieved.

Keywords: NEM contact switches, Graphene, Stiction, contact adhesion, Interlayer resistance, Interlayer tunneling, Twisted bilayer graphene, Finite Element Simulation (FEM).

ACKNOWLEDGEMENTS

First and foremost, I would like to thank my supervisor Prof. Hiroshi Mizuta who has supported me throughout the PhD course. Without the fruitful discussions and good advice, I would not have been able to spend such successful years in JAIST. He gave me a lot of freedom to peruse the research the way I want to do. I am very grateful for the recommendation of MEXT scholarship. It has been such great honor to be the part of his lab. I believe I have learned a lot being his student. His help with correcting my thesis was very helpful.

I also would like to thank, Dr. Manoharan Muruganathan, for his support throughout my PhD course. It is a great privilege to be his student. It is impossible to express thanks to him in words; there is a countless number of occasions that he helped me to accomplish a life here in JAIST. I would like to thank him wholeheartedly for all his efforts that he makes for the betterment of my life. I also would like to extend my sincere thanks to him for his first interview and for the recommendation of MEXT scholarship. His help with correcting my thesis was very beneficial.

Besides my supervisors, I would like to acknowledge all the Ph.D. qualification committee members, Professor Eisuke Tokumitsu, Professor Mikio Koyano, Professor Yoshifumi Oshima, and Professor Hitoshi Wakabayashi (Tokyo Institute of Technology) for their insightful comments and encouragement, which helps me to widen my research from various perspectives.

For his assistance in my research, I want to thank Dr. Marek E Schmidt, who provided me a lot of hope to do research, clean room training, mastering the techniques to do a real fabrication. Out of all, I want to thank him for sharing his stories with Lina Schmidt as a father. “Your fatherhood is one of the true sources that inspire me to pursue a normal life. You are one of the best things that happen to me here in JAIST, and the only thing that I would like to carry forever and ever. Thank you, Marek”.

Without the help of Hammam, the successful work on the Nano-fab would not have been possible. Also, the patience and support of Wenzhen Wang in the clean room was invaluable. Additionally, without any particular order, I want to thank Takuya Iwasaki, Shunei Suzuki, Wang Zhongwang, Huynh Van Ngoc, Takuo Chikuba, Nozomu Kanatake, Ohta Takachi, Le The Anh, and Jian Sun, for their help.

Also, I would like to thank all the lab members of Mizuta lab, who are behind me and giving me tremendous support.

Last but not the least; I want to thank my Japanese teacher, Akiko Takizawa, for her support.

CONTENTS

1	INTRODUCTION.....	19
1.1	MOORE'S LAW AND CMOS LIMITATIONS	19
1.1.1	<i>The energy efficiency limit of the CMOS</i>	<i>21</i>
1.2	NANO-ELECTRO-MECHANICAL SWITCHING: STATE OF THE ART	23
1.2.1	<i>Operating Principle of mechanical switching</i>	<i>23</i>
1.3	GRAPHENE	26
1.3.1	<i>Electrical properties of graphene</i>	<i>26</i>
1.3.2	<i>Mechanical properties of graphene</i>	<i>27</i>
1.4	REVIEW OF THE RECENT LITERATURE.....	27
1.5	THE PURPOSE OF THIS STUDY	29
1.6	THESIS STRUCTURE.....	30
2	ESSENTIAL THEORY OF NEM CONTACT SWITCHES.....	32
2.1	INTRODUCTION	32
2.2	ELECTROMECHANICAL ANALYSIS.....	33
2.2.1	<i>Pull-in analysis</i>	<i>33</i>
2.2.2	<i>The equilibrium position of the electrostatic actuator with applied bias.</i>	<i>35</i>
2.2.3	<i>Pull-out analysis</i>	<i>36</i>
3	FINITE ELEMENT METHOD (FEM) SIMULATION OF GRAPHENE BASED NANO-ELECTROMECHANICAL SWITCHES	39
3.1	INTRODUCTION	39
3.2	INTRODUCTION TO FINITE ELEMENT METHOD SIMULATION	40
3.2.1	<i>Meshing.....</i>	<i>40</i>
3.2.2	<i>Mechanical Meshing</i>	<i>41</i>
3.2.3	<i>Electrostatic Meshing</i>	<i>41</i>
3.2.4	<i>ThermoElectroMechanical coupling.....</i>	<i>42</i>
3.2.5	<i>The governing equations for Finite Element Method (FEM) simulation.</i>	<i>42</i>
3.3	FINITE ELEMENT METHOD SIMULATION OF GRAPHENE BASED NEM CONTACT SWITCHES	43
3.3.1	<i>Introduction.....</i>	<i>43</i>
3.3.2	<i>Description of the device geometry.....</i>	<i>44</i>
3.3.3	<i>Graphene NEM switch pull-in and pull-out characteristics.....</i>	<i>46</i>

3.3.4	<i>von Mises stress analysis</i>	48
3.3.5	<i>3D electric field distributions and its role in graphene beam NEM switch operation</i>	49
3.4	CHAPTER SUMMARY.....	52
4	FABRICATION OF GRAPHENE-TO-GRAPHENE NANOELECTROMECHANICAL SWITCHING DEVICES	53
4.1	INTRODUCTION.....	53
4.2	SAMPLE PREPARATION	54
4.2.1	<i>Cleaning the CVD graphene</i>	54
4.3	FABRICATION OF GRAPHENE-TO-GRAPHENE NEM CONTACT SWITCH	55
4.3.1	<i>Fabrication of address pattern</i>	55
4.3.2	<i>Patterning of the graphene ribbon</i>	57
4.3.3	<i>Fabrication of contact electrodes</i>	58
4.3.4	<i>Deposition of SiO₂ as a sacrificial layer</i>	59
4.3.5	<i>Transferring top graphene layer</i>	59
4.3.6	<i>Patterning the top graphene layer</i>	60
4.3.7	<i>Fabrication of the top contact electrodes</i>	61
4.3.8	<i>Releasing the sacrificial layer (SiO₂) using the BHF</i>	61
4.4	SUMMARY	63
5	GRAPHENE CROSSBAR DEVICE CHARACTERISATION	64
5.1	INTRODUCTION.....	64
5.2	INTRODUCTION TO CROSSBAR DEVICE.....	65
5.3	FABRICATION OF GRAPHENE CROSSBAR DEVICE.....	65
5.4	RAMAN SPECTROSCOPY OF CROSSBAR DEVICE	66
5.5	ELECTRICAL CHARACTERISATION OF CROSSBAR DEVICE.....	67
5.5.1	<i>Measurement configuration of the crossbar device</i>	67
5.5.2	<i>Results and discussion.</i>	69
5.6	SUMMARY	76
6	GRAPHENE-TO-GRAPHENE NEM CONTACT SWITCH: CHARACTERIZATION AND ANALYSIS	77
6.1	INTRODUCTION.....	77
6.2	DEVICE STRUCTURE AND DIMENSION	78
6.3	RESULTS AND DISCUSSION	79
6.3.1	<i>Pull-in characterization</i>	79
6.3.2	<i>Statistical analysis of the Pull-in voltage</i>	83

6.3.3	<i>Pull-in voltage variation in the different devices with similar structural dimension.</i>	86
6.3.4	<i>Fluctuation in the pull-in and pull-out voltages in different cycles of switch.</i>	89
6.3.5	<i>Sub 1-V graphene NEM contact switch</i>	89
6.3.6	<i>Pull-out characterisation</i>	91
6.4	CHAPTER SUMMARY	95
7	CONCLUSION AND FUTURE WORK	96
7.1	CONCLUSION	96
7.2	FUTURE WORKS	97
8	REFERENCES	99

LIST OF TABLES

TABLE 3.1. NEM SWITCH DIMENSIONS	45
TABLE 6.1. DEVICE PARAMETERS OF NINE MEASURED G_G NEM CONTACT SWITCHES. .	79
TABLE 6.2. STATISTICAL ANALYSIS OF THE PULL-IN VOLTAGES OF ALL DEVICES.....	84
TABLE 6.3. SUMMARY OF ELECTRICAL CHARACTERIZATION OF ALL THE DEVICES.....	85
TABLE 6.4. MISALIGNMENT INDUCED PULL-IN VOLTAGE VARIATION.....	88

LIST OF FIGURES

- FIGURE 1.1 EVOLUTION OF MICROELECTRONICS DEVICES SINCE THE TIME OF FIRST INTEGRATED CIRCUITS IN 1958. ON THE LEFT Y-AXIS, THE NUMBER OF TRANSISTORS PER CHIP, AND THEIR CRITICAL DIMENSION (GATE LENGTH) (RIGHT-HAND SIDE) ARE REPORTED. 20
- FIGURE 1.2. THE TREND OF POWER CONSUMPTION WITH CMOS SCALING. REPRODUCED FROM (WITHOUT PERMISSION) [2] 20
- FIGURE 1.3. (A) SCHEMATIC OF THE SUBTHRESHOLD SLOPE OF CMOS DEVICE. (B) EFFECT OF SCALING IN THE CMOS DEVICE. I_{OFF} ' IS AN INCREASED DRAIN CURRENT AS A RESULT OF THE GATE SCALING. 22
- FIGURE 1.4. (A) THE INITIAL STRUCTURE OF THE NEM CONTACT SWITCH (DOUBLE CLAMPED BEAM STRUCTURE IS SHOWN). (B) NEM CONTACT SWITCH IS IN ON STATE. 24
- FIGURE 1.5. AN OUTPUT CHARACTERISTIC OF THE NEM CONTACT SWITCHES (A) PULL-IN/PULL-OUT CURVES IN THE REGARDING DISPLACEMENT. (B) PULL-IN/PULL-OUT CURVES IN THE REGARDING MEASUREMENT. 25
- FIGURE 1.6. COMPARISON OF OUTPUT CHARACTERISTICS. (A) SWITCHING CHARACTERISTICS OF NEM CONTACT SWITCH WITH CMOS SWITCH (THE BLUE CURVE IS FOR CONVENTIONAL CMOS, THE RED CURVE IS FOR NEM CONTACT SWITCHING). (B) ILLUSTRATING THE BOTH NEM CONTACT SWITCH CMOS SWITCH IN THE SAME FRAME. 25
- FIGURE 1.7 UTILIZING GRAPHENE TO BUILD ALL-DIMENSIONAL CARBON MATERIALS. 26
- FIGURE 2.1. 1D PARALLEL PLATE MODEL OF NEM CONTACT SWITCH. 33
- FIGURE 2.2. SCHEMATIC EXPLANATION OF THE EQUILIBRIUM MECHANICAL AND ELECTROSTATIC FORCE. 35
- FIGURE 2.3. SCHEMATIC EXPLANATION OF THE EQUILIBRIUM MECHANICAL AND ELECTROSTATIC FORCE AT PULL-IN CONDITION. 36
- FIGURE 2.4. 1D PARALLEL PLATE MODEL TO CALCULATE THE VOLTAGE OF PULL-OUT EFFECT. 37
- FIGURE 3.1. SCHEMATIC OF DOUBLE-CLAMPED GRAPHENE BEAM NEM SWITCH WITH TOP METAL ACTUATION ELECTRODE. 46

FIGURE 3.2. THE GEOMETRY OF NEM SWITCH A. (A) INITIAL STRUCTURE OF DOUBLE-CLAMPED GRAPHENE BEAM NEM SWITCH WITH A TOP METAL ELECTRODE. (B) PULLED-IN STATE OF THE GRAPHENE BEAM; COLOR BAR INDICATES THE RELATIVE DISPLACEMENT WITH RESPECT TO THE INITIAL CONDITION. 47

FIGURE 3.3. PULL-IN/PULL-OUT SWITCHING CHARACTERISTICS OF THE DOUBLE-CLAMPED GRAPHENE BEAM NEM SWITCHES. (A) SWITCHING CHARACTERISTICS OF GRAPHENE BEAM NEM SWITCHES A, B, AND C. (B) SWITCHING CHARACTERISTICS OF GRAPHENE BEAM NEM SWITCH A, WITH DIFFERENT GRAPHENE THICKNESS OF $T = 3$ NM, 5 NM, AND 9 NM. 47

FIGURE 3.4. VON MISES STRESS OF DOUBLE-CLAMPED GRAPHENE BEAM NEM SWITCHES. (A) VON MISES STRESS OF GRAPHENE NEM SWITCHES A, B, AND C. (B) VON MISES STRESS OF GRAPHENE BEAM NEM SWITCH A, WITH DIFFERENT GRAPHENE THICKNESSES OF $T = 3$ NM, 5 NM, AND 9 NM. 48

FIGURE 3.5. CONTOUR PLOT (TOP VIEW OF GRAPHENE BEAM) OF VON MISES STRESS FOR THE NEM SWITCH A, WITH DIFFERENT GRAPHENE BEAM THICKNESSES OF $T = 3$ NM, 5 NM, AND 9 NM. 49

FIGURE 3.6. 2D ELECTRIC FIELD DISTRIBUTION ACROSS THE CENTER OF THE NEM SWITCH. DIMENSIONS OF THE GRAPHENE BEAM (TOP ELECTRODE) ARE EQUIVALENT TO THOSE OF THE NEM SWITCH A. (A) THE ELECTRIC FIELD DISTRIBUTION ACROSS THE SWITCH AT THE CENTER OF THE BEAM. ARROWS INDICATE THE ELECTRIC FIELD DIRECTION. (B) THE ELECTRIC FIELD STRENGTH IN THE Z DIRECTION AT 5 NM ABOVE THE BOTTOM ELECTRODE AT DIFFERENT VOLTAGES APPLIED BETWEEN THE BOTTOM AND TOP ELECTRODES. THE INSET SHOWS ZOOMED-IN VERSION OF ELECTRIC FIELD DISTRIBUTION FOR LOWER ACTUATION VOLTAGES AS INDICATED BY THE DASHED BOX; THE SCALE IS SAME AS (B). 50

FIGURE 3.7. EFFECT OF THE BEAM EDGE ELECTRIC FIELD TERMINATION AT 8.3 V. (A) THE DISPLACEMENT OF THE BEAM AT 8.3 V SHOWN AS A SIDE VIEW. (B) THE DISPLACEMENT OF THE BEAM FROM AN INITIAL POSITION AT DIFFERENT APPLIED VOLTAGES. BIRDS-EYE CROSS SECTIONAL VIEW OF THE GRAPHENE BEAM AT (C) 0.1 V, (D) 1 V, AND (E) 8.3 V. 51

FIGURE 4.1 (A) AND (B) OPTICAL MICROSCOPY IMAGES OF CVD GRAPHENE SAMPLE FROM GRAPHENE PLATFORM. (C) A RAMAN SPECTRUM COLLECTED FROM ONE OF OUR CVD SAMPLES. 54

FIGURE 4.2. CVD GRAPHENE ON Si/SiO ₂ SUBSTRATE.	57
FIGURE 4.3. PATTERNED GRAPHENE RIBBON.	57
FIGURE 4.4. FABRICATION OF GOLD ELECTRODES. (A) SCHEMATIC ILLUSTRATION OF THE GOLD ELECTRODE FABRICATION. (B) OPTICAL MICROSCOPE OF THE DEVICE AFTER THE GOLD ELECTRODE FABRICATION.	58
FIGURE 4.5. DEPOSITION OF SiO ₂ LAYER.	59
FIGURE 4.6. TRANSFERRED THE TOP GRAPHENE LAYER.	60
FIGURE 4.7. PATTERN THE TOP GRAPHENE LAYER.	60
FIGURE 4.8. FABRICATION OF TOP ELECTRODES. (A) SCHEMATIC OF THE DEVICE STRUCTURE AFTER THE TOP ELECTRODE FABRICATION. (B) OPTICAL MICROSCOPE IMAGE OF THE DEVICE.	61
FIGURE 4.9. SUSPENDED GRAPHENE RIBBON AFTER THE BHF RELEASE.	62
FIGURE 5.1. SCHEMATIC OF FABRICATION FLOW OF THE GRAPHENE-TO-GRAPHENE CROSSBAR DEVICE.	66
FIGURE 5.2. (A) RAMAN SPECTROSCOPY OF THE GRAPHENE CROSSBAR DEVICE. (B) 2D PEAK SHIFT OF THE GRAPHENE CROSS BAR DEVICE (COMPARED WITH THE SINGLE LAYER GRAPHENE SLG).	67
FIGURE 5.3. ELECTRICAL MEASUREMENT CONFIGURATION OF THE INTERLAYER RESISTANCE MEASUREMENT SETUP.	68
FIGURE 5.4. EQUIVALENT CIRCUIT MODEL OF CROSS JUNCTION DEVICE. (A) IDEAL CIRCUIT. (B) REAL CIRCUIT	68
FIGURE 5.5. BACK GATE CHARACTERISTICS OF THE GRAPHENE CROSSBAR DEVICE. (A) BOTTOM GRAPHENE RIBBON. (B) TOP GRAPHENE RIBBON.	69
FIGURE 5.6. BACK GATE CHARACTERISTICS OF THE GRAPHENE CROSSBAR DEVICE AFTER VACUUM ANNEALING. (A) BOTTOM GRAPHENE RIBBON. (B) TOP GRAPHENE RIBBON.	70
FIGURE 5.7. BACK GATE CHARACTERISTICS OF THE GRAPHENE CROSSBAR DEVICE AFTER HYDROGEN ANNEALING. (A) BOTTOM GRAPHENE RIBBON. (B) TOP GRAPHENE RIBBON.	70

FIGURE 5.8. TEMPERATURE DEPENDENCE BACK GATE CHARACTERISTICS OF THE GRAPHENE CROSSBAR DEVICE AS FABRICATED. (A) BOTTOM GRAPHENE RIBBON. (B) TOP GRAPHENE RIBBON.	71
FIGURE 5.9 TEMPERATURE DEPENDENCE BACK GATE CHARACTERISTICS OF THE GRAPHENE CROSSBAR DEVICE AFTER THE IN-SITU ANNEALING PROCESS. (A) BOTTOM GRAPHENE RIBBON. (B) TOP GRAPHENE RIBBON.	71
FIGURE 5.10. INTERLAYER RESISTANCE AS A FUNCTION OF THE BACKGATE VOLTAGE. (A) THE INTERLAYER RESISTANCE OF THE GRAPHENE CROSSBAR DEVICE FOR THE AS FABRICATED SAMPLE. (B) INTERLAYER RESISTANCE AFTER THE IN-SITU ANNEALING.	72
FIGURE 5.11. INTERLAYER RESISTANCE AS A FUNCTION OF THE TEMPERATURE.	72
FIGURE 5.12. SCHEMATIC DIAGRAM OF THE TEMPERATURE DEPENDENCE OF THE INTERLAYER CONDUCTION MECHANISM.	73
FIGURE 5.13. SCHEMATIC DIAGRAM OF INTERLAYER CONDUCTION. (A) METAL-INSULATOR-METAL MODEL OF INTERLAYER TRANSPORT. (B) THE EFFECT OF IN-SITU ANNEALING IN THE INTERLAYER TRANSPORT.	74
FIGURE 5.14. (A) INTERLAYER RESISTANCE IN THE $Ar+H_2$ GAS ENVIRONMENT. (B) INTERLAYER RESISTANCE AS A FUNCTION OF THE TEMPERATURE IN THE $Ar+H_2$ GAS ENVIRONMENT.	75
FIGURE 6.1. SCHEMATIC DIAGRAM OF THE GRAPHENE-TO-GRAPHENE TO NEM CONTACT SWITCH. THE INSET SHOWS THE FIXED GOLD ELECTRODE WITH GRAPHENE AS THE CONTACT MATERIAL.	78
FIGURE 6.2. (A) AFM IMAGE OF THE DEVICE D1. (B) SEM IMAGE OF THE DEVICE D1.	78
FIGURE 6.3. TWO TERMINAL ELECTRICAL MEASUREMENT CONFIGURATION.	80
FIGURE 6.4. TYPICAL SWITCHING CHARACTERISTICS OF THE GRAPHENE-TO-GRAPHENE NEM CONTACT SWITCH. (FIRST SWITCHING CYCLE OF DEVICE D1)	80
FIGURE 6.5. SWITCHING CHARACTERISTICS OF GRAPHENE-TO-GRAPHENE NEM CONTACT DEVICE (DEVICE D1 TO D6 IS SHOWN)	81
FIGURE 6.6. SWITCHING CHARACTERISTICS OF GRAPHENE-TO-GRAPHENE NEM CONNECT THE DEVICE (DEVICE D7 TO D9 IS SHOWN).	82
FIGURE 6.7. STATISTICAL AVERAGE OF THE PULL-IN VOLTAGE FOR DEVICE D1-D6.	83

FIGURE 6.8. STATISTICAL AVERAGE OF THE PULL-IN VOLTAGE FOR DEVICE D7-D9.	84
FIGURE 6.9. SUMMARY OF THE DEVICE D1- D9. (A) PULL-IN VOLTAGE AND THE SWITCHING CYCLE OF THE DEVICES FROM D1 TO D9. (B) THE SWITCHING VOLTAGE WINDOW OF THE DEVICES FROM D1 TO D9.	86
FIGURE 6.10. (A-F) SEM IMAGES OF THE DIFFERENT DEVICES WITH A MISALIGNMENT INDUCED SHIFT IN THE ACTUATION ELECTRODE. (D-F) SCHEMATIC REPRESENTATION OF THE ACTUATION ELECTRODE SHIFT IN DIFFERENT DEVICES.	87
FIGURE 6.11. THE GEOMETRY OF NEM SWITCH A. (A) INITIAL STRUCTURE OF DOUBLE-CLAMPED GRAPHENE BEAM NEM SWITCH WITH A TOP METAL ELECTRODE. (B) PULLED-IN STATE OF THE GRAPHENE BEAM; COLOR BAR INDICATES THE RELATIVE DISPLACEMENT WITH RESPECT TO THE INITIAL CONDITION.	88
FIGURE 6.12. SWITCHING CHARACTERISTICS OF THE GRAPHENE NEM CONTACT SWITCH WITH DIFFERENT MISALIGNMENT.	88
FIGURE 6.13. (A) SWITCHING CHARACTERISTICS OF THE DEVICE D9. THE PULL-OUT VOLTAGE FLUCTUATION OF THE DEVICE D9.	89
FIGURE 6.14. (A) AFM IMAGE OF THE GRAPHENE RIBBON WITH SiO ₂ DEPOSITION. (B) AFM LINE PROFILE OF THE AFTER SiO ₂ DEPOSITION.	90
FIGURE 6.15. SWITCHING CHARACTERISTICS OF THE SUB 1-V SWITCH. (A) SWITCH WITH PULL-IN VOLTAGE OF 0.92 V. (B) SWITCH WITH PULL-IN VOLTAGE OF 0.8 V.	90
FIGURE 6.16. SURFACE ADHESION IN GRAPHENE- GOLD SURFACE. (A) GRAPHENE BEAM IS PULLED ON TO THE SURFACE OF THE GOLD. (B) PULL-IN CHARACTERISTICS OF THE NEM CONTACT SWITCH WITH AU AS CONTACT MATERIAL. (B) TYPICAL PULL OUT CHARACTERISTICS OF THE PULL-OUT IN THE NEM CONTACT SWITCH WITH AU AS THE CONTACT MATERIAL.	91
FIGURE 6.17. SURFACE ADHESION IN GRAPHENE- Cr ₂ O ₃ SURFACE. (A) GRAPHENE BEAM IS PULLED ON TO THE SURFACE OF THE Cr ₂ O ₃ . (B) PULL-IN CHARACTERISTICS OF THE NEM CONTACT SWITCH WITH Cr ₂ O ₃ AS CONTACT MATERIAL. (B) TYPICAL PULL OUT CHARACTERISTICS OF THE PULL-OUT IN THE NEM CONTACT SWITCH WITH Cr ₂ O ₃ AS THE CONTACT MATERIAL.	92
FIGURE 6.18. SURFACE ADHESION IN THE GRAPHENE-GRAPHENE SURFACE. (A) GRAPHENE BEAM IS PULLED ONTO THE SURFACE OF THE GRAPHENE. (B) PULL-IN CHARACTERISTICS OF THE NEM CONTACT SWITCH WITH GRAPHENE AS CONTACT	

1 Introduction

1.1 MOORE'S LAW AND CMOS LIMITATIONS

Complementary Metal Oxide Semiconductor (CMOS) technology has been miniaturized to nano scale according to Moore's law [1]. The Moore's law expressed that, the number of transistors in a silicon integrated circuit (IC) increased to twice the quantity for every 18 months and also the gate length of the MOS transistor reduced to half [2]. Figure 1.1 illustrates the number of transistor per processor chip vs. year. It is evident from the Figure 1.1; the scaling is in good agreement with Moore's law. The CMOS scaling gradually improves the performance of the Very Large Scale Integration (VLSI) circuits and systems [3]. However, the CMOS scaling introduces the heat dissipation problem. The amount of heat released from the IC has been increased with the CMOS scaling. The heat dissipation is critical issue. The heat dissipation problem is difficult to solve with scaling. It is Because of the subthreshold swing, how sharply the drain current drops with the applied gate voltage, of the Metal-oxide-semiconductor field effect transistor (MOSFET). The slope of the subthreshold swing is limited to 60 mV/dec at 300K [4]. It is exceptionally hard proportional down the drain voltage V_D less than sub 1 V while expanding the speed of the MOSFET and keeping the power dissipation in very low range. Scaling is difficult without reducing the applied voltage because the charge control is difficult. The reduction of the channel length gives rise to unwanted short-channel effects (SCE). When the length of channel is shortened, drain bias affects the channel potential than the long channel device. Due to this channel bias, the potential barrier is reduced, this phenomenon is called drain-induced barrier lowering (DIBL). To effectively control short channel device by the gate, thinner gate oxides are needed. For 65 nm node CMOS process technology, the

thickness of the gate oxide is only 1.2 nm. Moreover, band-to-band tunneling occurs because of drastically reducing gate oxide to low thickness, which upsurges the gate leakage. For MOSFET with 40 nm gate length, the leakage power dissipation has tantamount to dynamic power dissipation, Figure 1.2, displays the off-state leakage power and the dynamic power with scaling [5].

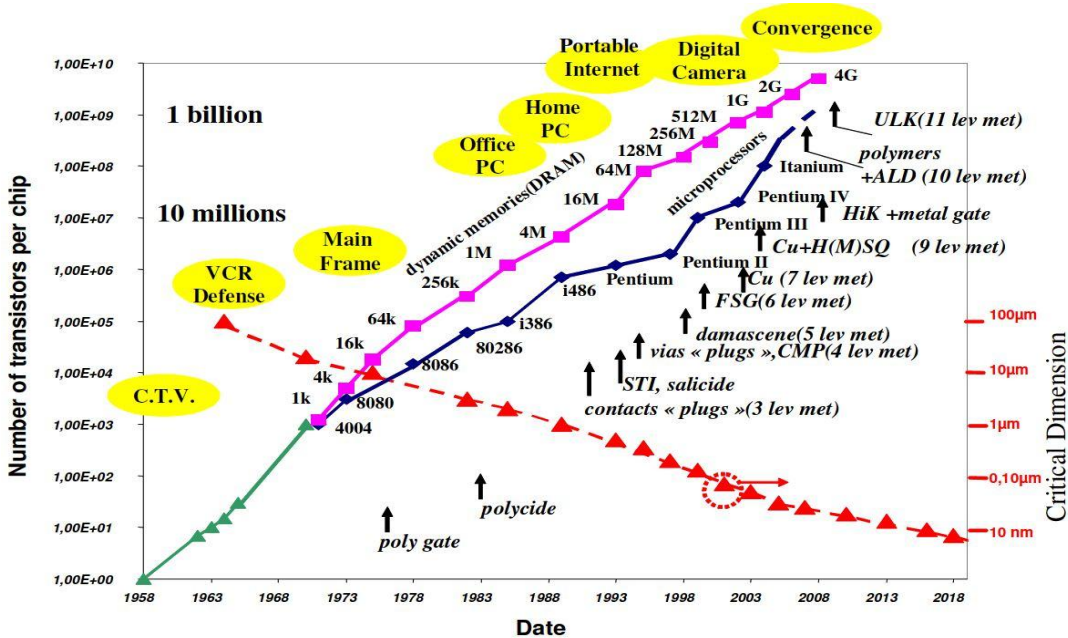


Figure 1.1 Evolution of microelectronics devices since the time of first integrated circuits in 1958. On the left Y-axis, the number of transistors per chip, and their critical dimension (gate length) (right-hand side) are reported.

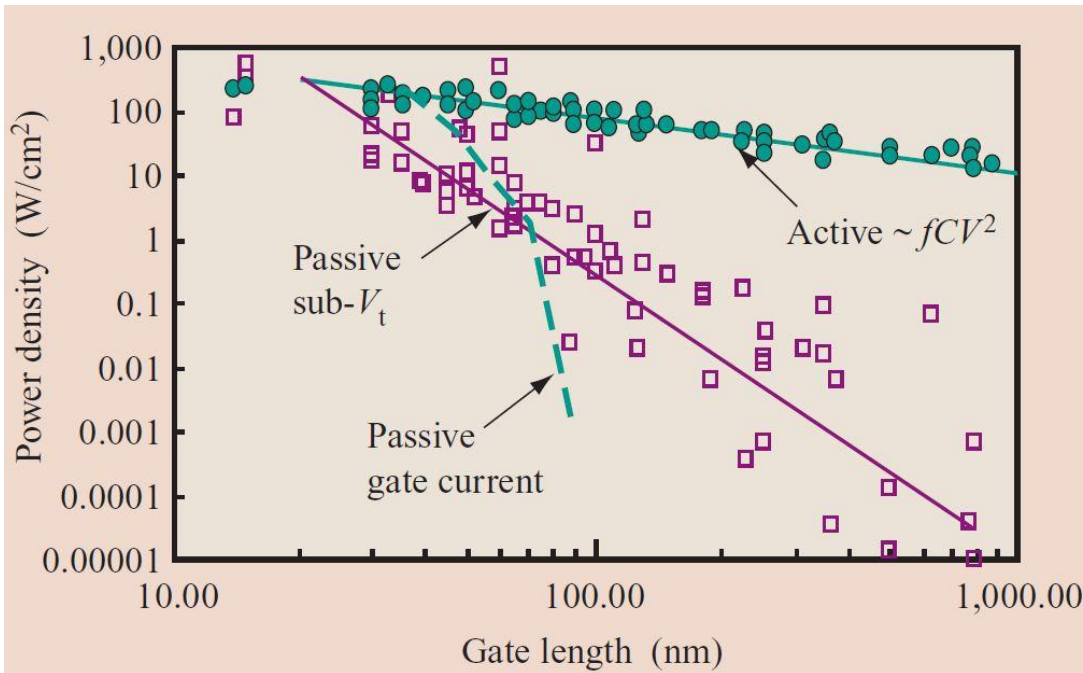


Figure 1.2. The trend of Power consumption with CMOS scaling. Reproduced from (without permission) [2]

1.1.1 THE ENERGY EFFICIENCY LIMIT OF THE CMOS

The MOSFET is the fundamental functional unit of the VLSI Integrated Circuits (IC's). The MOSFET is an active device. The active device has three terminals. There is source terminal, drain terminal and the gate. The channel is formed between the source and drain terminal. The current flow in the channel is controlled by the gate. The potential barrier is shaped between the source and drain interface in the off state. The current flow in the channel is caused by the diffusion of charge carriers. The height of the potential barrier determines a number of charge carriers that flow through the channel. The drain collects the mobile charge carriers. By controlling the gate voltage, height of the potential barrier is modulated, which controls the current moving over the channel [6].

The current that flows through the channel of the MOSFET is referred as the drain current (I_D). The transfer characteristic of a MOSFET is shown in Figure 1.3. The applied gate voltage (V_G) increased beyond the threshold voltage (V_{TH}), the height of the potential barrier is reduced. Once the potential barrier is reduced, then charge carriers freely maneuver from the source into the channel area. In the on case, mobile charge carriers make the conductive path along the channel region. The drift in the state channel limits the current flow through the channel. The following equation gives the on-current (I_{ON}) of a long-channel MOSFET:

$$I_{ON} = \mu_{eff} C_{ox} \frac{W}{L} (V_{DD} - V_{th})^2 \quad (1.1)$$

μ_{eff} - Effective carrier mobility, C_{ox} - Capacitance (gate oxide) per unit area, W - Width of the channel and L - Length of the channel.

The Figure 1.3a shows the drain current (ID) over gate voltage (VG). It can be evident from the Figure 1.3a, that the transition of the drain current (ID) from off-state to on-state is not an abrupt one. Boltzmann statistics represents the dissemination of energy of charge carriers in source area. So, the subthreshold ($V_G < V_{TH}$) region of operation, diffusion of charge carriers (and hence ID) increases exponentially with increasing VG. The increasing VG reduces the potential barrier.

The off-state leakage current (I_{OFF}) is given by:

$$I_{OFF} \propto 10^{-V_{th}/SS} \quad (1.2)$$

Moreover, the subthreshold swing (SS) is described as the inverse slope of the I_D - V_G curve,

$$SS = \ln(10) \frac{kT}{q} \left(1 + \frac{C_{dep}}{C_{ox}} \right) \quad (1.3)$$

$\frac{kT}{q}$ - thermal voltage ; $1 + \frac{C_{dep}}{C_{ox}}$ - factor from the depletion capacitance. The

oxide capacitance is higher than that of the depletion capacitance of the semiconductor. So the sub threshold slope reduces to, which is 60mV/dec at room temperature. The common MOSFET switching characteristic constrained to be no more acute than the 60mV/dec as because $\frac{kT}{q}$ is the non-scaling physical quantity. In practical MOSFET

switches, the subthreshold swing is typically more than 100mV/dec. The non-scalability of physical quantity sets the fundamental limit on the subthreshold swing. The subthreshold swing tells how suddenly a MOSFET can switch make a transition from the ON state to OFF state. The Figure 1.3a shows the transfer characteristics of the MOSFET. The Figure 1.3b shows the, increase in the leakage current (I_{off}') due to the CMOS scaling [3].

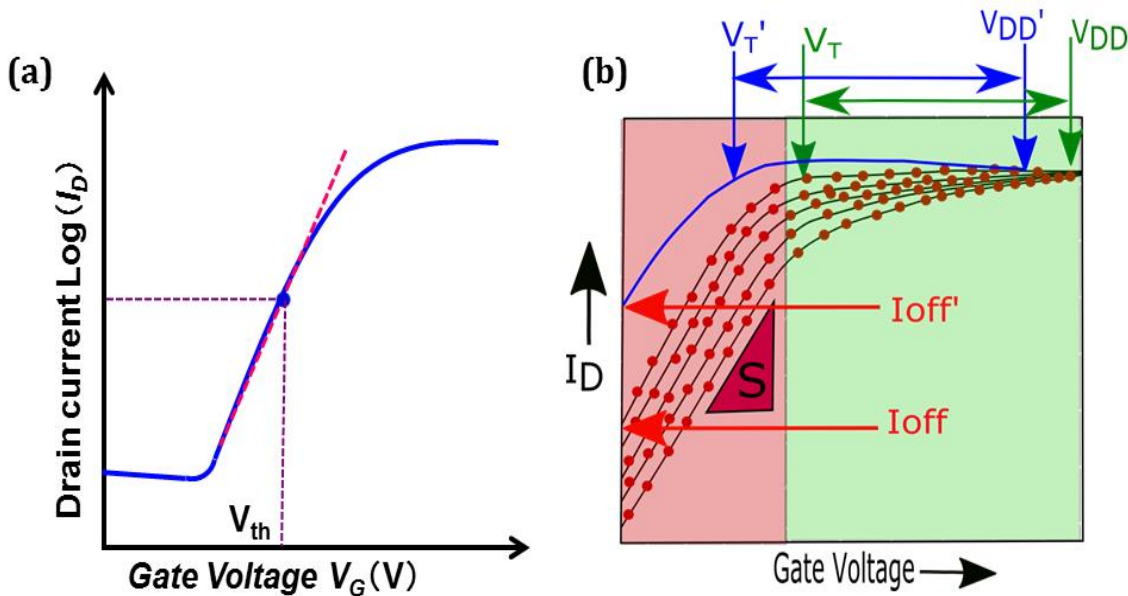


Figure 1.3. (a) Schematic of the subthreshold slope of CMOS device. (b) Effect of scaling in the COMS device. I_{off}' is an increased drain current as a result of the gate scaling.

The total amount of the energy dissipated in the digital CMOS circuits is divided into two main parts. First, the dynamic energy ($E_{DYNAMIC}$), the dynamic energy is comes from either charging or discharging capacitors. Second, leakage energy ($E_{LEAKAGE}$) is generated by off-state leakage current of the MOSFET. The total energy dissipated in the CMOS circuits are given by,

$$E_{TOTAL} = E_{DYNAMIC} + E_{LEAKAGE} \quad (1.4)$$

$$E_{DYNAMIC} = \alpha L_D f C V_{DD}^2 \quad (1.5)$$

$$E_{LEAKAGE} = L_D f I_{OFF} V_{DD} t \quad (1.6)$$

α - the activity factor, L_D - logic depth, f - fan-out and C - capacitance, and t - time delay.

Reducing the V_{DD} can reduce the dynamic energy, which means MOSFET ON current (I_{ON}) is also reduced. The reducing the V_{DD} also increases the time delay (t_{DELAY}). To retain the same ON current, the threshold voltage (V_{TH}) should be minimized. Nonetheless, according to Subthreshold Swing, when the threshold voltage (V_{TH}) is reduced linearly the off-state leakage (I_{OFF}) will increase exponentially.

The panacea to power crisis issue of CMOS devices is a need of new sort of device that has a perfect exchange of conventional CMOS. The new device should possess characteristics of ideal switching. An ideal switch should have abrupt on/off ratio, stable on current, and no leakage current. The Mechanical switching is the proposed solution for the CMOS power crisis. In the mechanical switching, the active element and the fixed electrode are separated by the air gap. This physical separation between suspended beam and the fixed electrode ensures the low off current. And this will lead to the very low leakage. As the leakage is extremely small, the $E_{LEAKAGE}$ becomes negligible. So the total energy only depends on the dynamic energy [7].

1.2 NANO-ELECTRO-MECHANICAL SWITCHING: STATE OF THE ART

1.2.1 OPERATING PRINCIPLE OF MECHANICAL SWITCHING

The device structure of double clamped NEM contact switch is shown in Figure 1.4. Several device structures are available to realize the NEM contact switch. The two primary device type is cantilever type, and double clamped type (resonator). In the

double clamped beam NEM contact switch, there are two elements, one is a fixed element, and the other one is a movable/active element (suspended beam) as shown in Figure 1.4a. The fixed element and suspended element both are separated by an air gap. The voltage is enforced between fixed element suspended beam; the suspended beam begins to deflect towards the fixed element is attributable to the electrostatic force between the fixed electrode and the suspended beam. To understand the pull-in phenomenon consider only the two most important forces in the device; electrostatic force due to the applied voltage and restoring force of the suspended beam. The origin of the restoring force is effective spring constant of the suspended beam. When the given voltage is maximized beyond a certain value, the restoring force no longer can effectively balance the electrostatic force; the suspended beam suddenly deformed to the fixed electrode [8]. This abrupt deflection of the suspended beam gives the sharp rise in the current. The current is referred as the switching current. The switching slope is very steep [9]. The Figure 1.4a shows the OFF state of the NEM contact switch and the ON state of the NEM contact switch is shown Figure 1.4b.

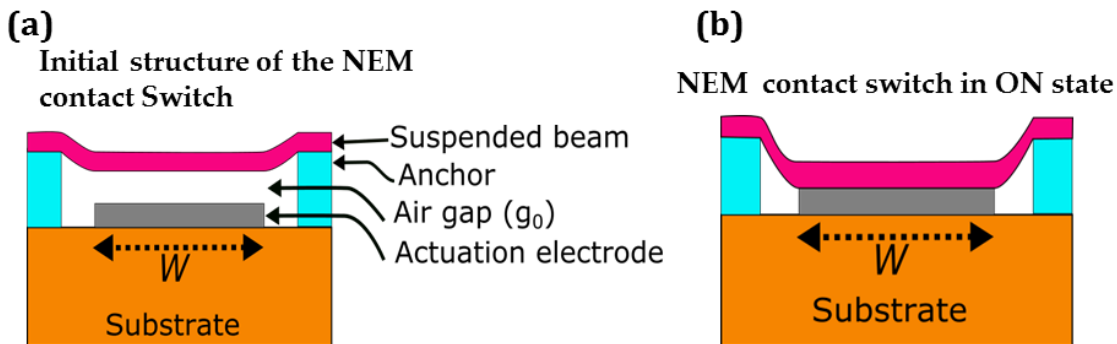


Figure 1.4. (a) The initial structure of the NEM contact switch (double clamped beam structure is shown). (b) NEM contact switch is in ON state.

The switching characteristics of NEM contact switch are shown in Figure 1.5. The switching characteristics regarding the beam displacement are shown in the Figure 1.5a. When the voltage is increased between the fixed electrode and the suspended beam, suspended beam moves towards the fixed electrode gradually up to certain limit, snap-in point. After the snap-in point, the suspended beam abruptly deflects to the fixed electrode. When the voltage is decreased, the restoring force overwhelms the electrostatic force; the pulls the suspended beam to its original position. The immediate collapse of the suspended beam on to the fixed electrode gives the very sharp rise in the current between the fixed electrode and the suspended beam. The switching

characteristics regarding the switching current are shown in the Figure 1.5b. The hysteresis is formed between the switch ON state and the switch OFF state due to the contact force [10].

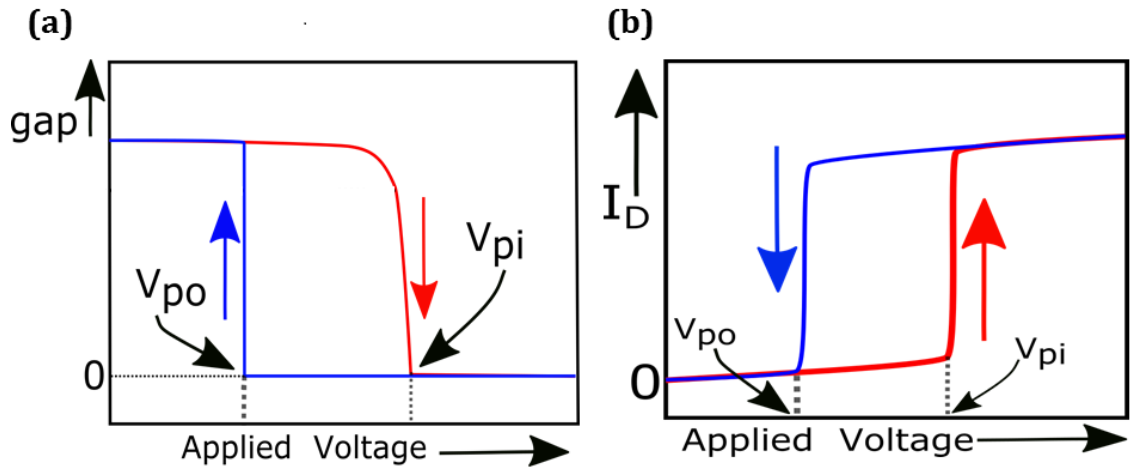


Figure 1.5. An output characteristic of the NEM contact switches (a) Pull-in/Pull-out curves in the regarding displacement. (b) Pull-in/Pull-out curves in the regarding measurement.

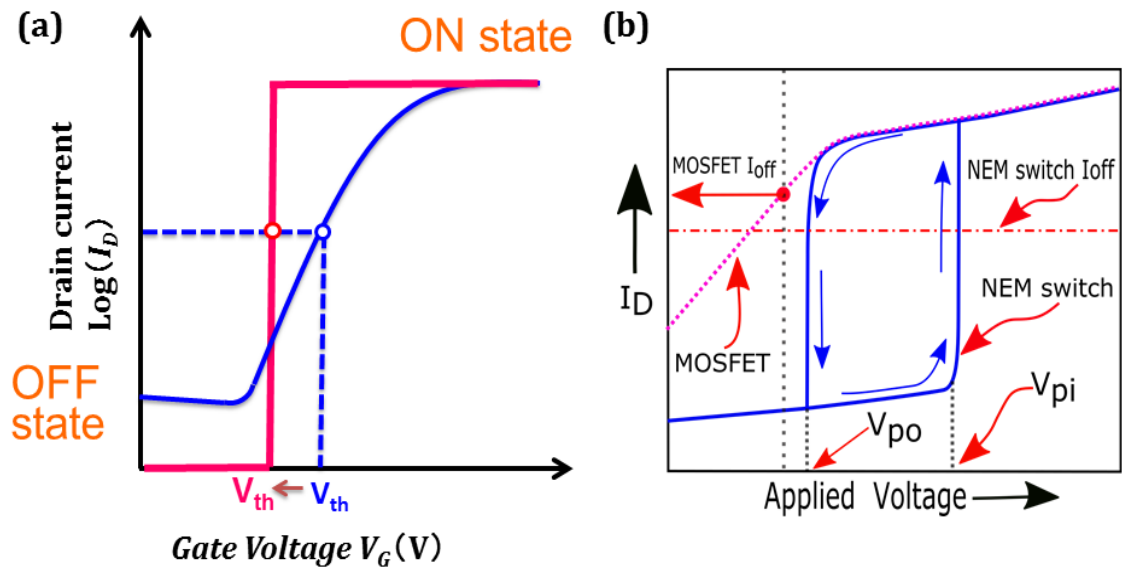


Figure 1.6. Comparison of output characteristics. (a) Switching characteristics of NEM contact switch with CMOS switch (the blue curve is for conventional CMOS, the red curve is for NEM contact switching). (b) Illustrating the both NEM contact switch CMOS switch in the same frame.

The Figure 1.6a illustrates the switching characteristics of the CMOS MOSFET and the mechanical switch. Figure 1.6b shows the combination of the switching characteristics of CMOS and NEM contact switch [10].

1.3 GRAPHENE

Graphene is an atomically-thick two-dimensional (2D) material, which consists of the hexagonal lattice which is made up of carbon atoms [11]. Graphene is a single layer form of the bulk material graphite, which can be easily found from the pencil lead.

Monolayer graphene was exfoliated from the graphite, by using the scotch tape. The first single layer graphene properties are demonstrated by Dr. Andre Geim and Dr. Konstantin Novoselov, for which they were awarded the Nobel Prize in Physics (2010). The different forms for the carbon atoms are shown in Figure 1.7. The graphene additionally can also be grown by the Chemical Vapor Deposition (CVD) technique. The quality of the CVD grown graphene is not similar to that of the exfoliated graphene layer. The single layer graphene is a zero band gap material [12], [13].

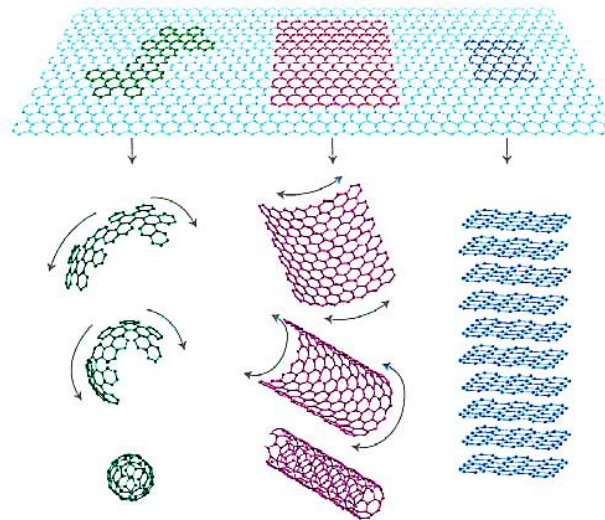


Figure 1.7 Utilizing graphene to build all-dimensional carbon materials.

1.3.1 ELECTRICAL PROPERTIES OF GRAPHENE

Graphene has exclusive band structure. It is a zero band gap material [12]. The conduction band and valence band of graphene are connected at one point, known as the Dirac point, or the charge neutral point. Moreover, the linear dispersion relationships are observed from both the conduction band and valence band when the energy level is not far away from the charge neutral point. The effective electron mass of graphene is zero owing to the linear relationship of momentum k and energy E [11]. Due to this massless behavior, intrinsic suspended graphene possesses extremely high electron mobility, approaching to $200,000 \text{ cm}^2/\text{Vs}$ measured at the low temperature [14]. The electrical property of the graphene is layer dependent. The band gap of the bilayer graphene is tunable by the applying the electric field. Even the electronic properties of

the bilayer graphene are highly rotational dependent. The Bernal stacked bilayers exhibit the metallic behavior where as the twisted bilayer exhibits the semiconducting behavior [13].

1.3.2 MECHANICAL PROPERTIES OF GRAPHENE

Graphene, a single atomic layer of material. The in-plane stiffness of graphene, 340 N/m, was characterized from freely suspended circular shaped membranes by using the nanoindentation method. Graphene possesses an impressively high Young's modulus of 1 TPa [15]. The breaking tenacity was also reported from the same experiment, indicating to a bulk value of 130 GPa. Besides, breaking strain of 25% was investigated, and the graphene membranes were easy to be broken under the nonlinear elastic regime. In the case of NEMS study, the mechanical properties of the movable elements largely determine the performance and reliability of the device. These mechanical properties of graphene mentioned above are better than any of the thin-film materials under the use of NEM technology. Also, graphene has another merit which is resistance to the natural oxidation, revealing that graphene-based NEM device has better reliability compared with the device made from metals.

1.4 REVIEW OF THE RECENT LITERATURE

In this section, some of the important literature are discussed. The NEM contact switches are a primarily a mechanical switch; the electrostatic forces between the fixed electrode and the suspended beam can activate the suspended element. The electrostatic force causes to deflect the suspended element mechanically, further forming a physical contact with the fixed electrode.

As the air gap physically separates the suspended beam and the fixed electrode, NEM contact switch can give low leakage current; NEM contact switch has many enormous advantages such as reduced power consumption and high ON/OFF ratio. Also, the NEM contact switch can operate at high speeds with sub 1-V operation. NEM switches also have potential capability of working in the harsh environment like high radiation, external electric field, and temperature. The NEM switches have been widely explored for the several applications like a relay, a logic device [16], [17], transistor and sensor, which is consistent with these switches based on the conventional

semiconductor technology [18], [19]. Furthermore, the low reliability of the device performance mainly limited by the contact adhesive forces [8].

In this section, different types of NEM contact switches actuated by electrostatic force are reviewed and discussed.

- **Nanowire**-based NEM switches: The nanowires are one of the prime material of choice for the NEM contact switches. The high-performance three-terminal NEM switching FET was successfully demonstrated, using the double clamped Ge/Si core shell nanowire, experimentally by the J.H. Kim *et al.* [20]. Clear pull-in/pull-out operations were observed with a subthreshold slope as low as 6mV/dec. The Ge/Si core shell nano wire NEM FET works in the very high-frequency range. Another important, silicon carbide nanowire based NEM contact switches are demonstrated by X.L. Feng *et al.* [21]. The NEM contact switches are fabricated with a highly small w air gap (~10 nm). Very low activation voltage is demonstrated with on/off ratio $> 10^3$.
- **Carbon Nanotube** based NEM switches: Prof. Iijima discovered a single-wall CNT in 1991. In 2004, a two terminal CNT NEM switch was demonstrated by S. W. Lee *et al.* [22]. Multiwall CNT was used as the suspended material. The device is fabricated as the cantilever type. And the CNT was deflected to contact with drain electrode by applying gate voltage. Switching hysteresis was observed experimentally from this device. No precise switching characteristics were observed as the device shows inferior performance. The pull-in was observed at 5 V.
- **Graphene**-based NEM switches: Graphene is regarded as the material to improve the performance of NEM switches due to its better electrical and mechanical properties. The graphene based NEM contact switch was demonstrated by K.M. Milaninia *et al.* in 2009 [23]. They utilized chemical vapor deposition (CVD) grown graphene. The CVD graphene was used to define both the moveable beam and bottom contact electrode. There is no precise switching was observed. Two years later, a graphene NEM switch with very low pull-in voltage (1.85 V) was demonstrated by S. M. Kim and his colleagues [24]. And their device fabrication showed the compatibility with the conventional CMOS technology. Based on the quantitative study of exfoliated graphene-based NEM switches by Zhang's group, they found that monolayer graphene was not ideal for the NEM application since it was too easy to tear.

Multilayer graphene-based NEM switch worked with a point contact with the probe of Scanning Tunneling Microscope (STM), which reached high reliability among the graphene NEM switching devices (~500 cycles). Instead of double clamped structure, cantilever-type graphene NEM switches were also measured using both two-terminal and three-terminal measurement by P. Li and his colleagues [25]. However, the reliability was still a severe issue of device performance. A bilayer graphene-based NEM switch with local bottom electrode was achieved with very low pull-in voltage, 1.8 V was demonstrated by J.Sun *et al.* [26]. The device works only a very few cycle. And the graphene beam is stick to the fixed electrode. The stiction is attributed to the Au-C chemical bonding. To overcome the stiction issues in the graphene based NEM contact switches, the structurally engineering the contact surface was studied by W.Wang *et al.* [27]. The period trench pattern was introduced in the contact surface to overcome the surface adhesion. The stiction is one of the prominent failure modes in the graphene based NEM contact switches. As the NEM contact switches only work for the very few switching cycles, the failure mode cannot be the ablation. The ablation, in which the suspended beam was damaged by repeated contact cycles [22]–[26].

1.5 THE PURPOSE OF THIS STUDY

As based on the current research, NEM contact switch becomes one of the promising candidates for overcoming the limitations of conventional CMOS technology. The NEM contact switches can offer low leakage current, abrupt switching ($SS < 5\text{mV/dec}$) as well as high ON/OFF ratio. Conventional material (Si) based as well as the graphene based NEM contact switches facing lot problems. One among them is stiction induced failure in the NEM contact switches. Though graphene possesses the excellent electrical and mechanical properties, the conventional contact material (Au, Cr, Cr_2O_3) leads to stiction related failures in the NEM contact switches. The adhesion force between the graphene and the conventional contact material leads to high energy barrier, which causes the irreversible stiction in the graphene based NEM contact switches. To avoid the irreversible stiction in the graphene based NEM contact switches, graphene layer as the contact material is proposed as a solution to prevent the irreversible stiction. It is also essential to understand the interaction between the

graphene layer, a graphene-to-graphene crossbar device is intended as a method to study the interlayer conduction between the graphene layers.

1.6 THESIS STRUCTURE

This dissertation composed into six chapters. The content of these sections is as per the following:

- **Chapter1: Introduction.** This chapter discusses the origin of the crisis and fundamental limit of the CMOS MOSFET switching. The effect of the CMOS scaling. A different switching device with ideal switching characteristics, the NEM contact switches, is suggested as a solution for CMOS power crisis. Further, it also introduces failure issues with the conventional contact NEM switches. The graphene-to-graphene NEM contact switch is proposed as a solution for the NEM contact switches.
- **Chapter2: Essential theory of the NEM contact Switches.** In this chapter, the theory behind the mechanical switching is explained.
- **Chapter3: Theory and Finite Element Method (FEM) simulation of graphene based NEM contact switches.** In this chapter, Finite Element Method (FEM) simulation is introduced. Further, finite element method (FEM) simulation of the graphene based NEM contact Switches is discussed in detail.
- **Chapter4: Fabrication of graphene-to-graphene NEM contact switches.** In this chapter, provides essential detail about the CVD graphene. Then the fabrication process of graphene-to-graphene NEM contact switch is explained in step by step manner. The fabrication techniques such as Graphene transfer (wet chemical based transfer), BHF etching, and super critical point dryer also discussed in detail.
- **Chapter5: Fabrication and characterisation of graphene cross bar device.** In this chapter, the in-situ annealing effect on the interlayer conduction in graphene-to-graphene crossbar device is discussed. Also, the fabrication process of the graphene-to-graphene crossbar device, Raman spectroscopy of the interlayer (twisted bilayer) graphene, incoherent conduction in the misoriented graphene bilayer, in-situ annealing effect on the interlayer conduction, as well as the effect gas ($\text{Ar}+\text{H}_2$) on the interlayer conduction in graphene-to-graphene crossbar device is discussed in detail.

- **Chapter6: Measurements and Characterization of Graphene-to-graphene NEM contact Switches.** In this chapter, we presented the results of the graphene-to-graphene NEM contact devices with different dimensions. Graphene-to-graphene NEM contact switch introduced experimentally for the first time. We extracted the switching slope for several devices which showed very steep switching of <10 mV/sec. Moreover, the graphene-to-graphene NEM contact switches show the stiction free switching characteristics.
- **Chapetr7: Summary and Future work:** This chapter concludes the thesis, and also provide an outlook on future work regarding graphene based NEM contact switches.

2 Essential theory of NEM contact switches.

2.1 INTRODUCTION

In this chapter, the basic physics and related equations behind the switching mechanisms of NEM contact switches are introduced. Pull-in and pull-out conditions of the movable element, as the fundamental operations of NEM contact switches, are explained at first. The equations presented in this chapter are useful for designing NEM contact switches.

2.2 ELECTROMECHANICAL ANALYSIS

2.2.1 PULL-IN ANALYSIS

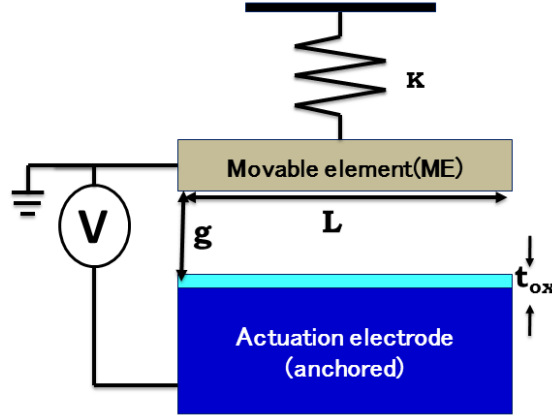


Figure 2.1. 1D parallel plate model of NEM contact Switch.

Figure 2.1 shows a typical one-dimensional (1D) limped model approximation of parallel-plates for the mechanical contact switches. One plate is fixed and controlled by a voltage source, which is normally considered as the fixed actuation electrode. The other plate is a movable element/beam and is connected to a mechanical spring with spring constant K and also connected to ground electrically. The voltage is enforced between fixed actuation electrode and movable beam; electrostatic force is generated by because of the potential difference between the fixed and the movable beam. The electrostatic force causes the movable beam to be attracted to and approach the actuation electrode [32], [33].

The electrostatic force generated between the two plates is expressed as follows:

$$F_{\text{electrostatic}} = \frac{\epsilon_0 W L V^2}{2g_0^2} \quad (2.1)$$

ϵ_0 - Vacuum permittivity

L - Length of beam

W - Width of the beam

V - Applied voltage of the actuation electrode

g_0 - The initial air gap between the movable element and fixed electrode.

The mechanical motion of a movable element is modeled as a linear spring following the Hooke's law, which acts as restoring force. The spring constant is

obtained by the geometry of the movable elements. The equation indicating a linear response of restoring mechanical motion of the movable element is shown below.

$$F_{\text{restoring}} = Kd \quad (2.2)$$

K - spring constant of the movable element;

d - displacement distance moved from anchored electrode from its original position.

For the study of NEM contact switches, double-clamped beam and single-clamped cantilever structure are often investigated. Spring constants of double-clamped beam and cantilever are expressed as [34], [35]:

$$K_{\text{double-clamped beam}} = \frac{32EWt^3}{L^3} \quad (2.3)$$

$$K_{\text{cantilever}} = \frac{EWt^3}{4L^3} \quad (2.4)$$

Where E is Young's modulus of material used for the movable element, L and W are the length and width of its structure, respectively, and t is the thickness of beam or cantilever. The electromechanical system is mainly governed by the mechanical restoring force and electrostatic force. As the voltage is applied between the two electrodes, the movable element initially approaches the fixed electrode, since those two forces mentioned above are under equilibrium state. However, at a certain position (usually two-thirds of the original gap distance), the electrostatic force overwhelms the mechanical restoring force, resulting in a sudden collapse of the movable element on the electrode and a sharp increase of current. The phenomenon mentioned above is called pull-in effect, and we can calculate the pull-in voltage from the estimated electrostatic and restoring force at the position of two-thirds of original gap. The pull-in equation is shown below:

$$V_{\text{pull-in}} = \sqrt{\frac{8Kg_0^3}{27\varepsilon_0WL}} \quad (2.5)$$

If we considered the spring constant of a double-clamped beam and cantilever into the estimation of pull-in voltage, the equations of pull-in voltage could be rewritten as:

$$\text{Double-clamped beam: } V_{\text{pull-in}} = \sqrt{\frac{256Et^3g_0^3}{27\varepsilon_0L^4}} \quad (2.6)$$

$$\text{Cantilever: } V_{\text{pull-in}} = \sqrt{\frac{16Et^3g_0^3}{81\varepsilon_0L^4}} \quad (2.7)$$

2.2.2 THE EQUILIBRIUM POSITION OF THE ELECTROSTATIC ACTUATOR WITH APPLIED BIAS.

As discussed earlier, the electrostatic actuators have one deformable/ movable beam and a fixed electrode. It is essential to understand and determine the amount of static displacement under the applied bias voltage. To analyze the displacement position of the suspended/deformable beam, consider that the equilibrium position can be visualized as shown in Figure 2.2. The X-axis represents the space between the fixed electrode and the movable beam, and the Y-axis represents the force (electrical/mechanical). The movable beam is initially placed at the position X_0 . There are two curves, one represents the mechanical restoring force, and the other one represents the electrostatic force. The mechanical restoring force changes linearly with the position for any applied voltage. (The black line is shown in Figure 2.2) The electrostatic force varies nonlinearly with the position for any applied bias voltage (The red curve showed in Figure 2.2) [36]–[38].

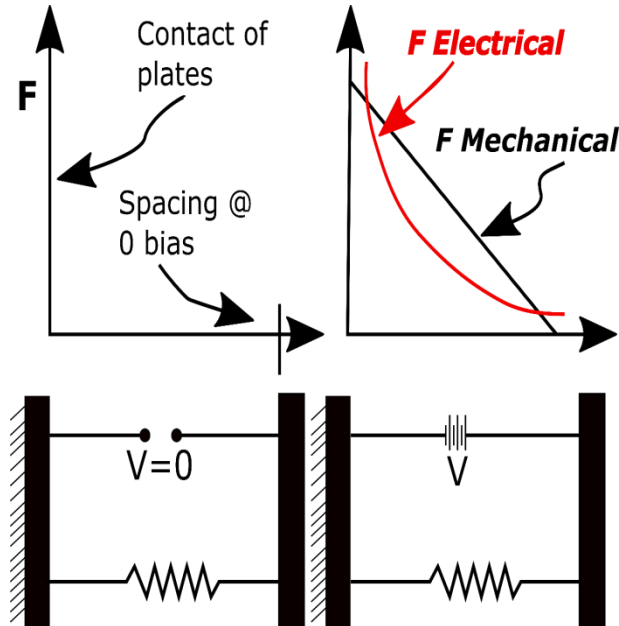


Figure 2.2. Schematic explanation of the equilibrium mechanical and electrostatic force.

There are multiple intersecting points for the two curves, and the intersecting points are identical. The equilibrium position of the movable beam for different applied voltages is demonstrated graphically in Figure 2.3. As the voltage increases, the

corresponding electrostatic curves shift upwards. At a certain bias voltage, the mechanical restoring force and the electrostatic force intersect at one point tangentially. At that point, the mechanical and electrostatic force equal each other. This condition is referred as the snap-in/ pull-in condition. Moreover, the effective force constant of the spring becomes zero. The voltage at this condition is referred as pull-in voltage [39], [40].

After this voltage, any infinitesimal change in the applied voltage leads to a sudden deformation of the movable beam on to the substrate due to the mechanical force being unable to overcome the electrostatic force.

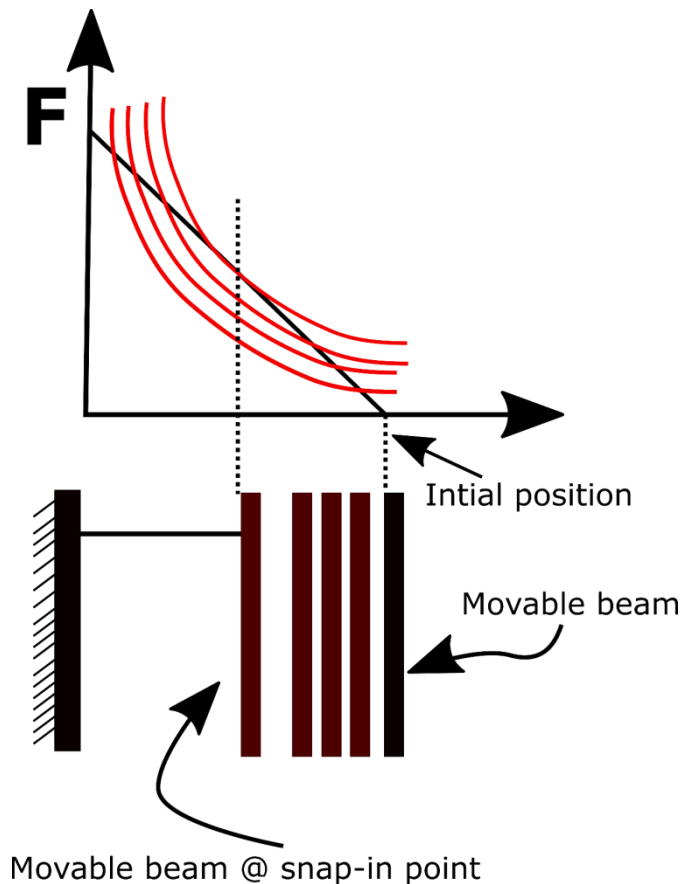


Figure 2.3. Schematic explanation of the equilibrium mechanical and electrostatic force at pull-in condition.

2.2.3 PULL-OUT ANALYSIS

For the pull-out operation, the assumed initial position of both plates is in contact, as shown in Figure 2.3. By applying a voltage, an electrostatic force is generated. The mechanical restoring force at this point obtains the highest value since the movable element is at maximum displacement from its original position. With the decrease of the voltage applied between the movable element and actuation electrode, the

electrostatic force is reduced. Once the mechanical-restoring force overcomes the electrostatic attraction force, the movable element will be detached from the actuation electrode. This process is called pull-out [41], [42].

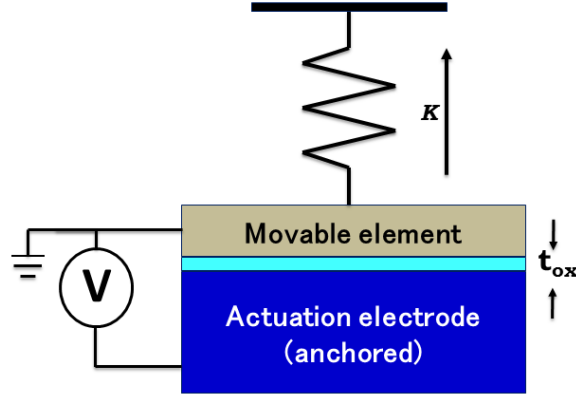


Figure 2.4. 1D parallel plate model to calculate the voltage of pull-out effect.

Owing to the existence of dielectric oxide layer at the contact interface, the polarized dielectric layer governs the electrostatic force. Assuming the dielectric layer having a thickness t_{ox} , the pull-out voltage can be described by the equation below.

$$V_{\text{pull-out}} = \sqrt{\frac{2Kt_{ox}^2}{\epsilon_{ox}\epsilon_0WL}} (g_0 - t_{ox}) \quad (2.8)$$

where ϵ_{ox} is the relative permittivity of the dielectric oxide. This can also be applied with the spring constants of double-clamped beam and cantilever. The modified equations are listed below.

$$\text{Double-clamped beam: } V_{\text{pull-in}} = \sqrt{\frac{256Et^2g_0^3}{27\epsilon_{ox}\epsilon_0L^4}} (g_0 - t_{ox}) \quad (2.9)$$

$$\text{Cantilever: } V_{\text{pull-in}} = \sqrt{\frac{16Et^2g_0^3}{81\epsilon_{ox}\epsilon_0L^4}} (g_0 - t_{ox}) \quad (2.10)$$

The analytical equations describing the pull-in and pull-out voltage rely on ideal conditions such as material properties and precise geometry used. In other words, these analytical models can be used for estimating or examining the proposed structures. There are always some gaps between estimated values and experimental results, since several physical factors, such as short-range forces, dielectric charging effect, are not included in these models.

3 Finite Element Method (FEM) simulation of graphene based Nanoelectromechanical Switches

3.1 INTRODUCTION

There are two main purposes of this chapter; firstly, the chapter is devoted to explaining the essential theory of Finite Element Method (FEM) simulation. It is worth to mention, most of the simulations in this thesis, and especially the Pull-in problem, are carried out by the commercial software IntelliSuite. So, the theory section mainly explains the essential theory behind the operation of the FEM software (IntelliSuite). The second part of the chapter is devoted to the 3D finite element simulation of the graphene based NEM contact switches.

3.2 INTRODUCTION TO FINITE ELEMENT METHOD SIMULATION

To design and predict the behavior of complex systems such as Nano-Electro-Mechanical (NEM) contact switches via the use of appropriate simulation software tools is not a simple task. The design becomes more critical for NEM contact switches, as they require the coupling of different physical domains (e.g., electrical and mechanical). One of the suitable approaches for designing an NEM contact switch is a Finite Element Method (FEM) based software tool. To briefly explain the way these type of simulations work, finite element method divides the 3D geometry of the device into sub-elements (e.g., based on the mesh type), which are connected to each other using nodes. Within each of these small elements, the problem equations are approximated and solved locally. Poisson's equations are solved for the electrostatic problem and elasticity theory relations for the mechanical behavior. Finally, the relations among the set of elements are defined by imposing suitable boundary conditions. FEM tools can simulate and couple the device characteristics belonging to multiple physical domains. For designing NEM contact switches, the coupling of multi-physical domains is highly essential.

To numerically simulate a certain device geometry, the 3D model should be meshed and discretized into a number of finite elements, and the analysis engines can simulate that 3D model. The FEM tool can incorporate mechanical and electrical meshing options. The types of meshing and the refinement criteria may vary depending on whether the electrical or mechanical aspects of the model are being studied. Moreover, the compatibility between these two meshing domains must be considered, as well. To obtain the results with fine accuracy, the FEM model of the device must have a sufficiently refined electrostatic mesh in the areas of high potential gradients and a sufficiently refined mechanical mesh in the areas of high-stress gradients [43], [44].

3.2.1 MESHING

The device geometry is initially created as a solid 3D element, and the geometry is meshed either mechanically or electrostatically depending on the analysis type. If there are more mesh elements, a higher amount of mesh refinement is required in the areas of high mechanical deformation and stress gradients. In NEM contact switches, these areas include spring regions, membranes, and suspended beams. In the analysis modules, mesh refinement can be achieved by using two approaches. First, there is an automatic mesh option which refines the mesh based on a maximum allowable mesh

size; the automatic meshing is a straightforward one. However, by using this option, meshing will govern the geometry globally without discretion. As a result, both areas of mechanical importance, as well as areas of non-mechanical (electrostatic) importance, will be refined. So, the auto-meshing is not the most efficient option for analysis of NEM devices. The second option is refining the mesh locally on the device geometry. This option allows specifying a particular face on the device structure where the refinement will occur, resulting in a more efficient mesh. Locally refining the mesh allows determining whether a mesh is sufficiently dense by running convergence study analysis. For example, one can perform a series of simple voltage sweep analysis with gradually refined mechanical meshes to see what refinement level the mesh provides accurate results of pull-in voltage.

3.2.2 MECHANICAL MESHING

The NEM contact switch has two major parts in the FEM model, the fixed element, and the movable element. The movable element will deform when the voltage applied to the fixed element, and the movable element is increased sufficiently. The accuracy of the FEM simulation, especially for the pull-in voltage, mainly depends on the deformation of the movable element. So is highly essential to get the fine refinement of the movable element. To achieve the high refinement in the areas of the mechanical deformation, the mechanical meshing is used. The mechanical meshing uses the finite element meshing. The movable element is divided into small finite elements and meshed locally. To get the accurate results in the mechanical analysis, the individual element ratio is kept below 20:1 [45].

3.2.3 ELECTROSTATIC MESHING

The electrostatic mesh is based on boundary element, unlike the 3D solid finite element mesh. The boundary element mesh covers only the surface of the device structure. Boundary elements are mainly chosen for electrostatic analysis. The electrostatic mesh is used in FEM based finite element analysis of NEM contact switches because charge density collects on the surfaces and edges of a conductor. In electrostatic meshing, the surface of device geometry is divided into a number of boundary elements. Each boundary element is a triangular panel as it defines a single surface plane. To achieve accurate electrostatic analysis results, there has to be a sufficient mesh in the areas of electrical importance such as for the facing electrodes. Because the FEM tool (IntelliSuite) uses boundary elements, there is no need to mesh

air gaps between conductors(fixed and the movable element). This is an advantage for efficient and accurate simulation of NEM contact devices.

3.2.4 THERMOELECTROMECHANICAL COUPLING.

ThermoElectroMechanical (TEM) analysis is the coupling of the both the electrical and mechanical domains to solve the NEM switches problem. The TEM module incorporates many aspects from both Thermo-Mechanical and Electrostatic analysis. The unique feature is coupled electro-mechanical analysis. For this, the FEM tool (IntelliSuite) uses coupled finite element and boundary element analysis. To solve coupled electromechanical problems, the TEM module uses a relaxation scheme that combines a multi-pole-accelerated BEM based iterative method for electrostatic analysis, along with standard FEM based mechanical analysis to perform self-consistent electromechanical analysis of elastically deformed structures efficiently. During the analysis, iterations are performed by solving the mechanical deformation, using the resultant geometry to resolving the electrostatic solution, and then iterating with the newly updated electrostatic pressures. Equilibrium will be reached when the mechanical and electrostatic forces balance, which can involve nonlinearity in both domains. In the case where the electrical forces dominate the mechanical restoring forces, phenomena such as snap-down can occur. The solution used to efficiently couple the electrostatic and mechanical domains is known as the exposed face mesh method. Equilibrium is judged by a tolerance on the incremental structure deformation. Using boundary element analysis over finite element methods for the electrostatic solution drastically reduces problem size, and avoids complications that arise in such instances as gap closure, where finite elements can reach a zero-volume condition.

3.2.5 THE GOVERNING EQUATIONS FOR FINITE ELEMENT METHOD (FEM) SIMULATION.

As discussed earlier, the in the FEM simulation the two different physical domains are solved. The electrostatic domains and the mechanical domains are solved in the FEM simulation. The NEM contact switches are considered as the capacitive switch. The equations for the electrostatic and the mechanical domains are given as follows;

For the electrostatic force domain, the following equation is solved for the electromechanical problem in TEM module by IntelliSuite software for each discretized element.

$$\varphi(x) = \int_{\text{surface}} G(x, x') \sigma(x') da', \quad (3.1)$$

where ϕ is the surface potential, σ is the surface charge density, $G(x, x')$ is the green function, and da' is incremental in the surface area. The following equations were used by IntelliSuite software to solve the problem for the mechanical domain.

$$\begin{cases} K_{qq} q = F_{ele}(V) \\ K_{uu}(u) = F_{boundary}(V)' \\ K_{vv}(u, V) V = V_{boundary} \end{cases} \quad (3.2)$$

The first equation is the purely mechanical system which considering the electrostatic forces, F_{ele} . Parameter, q , in the first equation is the vector containing the displacements of the mechanical structure. This equation also known as the equilibrium equation of the mesh. While, the vector u in the second and third equations are the displacement of the electrostatic mesh nodes. The third equation is the electrostatic system which depending on the vector, u , displacement. Finally, the electro-mechanical coupling appears through this deformed mesh.

3.3 FINITE ELEMENT METHOD SIMULATION OF GRAPHENE BASED NEM CONTACT SWITCHES

3.3.1 INTRODUCTION

ThermoElectroMechanical (TEM) analysis is the coupling of the both the electrical and mechanical domains to solve the NEM switches problem. The TEM module incorporates many aspects from both Thermo-Mechanical and Electrostatic analysis. The unique feature is coupled electro-mechanical analysis. For this, the FEM tool (IntelliSuite) uses coupled finite element and boundary element analysis. To solve coupled electromechanical problems, the TEM module uses a relaxation scheme that combines a multi-pole-accelerated BEM based iterative method for electrostatic analysis, along with standard FEM based mechanical analysis to perform self-consistent electromechanical analysis of elastically deformed structures efficiently. During the analysis, iterations are performed by solving the mechanical deformation, using the resultant geometry to resolving the electrostatic solution, and then iterating with the

newly updated electrostatic pressures. Equilibrium will be reached when the mechanical and electrostatic forces balance, which can involve nonlinearity in both domains. In the case where the electrical forces dominate the mechanical restoring forces, phenomena such as snap-down can occur. The solution used to efficiently couple the electrostatic and mechanical domains is known as the exposed face mesh method. Equilibrium is judged by a tolerance on the incremental structure deformation. Using boundary element analysis over finite element methods for the electrostatic solution drastically reduces problem size, and avoids complications that arise in such instances as gap closure, where finite elements can reach a zero-volume condition.

Graphene is a two-dimensional material with excellent mechanical stability and electrical conductivity, and a high Young's modulus of ~ 1 TPa [11]. These outstanding properties of graphene make it a very promising material for high-performance NEM contact switches. Using graphene as a material for such devices can address some of the problems of conventional NEM switches by providing high reliability and a low pull-in voltage [26], [46], [47].

In this work, we present a 3D finite element method (FEM) simulation of double-clamped nano crystalline graphene beam NEM switches. We focus on designing the graphene NEM switch in-line with the experimental work [48]. The pull-in and pull-out characteristics from the simulation results are consistent with the experimental results. These models were used to study the double-clamped beam scaling on switching characteristics. After validating the simulation results for the pull-in voltage of the double-clamped graphene beam NEM switch with the experiment results, we studied the von Mises stress to evaluate the reliability of the switch. These results indicated that a longer and thinner graphene beam is more reliable. Also, we also analyzed the effect of the applied electric field on the double-clamped graphene beam NEM switch.

3.3.2 DESCRIPTION OF THE DEVICE GEOMETRY

In this section, we briefly describe the geometry and operation principles of NEM switches. In our earlier work ref.12, we experimentally studied the switching operation of nanocrystalline graphene (NCG) beam NEM switches. The NCG was synthesized by direct deposition of NCG on a Si/SiO₂ substrate using plasma-enhanced chemical vapor deposition (PECVD) [49]. The NCG deposited by PECVD contains both sp² and sp³ hybridized carbon atoms. The deposited NCG film is polycrystalline. The

polycrystalline nano graphene has randomly distributed grain orientation and size [50]. The mechanical behavior of NCG depends on both the grain misorientation and the grain boundary rotation [51]. Moreover, the mechanical strength of NCG depends on the arrangement of the defects in the NCG film. The NCG sheets have almost constant fracture stress and strain, and the fracture strength is independent of the grain size [52], [53]. The polycrystalline NCG sheets have a flaw-insensitive fracture mechanism. Usually, fractures in NCG films originate from the grain boundary and propagate to the rest of the polycrystal. The propagation of the fracture also depends on the grain orientation. Moreover, micro cracks in the surfaces are initiated from topological defects in the NCG polycrystal, which coalesce to form a big crack, eventually leading to the breakdown of the NCG film [54], [55]. As NCG is a polycrystalline material, we considered it as an isotropic material in the FEM simulation of the nanocrystalline NEM switches. The device structure and dimensions are adopted from our previous experimental work. We used Young's modulus of 860 GPa for graphene in all the FEM simulations as reported by this experimental work. This value is comparable to the reported Young's modulus of 500 GPa for layered suspended graphene sheets of between 2 to 8 nm thickness [56]. For the FEM simulations of the experimental device, we considered a graphene beam of length L , width W , and thickness t , and a top metal electrode. The schematic representation of the device is shown in Figure 3.1. The double-clamped graphene beam NEM switch dimensions are detailed in Table 1. For each double-clamped graphene beam NEM switch, the air gap thickness changes owing to the natural buckling of the suspended graphene beam.

Table 3.1. NEM Switch dimensions

NEM switch	Dimension			Air gap thickness (nm)
	Length (μm)	Width (μm)	Thickness (nm)	
A	1.5	0.5	9	75
B	1	0.5	9	50
C	0.8	0.5	9	45

The initial air gap of the device is g_0 . As the voltage applied between the suspended graphene beam and the top electrode is increased, the resulting electrostatic force balances with the elastic restoring force of the deformed graphene. When the applied voltage reaches a critical point, the electrostatic force overwhelms the restoring force, which causes the graphene beam to be pulled towards the top electrode/ fixed element, resulting in closing the switch and thereby leading to a sharp rise in the current flow through the device [57]. When the applied bias voltage is sufficiently reduced, the

elastic restoring forces in the deformed active element pull the switch open, and thus the device operates as a volatile switch. A mechanical hysteresis is formed between the pull-in voltage and the pull-out voltage.

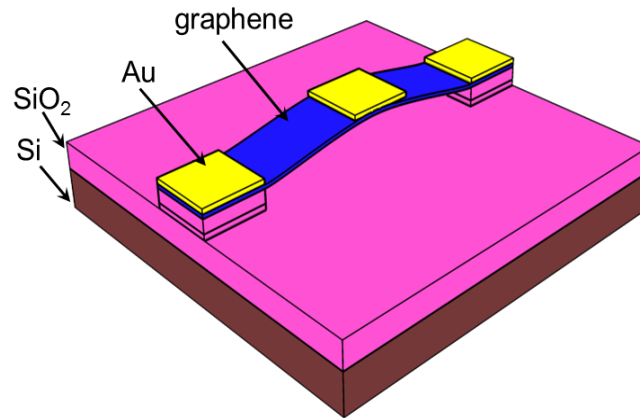


Figure 3.1. Schematic of double-clamped graphene beam NEM switch with top metal actuation electrode.

3.3.3 GRAPHENE NEM SWITCH PULL-IN AND PULL-OUT CHARACTERISTICS

The static electrical and mechanical characteristics of the NEM switch were simulated using the FEM based CAD tool from IntelliSuite. Figure 3.1 shows a schematic of our graphene beam NEM switch with a graphene beam connected to electrodes at each end. This graphene beam NEM switch features a metal top gate (actuation electrode), which enables the graphene beam to be pulled onto the gate when a voltage is applied, and then pulled away, disconnecting from the channel when a voltage is no longer applied. To be consistent with our experimental device structure, we used the device dimensions mentioned in Table 1. Figure 3.2a shows the initial geometry of NEM switch A used in the FEM simulation. To analyze the pull-in and pull-out characteristics of the NEM switch, the voltage applied between the top electrode and the graphene beam was first increased until pull-in was confirmed and then decreased back to 0 V. Figure 3.2b illustrates the geometry of the pulled-in state of the double-clamped graphene beam NEM switch. The color bar shows the displacement of the graphene beam concerning the initial position.

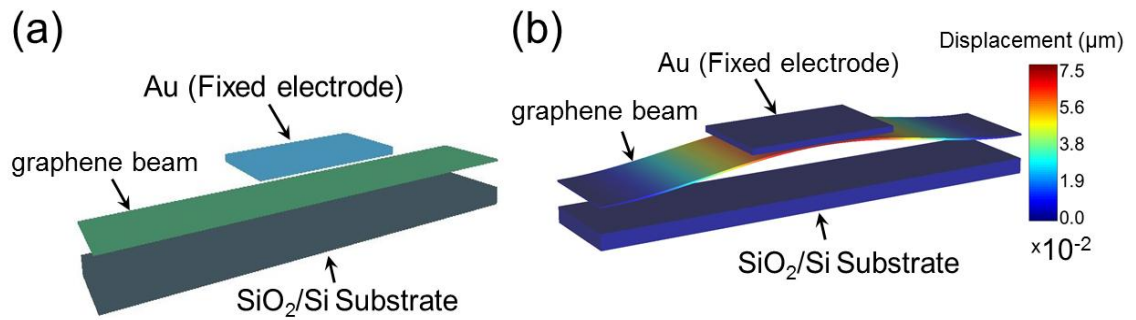


Figure 3.2. The geometry of NEM switch A. (a) Initial structure of double-clamped graphene beam NEM switch with a top metal electrode. (b) Pulled-in state of the graphene beam; color bar indicates the relative displacement with respect to the initial condition.

Figure 3.3a shows the pull-in/pull-out characteristics obtained for the different graphene beam NEM switches mentioned in Table 1. The pull-in voltages for the graphene beam NEM switches A, B, and C are approximately 8.6 V, 13.2 V, and 20.8 V, respectively. The obtained pull-in voltage shown in Figure 3.3a is in good agreement with the experimentally reported pull-in voltages. In order to clarify the impact of the thickness of the graphene beam, we conducted the FEM simulation for one of our experimental device structures (NEM switch A) with different graphene thicknesses of $t = 3$ nm, 5 nm, and 9 nm. Figure 3.3b shows the pull-in, and pull-out characteristics for the graphene beam with different thicknesses for the voltage applied between the top gate and the graphene beam. When the thickness is reduced, the pull-in voltages are evaluated to be 8.6 V, 4.3 V, and 2.1 V for $t = 9$ nm, 5 nm, and 3 nm, respectively. This result shows the clear dependence of pull-in voltage on the scaling of the thickness of the suspended graphene beam. Thus, we confirm that the introduction of thickness scaling leads to a reduction of the pull-in voltage.

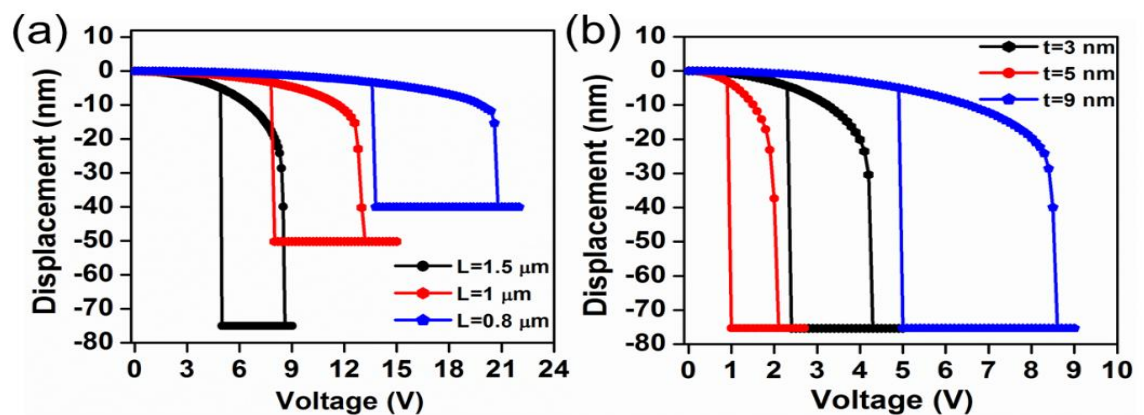


Figure 3.3. Pull-in/Pull-out switching characteristics of the double-clamped graphene beam NEM switches. (a) Switching characteristics of graphene beam NEM switches A, B, and C. (b) Switching characteristics of graphene beam NEM switch A, with different graphene thickness of $t = 3$ nm, 5 nm, and 9 nm.

3.3.4 VON MISES STRESS ANALYSIS

Von Mises yield criterion is a general way to estimate the yield of any ductile material, such as metals [58]. The mechanical reliability of the graphene beam NEM switch can potentially be improved by properly choosing the switch dimensions [59]. To quantitatively demonstrate the mechanical reliability of the double-clamped graphene beam NEM switch, we compared the maximum von Mises stress exerted along the length of the graphene beam. von Mises stress profile analysis is essential to comprehend the spatial variation of the stress generated on the suspended graphene owing to the applied voltage. A Cartesian coordinate system is used to represent the numerical coordinates on the suspended graphene beam. The stress profile is obtained after the pull-in state was achieved, giving the three-dimensional stress profile for the deformed graphene beam. However, the stress variation along the thickness is constant.

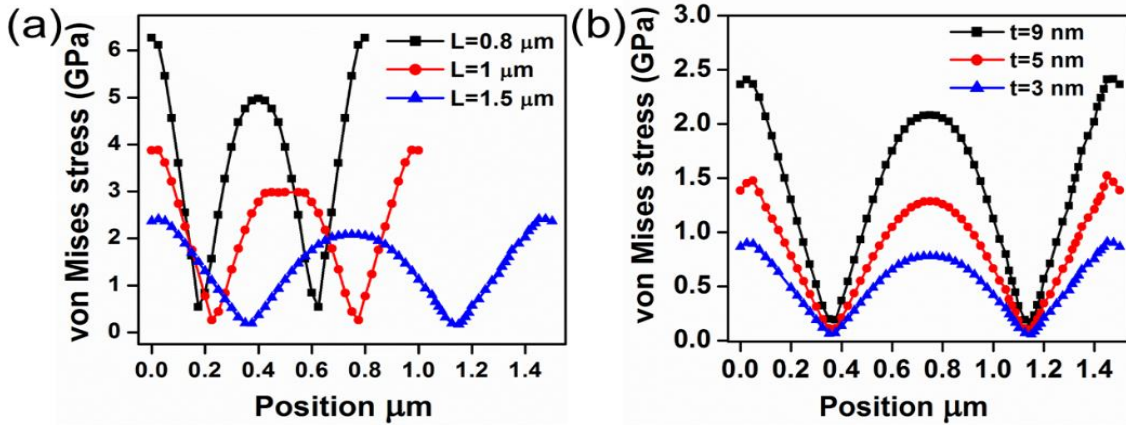


Figure 3.4. von Mises stress of double-clamped graphene beam NEM switches. (a) von Mises stress of graphene NEM switches A, B, and C. (b) von Mises stress of graphene beam NEM switch A, with different graphene thicknesses of $t = 3$ nm, 5 nm, and 9 nm.

Figure 3.4 shows the von Mises stress for the different graphene beam NEM switches. The von Mises stress reaches the maximum value towards the ends of the graphene beam. When the length of the graphene beam is reduced, the von Mises stress is increased to the maximum value. As evident from Figure 4.4a, the device with the shortest graphene beam length has the maximum probability of failure. When the thickness of the graphene beam is scaled for the fixed length of the beam, the von Mises stress is reduced as the thickness is reduced. The results suggest that NEM switch A is at least as reliable as NEM switches B and C.

NEM switch C has a maximum von Mises stress of 6.2 GPa. When the length of the graphene beam is increased to 1 μm and 1.5 μm, then it leads to a decrease in the

von Mises stress of 3.8 GPa and 2.3 GPa, respectively. Furthermore, the maximum stress for NEM switch A is 2.4 GPa; when the thickness of the graphene is reduced to 5 nm and 3 nm then the stress is decreased to 1.4 GPa, and 0.9 GPa, respectively. Figure 3.5 illustrates the top view of the von Mises stress counter plot of the graphene beam. It is evident from the contour plot that the von Mises stress is highest nearer to the both fixed ends of the beam. The von Mises stress reaches the minimum value between the fixed end of the beam and the center of the beam in the pull-in state. If we examine the von Mises stress across the beam carefully, then we can observe higher stresses at the edges of the graphene beam compared to those at the center of the beam. To clarify this point, 3D electric field distributions in the NEM switch are carried out in the pulled-in state.

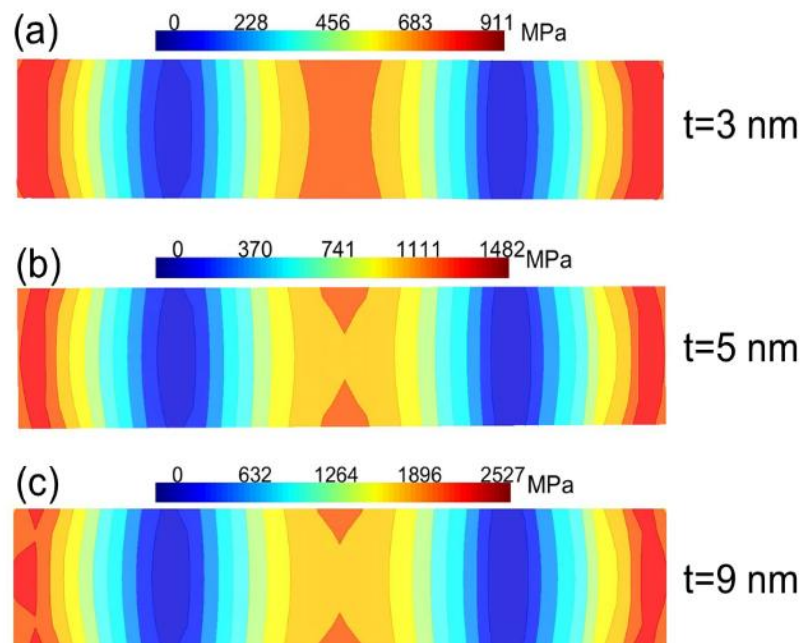


Figure 3.5. Contour plot (top view of graphene beam) of von Mises stress for the NEM switch A, with different graphene beam thicknesses of $t = 3$ nm, 5 nm, and 9 nm.

3.3.5 3D ELECTRIC FIELD DISTRIBUTIONS AND ITS ROLE IN GRAPHENE BEAM NEM SWITCH OPERATION

To analyze the impact of applied electric field on the double-clamped graphene beam NEM switch, we made the same model in COMSOL Multiphysics. The NEM switch was built inside a vacuum environment. The model was meshed with triangular mesh elements to reduce the computational complexity. The density of the mesh was varied adaptively to study the structural displacement of the graphene beam. In this simulation, the actuation electrode was kept at the bottom, and the graphene beam was placed at the top. For the electric field analysis at different voltages, a constant bias of 0

volts was applied to the bottom electrode (Au), and the voltage applied to the top electrode (graphene beam) was swept. The potential, V , and the electric field, E , in the free space can be obtained by solving Poisson's equation [31]. Figure 3.6a shows the cross sectional view of the electric field distribution across the center of the NEM switch for the applied voltage of 1 V to the bottom electrode. The dimensions of the graphene beam are equivalent to those of the NEM switch A. Arrows in this plot show the electric field lines directions. At the center of the beam, the electric field lines are distributed vertically. The orientation of the electric field distribution is gradually changed to the horizontal direction towards the edges of the beam. At both edges of the beam, the electric field is distributed more horizontally in the outward direction to the center of the beam.

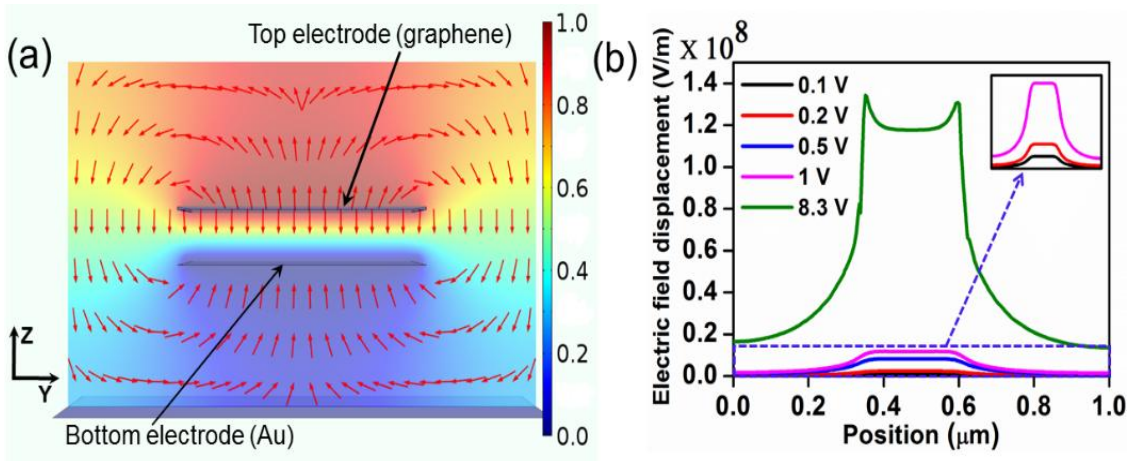


Figure 3.6. 2D Electric field distribution across the center of the NEM switch. Dimensions of the graphene beam (top electrode) are equivalent to those of the NEM switch A. (a) The electric field distribution across the switch at the center of the beam. Arrows indicate the electric field direction. (b) The electric field strength in the Z direction at 5 nm above the bottom electrode at different voltages applied between the bottom and top electrodes. The inset shows zoomed-in version of electric field distribution for lower actuation voltages as indicated by the dashed box; the scale is same as (b).

Figure 3.6b illustrates the 1D electric field strength in the Z direction at 5 nm above the bottom electrode for the different applied voltages. Consistent with Figure 3.6a, the electric field strength is highly concentrated at the edges of the graphene beam. These results demonstrate that the downward component of the electrostatic force acting on the edges of the graphene beam is higher than that at the center of the beam. In order to analyze this edge field termination effect, mechanical deflection analysis of NEM switch A with 3-nm graphene thickness was done. Figure 3.7 shows the displacement of the graphene beam nearer to the pull-in state. If we consider the edge of the graphene

beam, then the downward bend of the beam edges is apparent. This is also consistent with the higher von Mises stress at the beam edges.

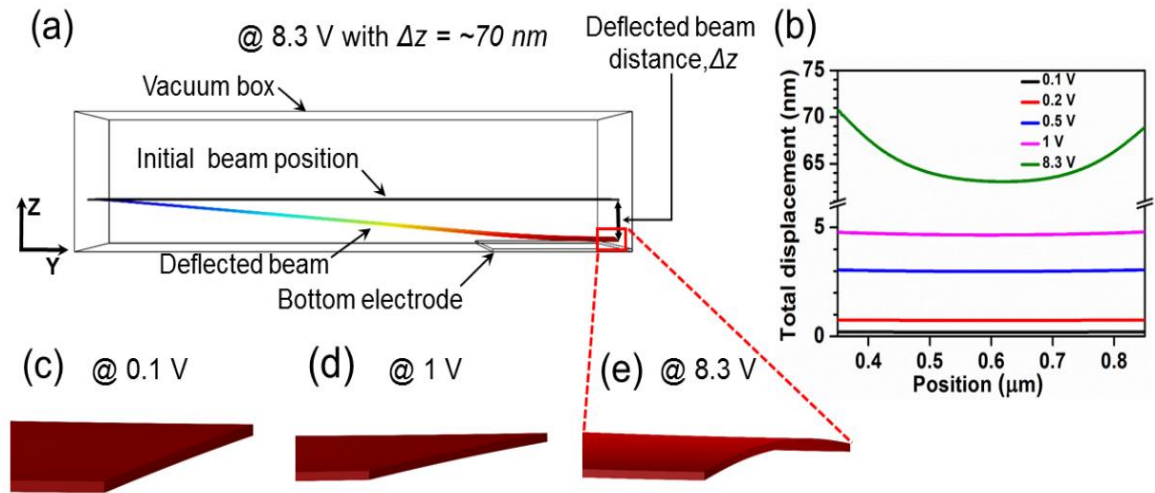


Figure 3.7. Effect of the beam edge electric field termination at 8.3 V. (a) The displacement of the beam at 8.3 V shown as a side view. (b) The displacement of the beam from an initial position at different applied voltages. Birds-eye cross sectional view of the graphene beam at (c) 0.1 V, (d) 1 V, and (e) 8.3 V.

3.4 CHAPTER SUMMARY

In summary, in this chapter the Finite Element Method (FEM) based simulation is discussed. Especially, all the essential theory needed for the simulating the NEM contact switches are discussed in detail. In FEM simulation the NEM contact switch is separated into two domains, one is mechanical domain and the electrical domain. And the result is obtained for the coupling of the two domains. The detailed information of meshing is explained, and its importance in result convergence is also discussed.

In addition, in this chapter, we have studied the electro-mechanical switching and mechanical reliability of graphene beam NEM switches by 3D FEM simulations. The structural dimensions for the device are obtained our experimental results. We have analysed the pull-in/pull-out results of the graphene based NEM contact switch. To evaluate the mechanical reliability of a graphene beam NEM switch, we scaled the length and thickness of the graphene beam and studied the von Mises stress for each structure. This analysis showed that the graphene beam NEM switch with a longer length of 1.5 μm and a thickness of 3 nm has a pull-in voltage of 2 V. The electrostatic force concentration at the edges of the graphene beam leads to more mechanical deflection at the edges than at the center of the beam.

4 Fabrication of graphene-to-graphene Nanoelectromechanical switching devices

4.1 INTRODUCTION

The principle reason of this chapter is to explain the fabrication process of graphene-to-graphene NEM contact switches. Also, the cleaning process of the CVD graphene, wet transferring of the CVD grown graphene layer, and the Supercritical point drying method is also discussed.

4.2 SAMPLE PREPARATION

The Chemical Vapor Deposition (CVD) - grown graphene was used for all the fabrication process. We received the samples from Graphene Platform Co., Ltd. Single layer of CVD graphene transferred on SiO₂/Si substrate where the SiO₂ is thermally grown with thickness 100 nm on top of highly N- doped silicon with resistivity < 50 Ω.cm.

4.2.1 CLEANING THE CVD GRAPHENE

Graphene is very sensitive to impurities and contaminants; therefore, the cleanliness of graphene is vital when studying its intrinsic properties. Due to the polymer residue after the transfer process, cleaning the sample is necessary and critical. Therefore, we put the sample in hot Acetone (60°C) for 30 min before rinsing in IPA for additional 2 min. Then we put the sample in the infrared furnace (ULVAC VHC-P610CP) for 3 hrs at 250°C in (Ar+H₂) atmosphere. Figure 4.1c shows Raman spectrum of one of the received samples (before cleaning).

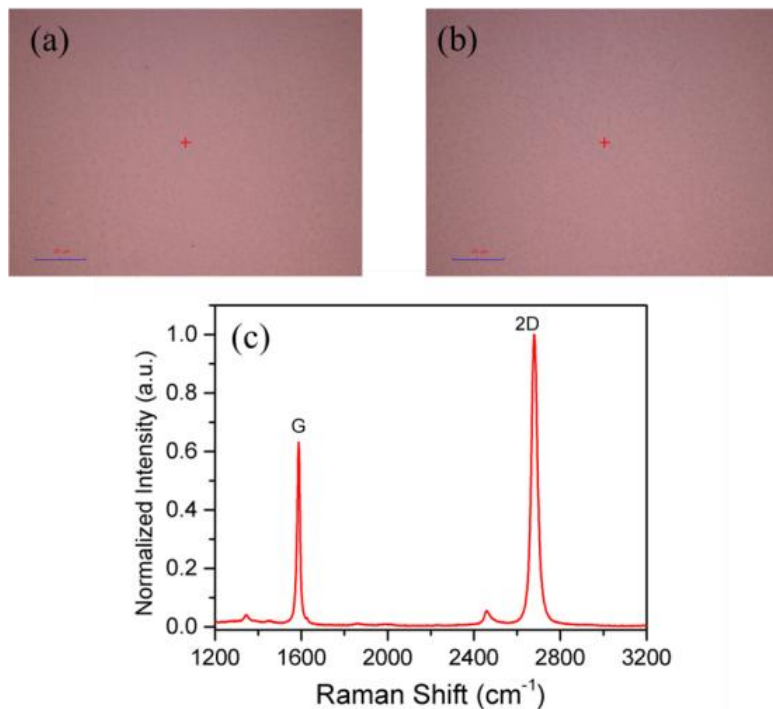


Figure 4.1 (a) and (b) optical microscopy images of CVD graphene sample from Graphene Platform. (c) A Raman spectrum collected from one of our CVD samples.

4.3 FABRICATION OF GRAPHENE-TO-GRAPHENE NEM CONTACT SWITCH

In this section, the fabrication flow of the graphene-to-graphene NEM contact switch is explained in detail. The fabrication steps are divided into sub sections to allow explaining the fabrication flow more quickly. Figure 4.2 illustrates a schematic diagram of CVD grown graphene on the Si/SiO₂ substrate.

4.3.1 FABRICATION OF ADDRESS PATTERN

Address pattern fabrication is the first step in the fabrication process. The following steps are carried out for the address pattern fabrication.

Standard cleaning and Annealing

The CVD grown graphene was used for the device fabrication. The sample was cleaned by the standard cleaning process. The standard cleaning process involves, first the sample was cleaned using the Acetone for 30 minutes at 60°C, and then the sample was cleaned in IPA for 5 minutes. The sample was dried naturally. After the cleaning process, the sample was annealed in the hydrogen (Ar+H₂ (10%)) environment for 180 minutes at 300°C.

Spin coating

This section explains the general procedures for spin resist onto a sample with the spin coater. Before the spin coating, confirm the cleanness of the sample. Any dirt can result in lithography defects and broken devices. For Address pattern fabrication the bilayer resist was used. There are two main reasons, the bilayer resist offers high thickness and it can also offer undercut which is useful for lift-off process.

- Dehydration baking: the sample was kept on the hot plate at 180°C for 5 min. And then the sample was cooled in air for 1 min.
- For Address pattern fabrication two different resists are used. The MMA and PMMA have used the resist. The both MMA (Methyl Methacrylate) and the PMMA (Poly Methyl Methacrylate) are generally referred as the bilayer resist.
- The MMA was coated on the clean sample. The spin speed was set to 2000 rpm.
- The MMA coated sample was soft baked for 5 mins at 180°C.
- The PMMA was coated on the MMA coated sample. The spin speed was set to 4000 rpm.
- The PMMA coated sample was soft baked for 5 mins at 180°C.

Electron Beam Lithography process

The lithography was performed using Elionix ELS-7500 electron beam lithography system. The electron beam dose for the address pattern fabrication was set to $210 \mu\text{C}/\text{cm}^2$. The acceleration voltage of 50 keV was used for the address pattern fabrication.

Developing

The electron beam exposed samples developed using the proper developer. The MIBK: IPA solution is used as the developer. The MIBK (Methyl isobutyl ketone) and the Isopropyl alcohol (IPA) are mixed in the 1:1 ratio. The sample was developed for 51 secs in MIBK: IPA, after that the sample was rinsed in pure IPA solution for 30 mins.

Reactive ion etching (RIE)

For the address pattern fabrication, the RIE etching was used to remove the graphene in the developed area. It is essential to avoid the failure during the lift-off process. Because the metal deposited on the graphene layer was not sticking on the substrate. By removing the graphene using the RIE then the metal can be directly deposited on the SiO_2 surface. The process information for the RIE was given below:

- RF Power: 30 W
- Gas: O_2
- Etching Time: 10 sec
- Pressure: 4 Pa

Metal Deposition.

The Electron beam Evaporation was used for the metal deposition. The metal deposition was carried out in the very low pressure ($<1 \times 10^{-3}$ Pa). First, 5 nm chromium (Cr) was deposited. And then, 85 nm gold (Au) was deposited. Acetone was used for lift-off of the metal.

In this fabrication of the address pattern is an important step, in this step mainly the chip marks are fabricated. These marks are used as the location identifiers, for any further EBL exposure. And the chip marks ensure the accurate EBL writing in the next e-beam lithography steps. Alignment marks without any rough surfaces and well-defined edges are good for the easy detection, which will reduce the process failures in the fabrication flow.

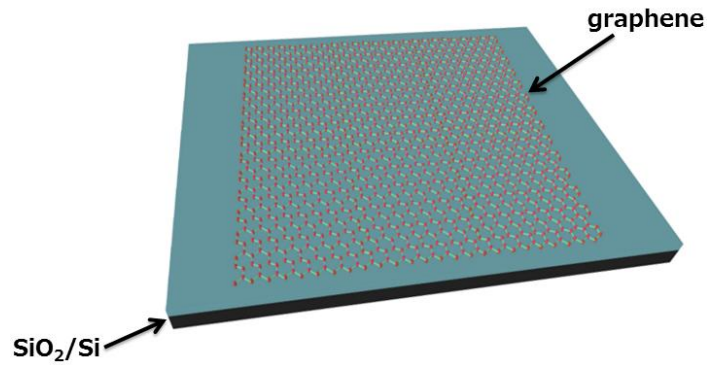


Figure 4.2. CVD graphene on Si/SiO₂ substrate.

4.3.2 PATTERNING OF THE GRAPHENE RIBBON

To pattern the graphene ribbon, a single layer of positive resist was used. Only PMMA was used. PMMA is coated at 4000 rpm, and the sample was baked for 5 minutes at 180 °C directly after spin coating. The advantage of using a single layer resist with high is to get the high resolution of the structure. The E-beam exposure was performed using Elionix ELS-7500. Electron beam dose of 210 $\mu\text{C}/\text{cm}^2$ was used for patterning the graphene ribbon with 1nA as the beam current, and with 50 keV as acceleration voltage. The same development process was used as mentioned in the previous section.

In this step, we have used the mask in such way that the unexposed area forms the graphene ribbon by removing the graphene in the exposed area. The exposed Graphene layer was etched using the RIE etching. The process information for the RIE was same as the previous section. Figure 4.3 shows the schematic of the fabricated graphene ribbon.

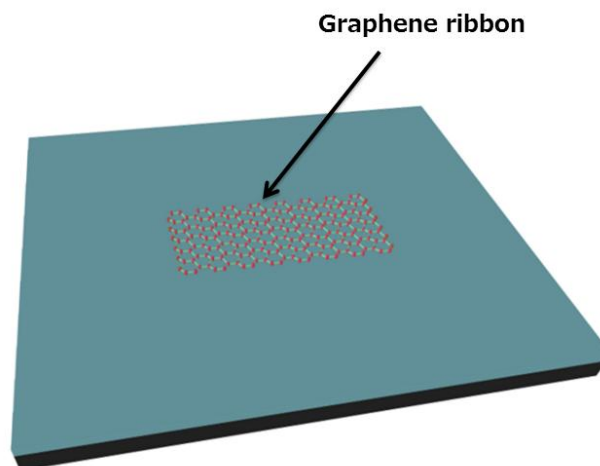


Figure 4.3. Patterned graphene ribbon.

4.3.3 FABRICATION OF CONTACT ELECTRODES

For fabricating the gold contact electrodes, we have used bilayer resist. Methyl Methacrylate (MMA) and Poly Methyl Methacrylate (PMMA), both of the resist are positive tone resist. Usually, these two resist are referred as the bilayer resist. The spin coating method was used to cover the sample with resist. First, the MMA was spin-coated on to sample. The spin speed was set to 2000 rpm; then the resist coated sample was baked for 5 mins at 180°C. After that, The PMMA was spin-coated on the sample which already coated with MMA. The spin speed was set 4000 rpm; the sample was baked for 5 mins at 180°C after the spin coating. The main advantage of using a bi-layer resist for the fabrication of the address pattern is, after the EBL exposure and development, the formation of an undercut in the MMA resist layer. Due to the high resolution of MMA resist, the undercut is formed. The formation of the undercut significantly helps the lift-off process. The e-beam exposure was performed using Elionix ELS-7500 system. The same EBL process information was used, as mentioned in the previous section. Then, the Electron beam Evaporation was used for the metal deposition. The metal deposition was carried out in the very low pressure ($<1 \times 10^{-3}$ Pa). First, 5 nm chromium (Cr) was deposited. And then, 85 nm gold (Au) was deposited. Acetone (sample kept in hot Acetone for at least 40 min) was used for liftoff the metal. Figure 4.4 illustrates the schematic representation of the device after the electrode fabrication. Optical microscope of the device structure after the contact electrode fabrication is shown in Figure 4.4b.

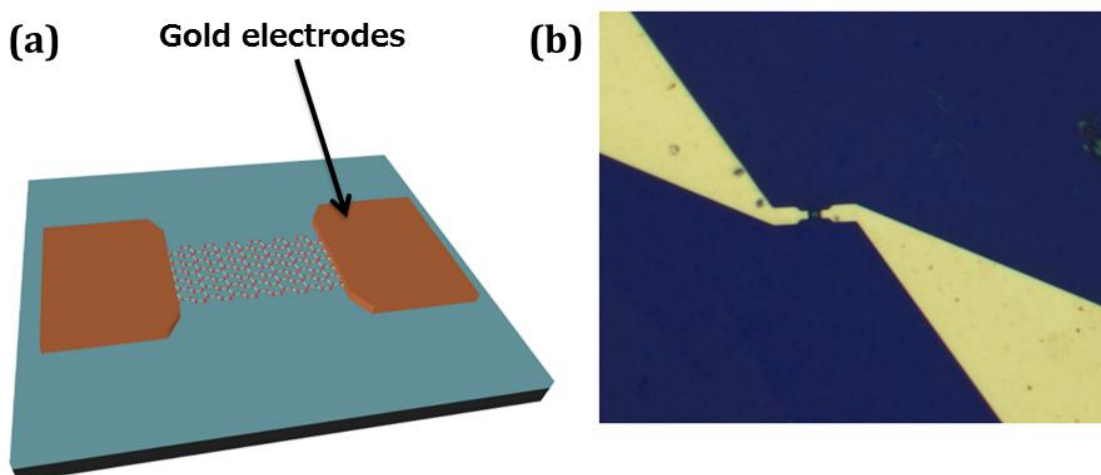


Figure 4.4. Fabrication of gold electrodes. (a) Schematic illustration of the gold electrode Fabrication. (b) Optical microscope of the device after the gold electrode fabrication.

4.3.4 DEPOSITION OF SiO₂ AS A SACRIFICIAL LAYER

For deposition of the SiO₂, we have used the same e-beam recipe which is mentioned in the section 4.3.2 (Electrodes fabrication).

The SiO₂ deposition was carried out using electron beam evaporation method. Then, electron beam evaporation system (ULVAC MUE-ECO-EB) was used to deposit SiO₂. The deposition was carried out in the very low pressure ($<1 \times 10^{-3}$ Pa), 85 nm of the SiO₂ was deposited. Acetone (sample was kept in hot Acetone for at least 30 min) was used to lift off the SiO₂. Figure 4.5 illustrates the schematic representation of the device after the SiO₂ deposition.

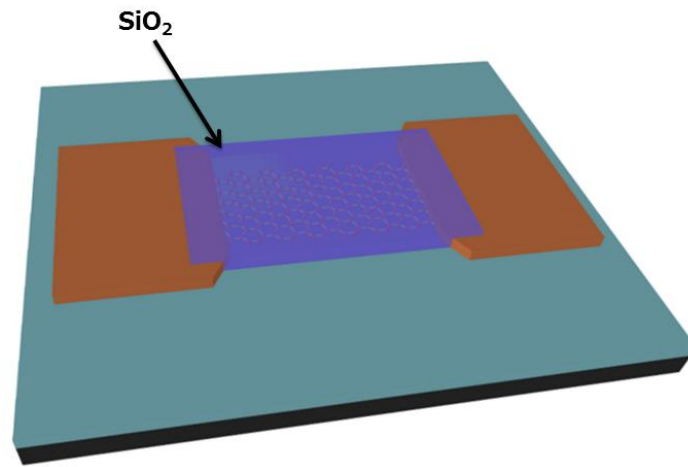


Figure 4.5. Deposition of SiO₂ Layer.

4.3.5 TRANSFERRING TOP GRAPHENE LAYER

After the SiO₂ deposition is finished. Another layer of CVD grown graphene is transferred on top of the sample. The sample already has fabricated device structures. We have employed the wet transferring method to transfer the CVD graphene layer. The wet transferring method is explained in detail as follows. The CVD grown graphene is separated from the copper foil using a Ferric chloride (FeCl₃) solution. FeCl₃ is used as the copper etchant. A 0.1M concentration FeCl₃ solution was used. The CVD graphene in copper foil is cut with a specific dimension, and it is spin coated with PMMA resist. The PMMA resist provides the mechanical support to the graphene layer. After spin coating, the graphene layer was kept in FeCl₃ solution for about ~10 hrs to remove the copper. Then, the graphene/ PMMA bi-layer was rinsed with diluted HCl (10%) to remove remaining metal particles and rinsed in DI water for several times. After that, the graphene layer was transferred to the main sample which already has the fabricated

device structure. The sample was dried naturally for one hr. After that, the PMMA layer was removed by acetone. The schematic diagram of the device with the top graphene layer transfer is shown in Figure 4.6.

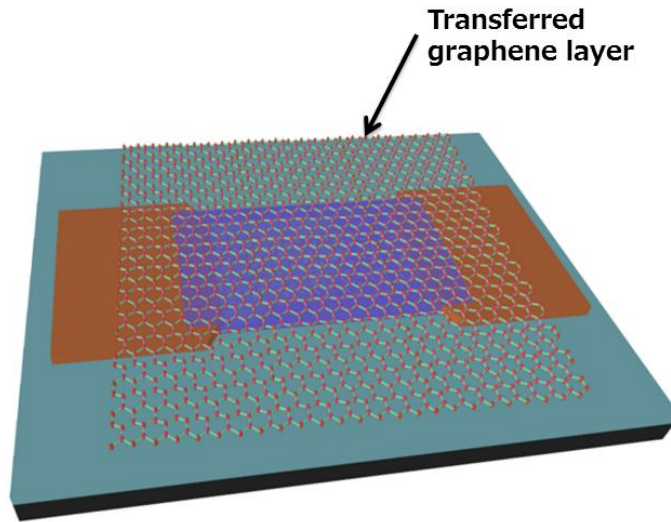


Figure 4.6. Transferred the top graphene layer.

4.3.6 PATTERNING THE TOP GRAPHENE LAYER

To pattern the top graphene layer, We have used the same E-beam recipe and development process as in section 4.3.2. Figure 4.7 shows the schematic diagram of the fabricated device after patterning the top graphene layer.

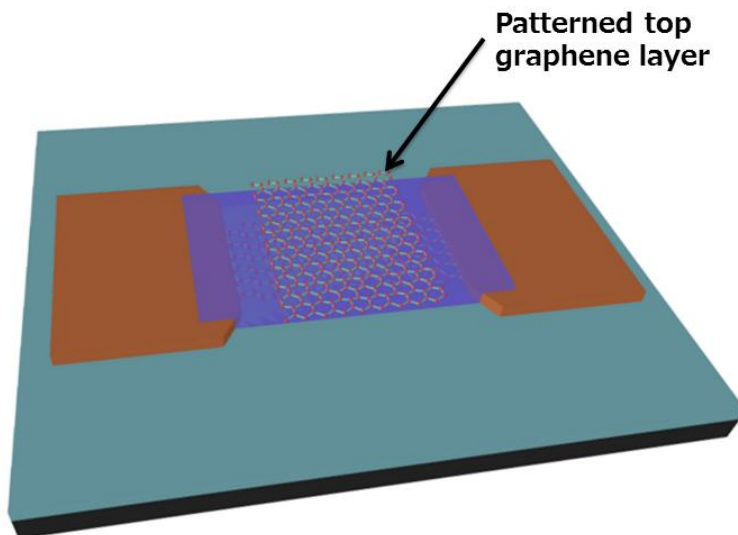


Figure 4.7. Pattern the top graphene layer.

4.3.7 FABRICATION OF THE TOP CONTACT ELECTRODES

To fabricate the top contact electrodes, We have used the same E-beam recipe and development process as in section 4.3.3. Figure 4.8a shows the schematic diagram of the fabricated device after the top electrode fabrication graphene layer. Optical microscope of the device structure after the top electrode fabrication is shown in Figure 4.8b.

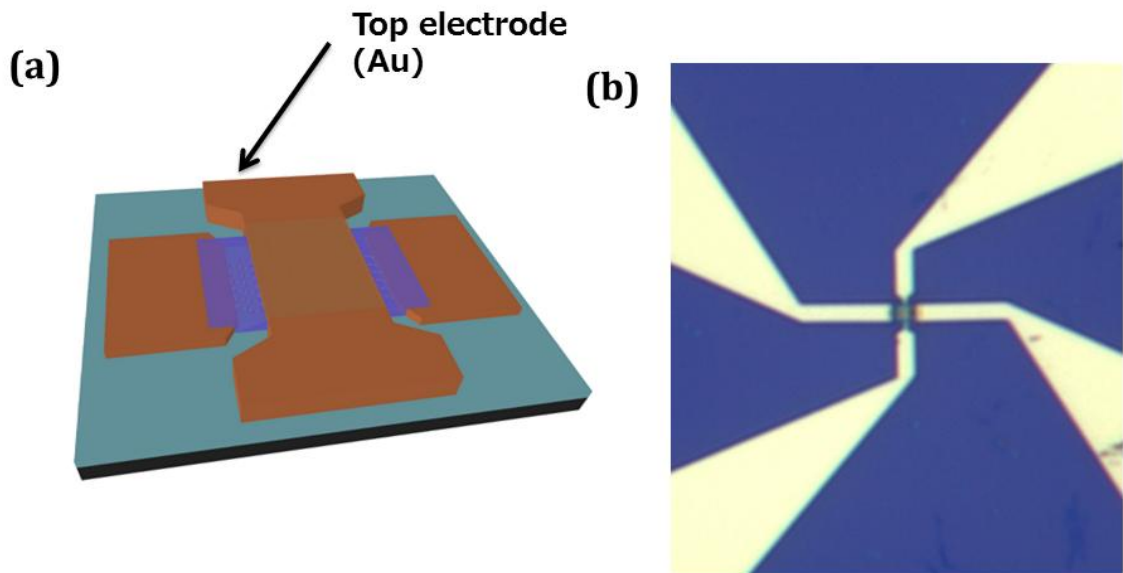


Figure 4.8. Fabrication of top electrodes. (a) Schematic of the device structure after the top electrode fabrication. (b) Optical microscope image of the device.

4.3.8 RELEASING THE SACRIFICIAL LAYER (SiO_2) USING THE BHF

The sacrificial layer (SiO_2) removal is often accomplished using the wet chemical solution method. The wet chemical method has several advantages such as

- high-speed etching
- Simple experimental procedure
- Good selectivity.

It is essential to dry the after the wet chemical etching. However, the drying process is not always the straightforward method. The natural drying process gradually removes the liquid. The liquid encapsulates the both top and the bottom surface of the graphene beam. Moreover, it takes much longer time to remove the liquid by the natural drying process. Surface tension has developed at the interface of the trapped liquid and this acting in the direction tangential to the liquid-air interface. The surface tension usually causes the graphene beam to deform to the substrate. As the dimension of the graphene-to-graphene NEM contact switch is the range of few micrometers, the surface

tension force has a very significant impact. To avoid stiction, usually, we employed super critical point dryer to release the graphene beam.

The detailed BHF etching process is furnished as follows, to achieve suspension of double clamped graphene beam, buffered etch solution of HF was used. The solution is a mixture of NH_4F and HF with a ratio of 6:1. BHF efficiently etches the sacrificial layer which is a evaporated SiO_2 and the substrate SiO_2 . The sample was etched for 60 seconds. To avoid the collapse of graphene beam owing to surface tension, critical point dryer was performed to dry the etched samples. It is worth to mention, as BHF etching is isotropic etching, which not only etched the evaporated SiO_2 but also the thermal-grown oxide (substrate SiO_2) are etched. The etching rate for thermal oxide is around 1.5 nm/sec; it is also essential to understand that the etching rate for the evaporated SiO_2 is much less than the thermal grown SiO_2 .

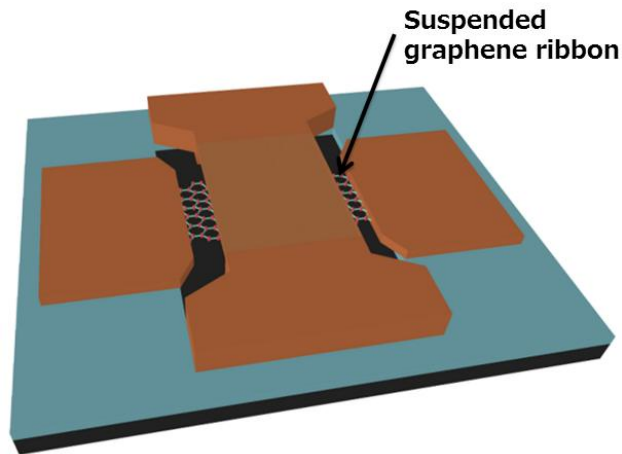


Figure 4.9. Suspended graphene ribbon after the BHF release.

4.4 SUMMARY

In summary, the detailed fabrication process of the graphene-to-graphene NEM contact switch is furnished in step by step manner. The CVD grown graphene layer was used for the fabrication of graphene-to-graphene NEM contact switches. The cleaning of the CVD graphene using the hydrogen annealing (Ar+H₂) is also explained. The hydrogen annealing (Ar+H₂) efficiently removes the PMMA residues from the wet chemical based transfer process. The detailed process information of the EBL exposure for the writing the fine structures are explained. The graphene-to-graphene NEM contact switch fabrication process involves the CVD graphene transfer twice. First on the Si/SiO₂ substrate, fabricated as the suspended beam. The second time, another layer of the CVD graphene is transferred on top the fabricated bottom graphene ribbon by wet chemical based transfer process. The transfer process for the top graphene layer is very crucial one because the top graphene layer is transferred on top of the fabricated device, with very high uneven surfaces. Due to this, the transferred graphene layer is broken very often. In order to avoid this, the transfer process has been optimized. The BHF based wet chemical etching for release the graphene beam also discussed in detail. To prevent the graphene beam to be pulled on to the substrate of the surface due to the capillary forces, the critical point drying was used. The CO₂ based super critical point drying was employed to get the suspended graphene beam.

5 Graphene crossbar device Characterisation

5.1 INTRODUCTION

In this chapter, the interlayer conduction between the two single layer graphene ribbons is studied. Furthermore, this chapter explains the following. Fabrication of graphene-to-graphene crossbar device, Raman spectroscopy of the twisted bilayer system, interlayer conduction in a twisted graphene bilayer system, in-situ annealing effect on the interlayer conduction, as well as the interlayer conduction in the gas (Ar+H₂) environment.

5.2 INTRODUCTION TO CROSSBAR DEVICE

The graphene-to-graphene crossbar device consists of two layers of graphene. In the crossbar device, one layer of graphene (top graphene layer) is transferred on the other layer of graphene (bottom graphene). The base graphene layer and the transferred graphene layer both are twisted to each other by a rotation angle θ [61]. The graphene-to-graphene cross bar device is simply the twisted bilayer cross junction device. Two individual monolayer graphene ribbons form an overlapping cross junction.

The properties of the twisted bilayer system are different from the conventional bilayer system. Graphene bilayer is the very simplest multilayer structure. Perfect graphene bilayers have AB/AA type stacking (Bernal stacking order). However, twisted bilayer graphene consists of two graphene layers rotated with respect to each other. The rotation angle θ can be classified as either commensurate or incommensurate [62]. For commensurate angles, the twisted bilayer graphene forms a crystal with a large lattice vector. Commensurability occurs at a finite set of rotation angles. The energy bands of the twisted bilayer graphene feature the linear dispersion of the momentum, which contrasts the Bernal stacked bilayer. Incommensurate twisted bilayers are not crystalline [63]. The arbitrary twist angle in the graphene bilayer introduces a new kind of electronic properties in the twisted bilayers. In Bloch states, the coherent motion of the electrons is one of the elementary principles of conduction [64]. The coherent conduction between the twisted bilayers is completely suppressed due to the momentum imbalance of Fermi surfaces. In this chapter, we present the in-situ annealing effect of the interlayer conduction in graphene cross junction device. Also, we also studied the impact of the gas ($\text{Ar}+\text{H}_2$) in the interlayer transport. The in-situ annealing technique provides a reliable method to study the influence of temperature on the interlayer transport properties.

5.3 FABRICATION OF GRAPHENE CROSSBAR DEVICE

The fabrication flow of the graphene-to-graphene crossbar device is schematically illustrated in Figure 5.1. We have started with single layer chemical vapor deposition (CVD) grown graphene on Si/SiO₂ as our substrate. We fabricate the alignment marks using the E-beam recipe mentioned earlier in chapter 3 of section 4.3.1. The electrode fabrication was done using the positive tone resist PMMA. The thickness of the metal electrode (Cr/Au) was 70 nm (5nm/65nm). The bottom graphene ribbon with dimensions of 1 μm width and 3 μm length is patterned by E-beam lithography using

negative tone resist hydrogen silsesquioxane (HSQ). During E-beam lithography, the exposed area of the resist cross-links. The exposed area of the resist (HSQ) is converted into SiO₂ and the unexposed area is removed through a development process. We used the MF-319 as the developer. In this way, the bottom graphene ribbon was fabricated using the HSQ. The uncovered Graphene layer was etched in O₂ (10 sccm) plasma. Graphene crossbar device is fabricated by transferring another CVD grown graphene above the bottom graphene ribbon that is covered with SiO₂. The top graphene ribbon with dimensions of 1 μm width and 1.8 μm length is also patterned by E-beam lithography using HSQ. The SiO₂ layer was removed by the wet chemical etching using BHF. The BHF etching duration is 7 seconds. By removing the SiO₂ between the top and bottom graphene, the cross junction is realized. Graphene-to-graphene overlapping area is 1 μm × 1 μm (width and length).

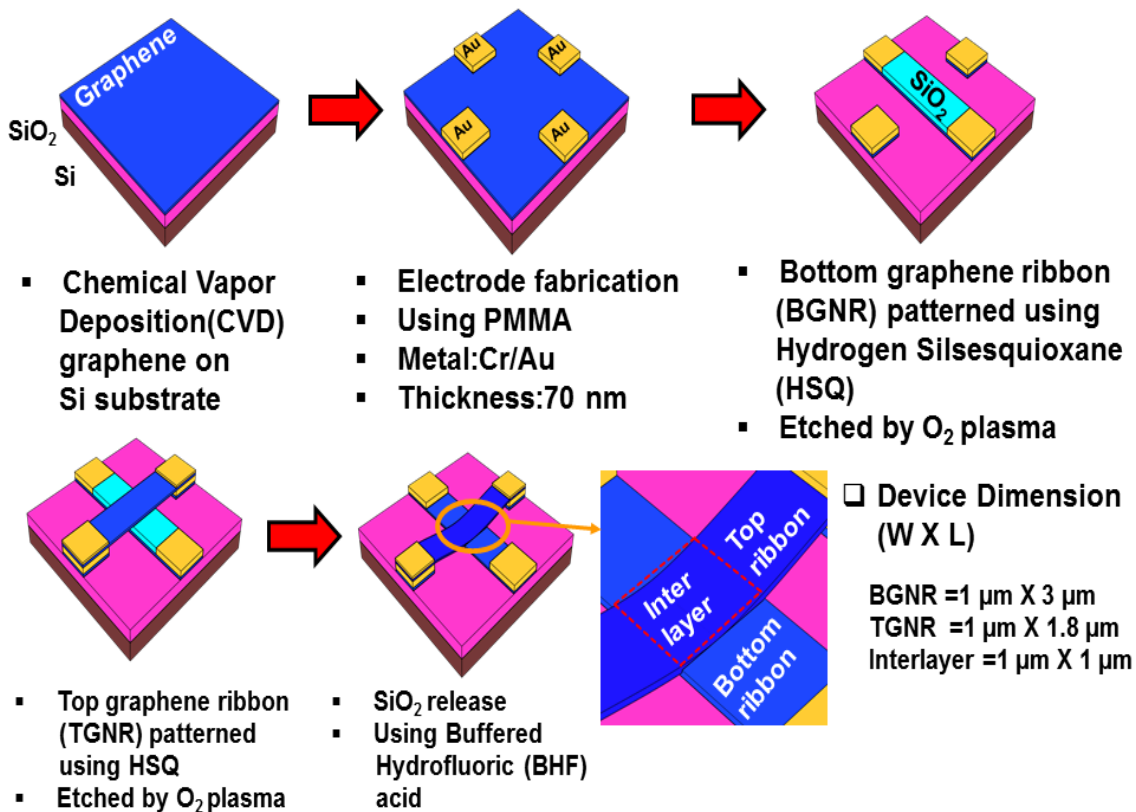


Figure 5.1. Schematic of Fabrication flow of the graphene-to-graphene crossbar device.

5.4 RAMAN SPECTROSCOPY OF CROSSBAR DEVICE

Raman spectroscopy can be used for identify the twisted angle between the graphene layers in the graphene-to-graphene cross junction. The double resonance peak (the 2D peak) of the graphene-to-graphene cross junction appears as a single Lorentzian

peak, which is different from the multiple Lorentzian peaks obtained in the Bernal stacked bilayer graphene. Moreover, the 2D peak is blue shifted in the twisted bilayer graphene due to the reduced Fermi velocity [65].

Figure 5. 2(a) displays the Raman spectra of graphene-to-graphene cross junction device. The significant features observed in the graphene-to-graphene cross bar device are as follows. A distinct D peak which indicates the presence of defects in the cross junction caused by the fabrication process. The G peak appears at the same position $\sim 1583 \text{ cm}^{-1}$ for both single layer and twisted bilayer junction. The Raman 2D peak is observed at 2672 cm^{-1} for the single layer graphene (SLG). The 2D peak is observed at 2684.7 cm^{-1} for the twisted bilayer layer graphene (at the graphene-to-graphene cross junction). The 2D peak is blue shifted about 12.7 cm^{-1} and the FWHM of the twisted bilayer junction 35 cm^{-1} , which confirms that the rotational angle between the bottom and the top layer is ~ 10 degrees [66].

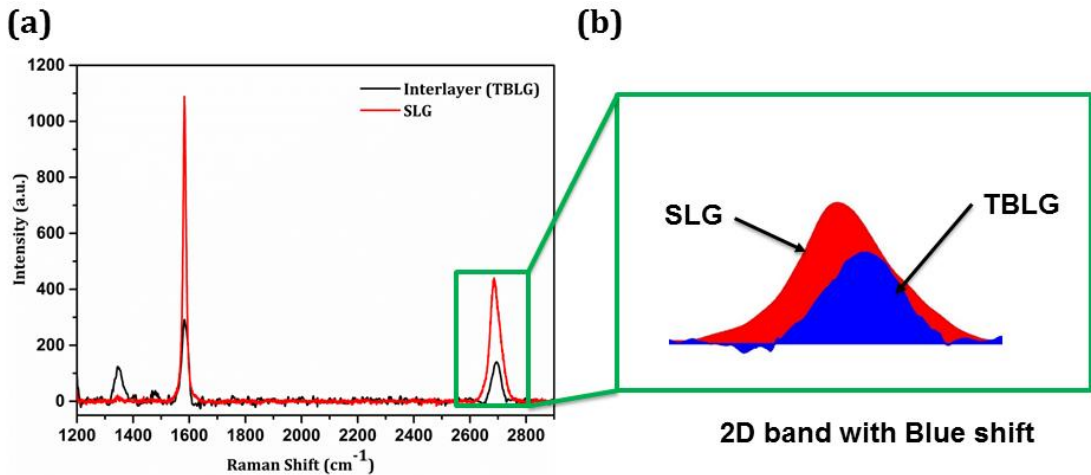


Figure 5.2. (a) Raman spectroscopy of the graphene crossbar device. (b) 2d peak shift of the graphene cross bar device (compared with the single layer graphene SLG).

5.5 ELECTRICAL CHARACTERISATION OF CROSSBAR DEVICE

5.5.1 MEASUREMENT CONFIGURATION OF THE CROSSBAR DEVICE

The interlayer transport measurements of graphene crossbar device was carried out using the four-point resistance technique [67]. The interlayer resistance measurement was done in cross configuration. The measurement setup of the cross configuration is shown in Figure 5.3. The equivalent circuit model of the interlayer resistance i.e. cross junction is provided in Figure 5.4. Figure 5.4a shows the ideal cross junction circuit. The top and the bottom electrodes give the equipotential nodes V_S and V_L (V_D and V_H). The interlayer resistance R_{inter} is same as that of the measured

resistance of the cross junction R_{measured} . The measured resistance of the cross junction is given by $R_{\text{measured}} = (V_H - V_L)/I$; I is the current flow through the cross junction. However, there is a finite amount of the voltage drop across the nodes V_L and V_D owing to the resistance across the width of the contact electrodes. The real cross junction equivalent circuit model is shown in the Figure 5.4b. The negative resistance error occurs [67] when the measured resistance R_{measured} is much less than the interlayer resistance R_{inter} .

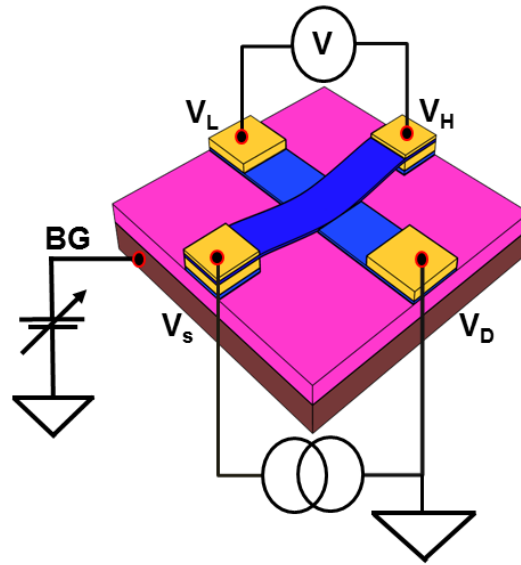


Figure 5.3. Electrical measurement configuration of the interlayer resistance measurement setup.

We have applied a current bias of $1 \mu\text{A}$ for all the interlayer measurement. The terminals V_S and V_D are utilized for the current biasing. The voltage drop across the terminal V_L and V_D are measured. The backgate (BG) voltage is swept from -40 V to 40 V .

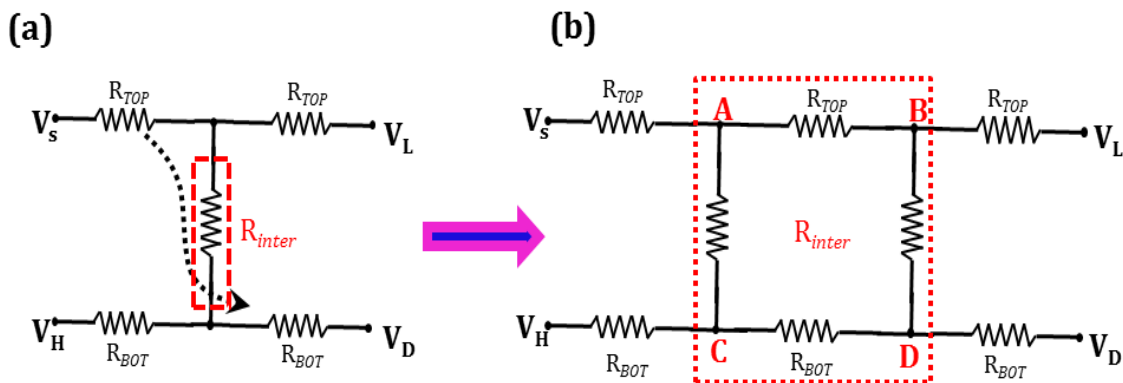


Figure 5.4. Equivalent circuit model of cross junction device. (a) Ideal circuit. (b) Real circuit

5.5.2 RESULTS AND DISCUSSION.

The backgate characteristics of the bottom graphene ribbon (BGNR) and the top graphene ribbon (TGNR) are (as fabricated) shown in Figure 5.5. The back-gate characteristic of both, the bottom graphene ribbon and the top graphene are heavily P-doped. This is mainly due to PMMA residues, the H₂O molecules that remain in the device from the fabrication process [68].

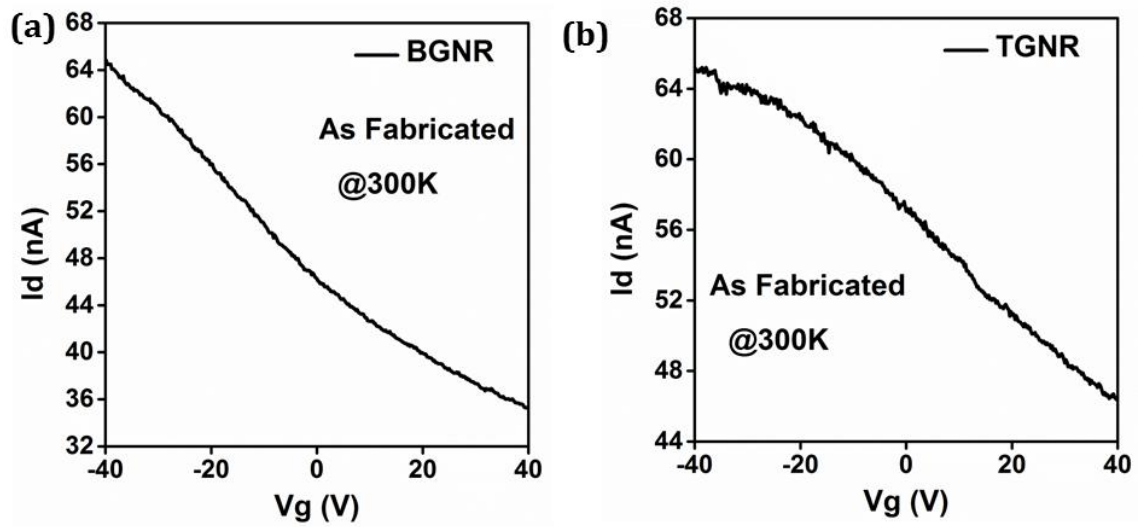


Figure 5.5. Back gate characteristics of the graphene crossbar device. (a) Bottom graphene ribbon. (b) Top graphene ribbon.

The device was annealed in vacuum for 2 hours at 200°C. Figure 5.6 shows the back gate characteristics of the both bottom and the top graphene ribbons. After in-situ vacuum annealing, the charge neutrality point (CNP) is shifted to negative. The vacuum annealing effectively removes the surface contamination in the graphene ribbons. The vacuum annealing also removes the water molecules that are absorbed in between the graphene layer and the SiO₂, effectively reducing the distance between graphene and the SiO₂. A charge transfer from the SiO₂ to graphene occurs because of vacuum annealing. This is the origin of the negative shift in the CNP after vacuum annealing.

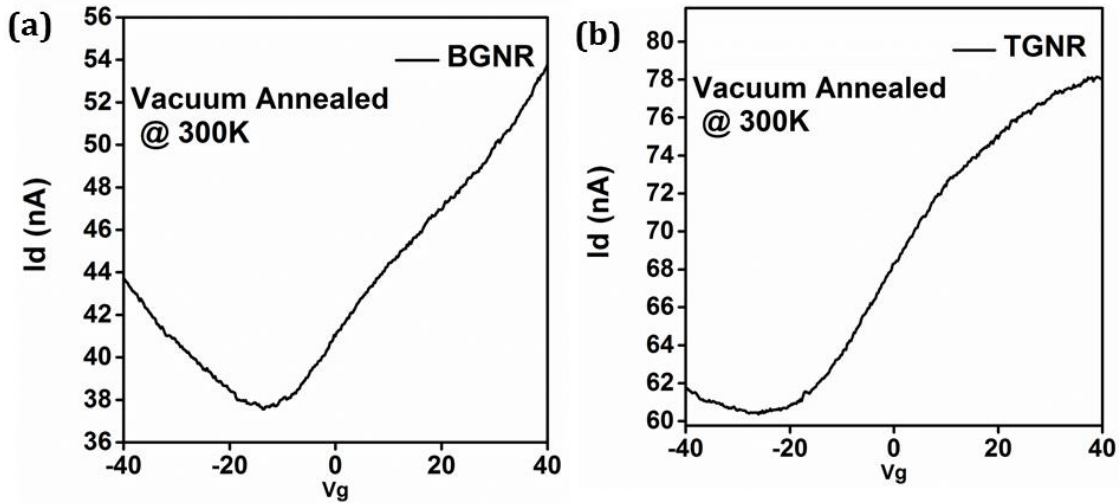


Figure 5.6. Back gate characteristics of the graphene crossbar device after vacuum annealing. (a) Bottom graphene ribbon. (b) Top graphene ribbon.

After vacuum annealing, the device was hydrogen annealed for 3 hours at 275°C. Figure 5.7 shows the back gate modulation of the bottom and top graphene ribbons after the in-situ vacuum annealing. A positive shift has been observed in the CNP for both graphene ribbons. The positive shift in the CNP is attributed to the hydrogen intercalation. The hydrogen intercalation effectively reduces the charge transfer between the SiO₂ and the graphene layer [68], [69].

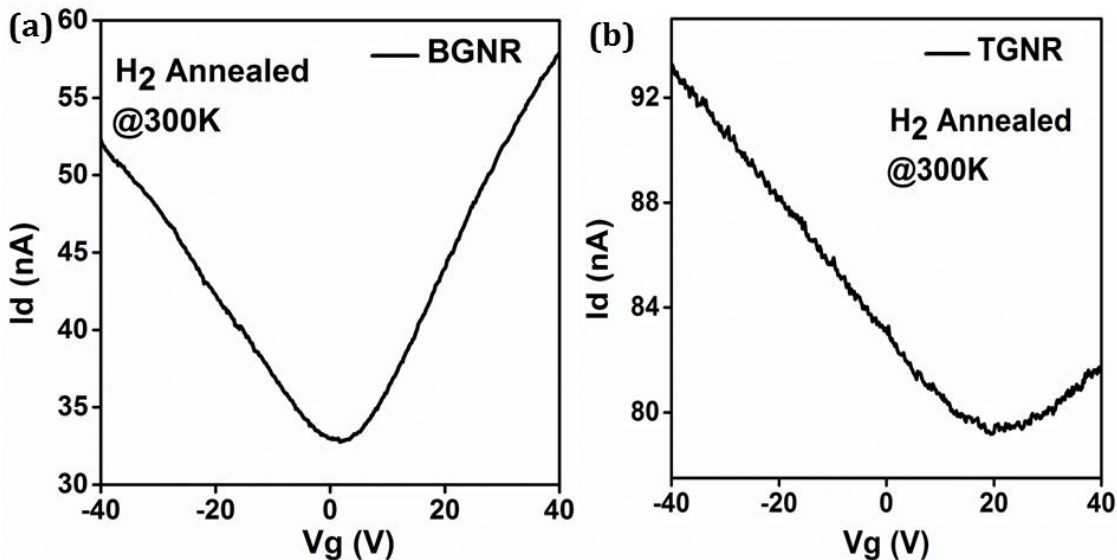


Figure 5.7. Back gate characteristics of the graphene crossbar device after hydrogen annealing. (a) Bottom graphene ribbon. (b) Top graphene ribbon.

Figure 5.8 shows the temperature dependence back gate modulation of the BGNR and TGNR before the in-situ annealing. At low temperature, there is high distortion in the back gate modulation due to the charged impurity scattering.

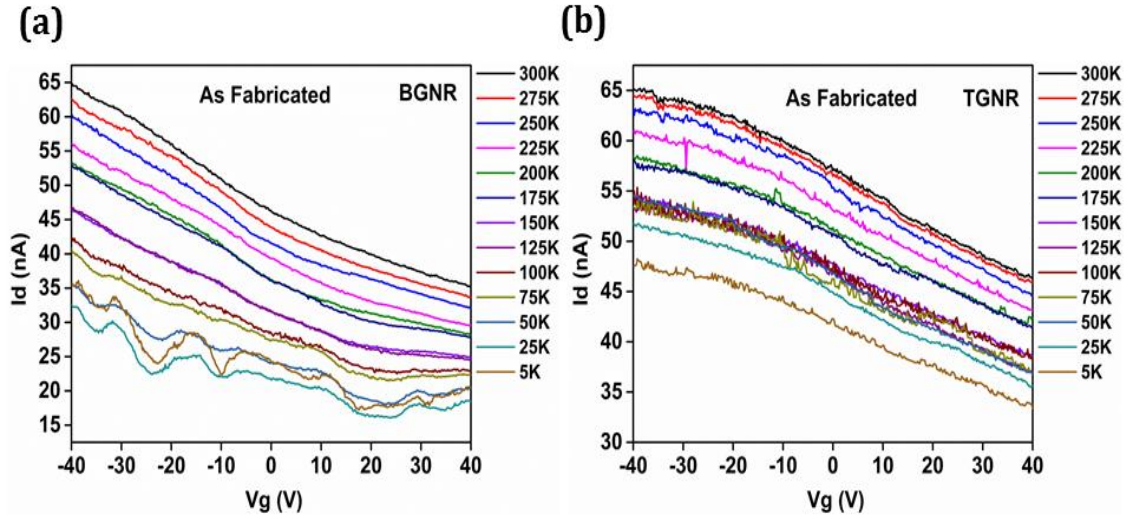


Figure 5.8. Temperature dependence back gate characteristics of the graphene crossbar device as fabricated. (a) Bottom graphene ribbon. (b) Top graphene ribbon.

After the in-situ annealing process (vacuum and the hydrogen annealing) the temperature dependence backgate modulation of both the bottom graphene ribbon and the top graphene ribbon is shown in Figure 5.9. The charge impurity scattering is reduced after the in-situ annealing process [70].

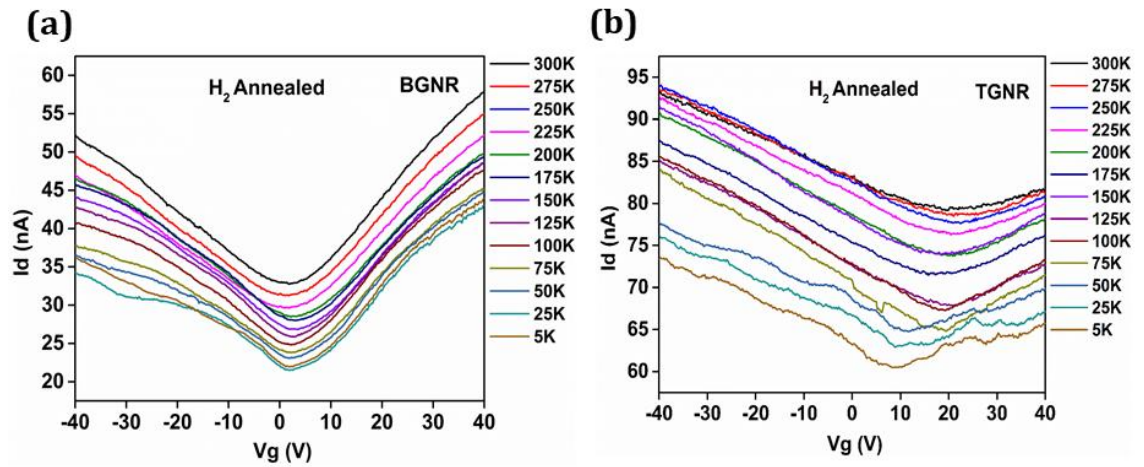


Figure 5.9 Temperature dependence back gate characteristics of the graphene crossbar device after the in-situ annealing process. (a) Bottom graphene ribbon. (b) Top graphene ribbon.

The interlayer resistance of the graphene-to-graphene crossbar device is shown in the Figure 5.10. The interlayer resistance of device as fabricated is illustrated in the Figure 5.10a. The interlayer resistance before in-situ annealing was in the range of $k\Omega$. There is no clear signature of charge neutrality point because the device is heavily p-doped. After the in-situ annealing, the CNP shifts to zero volts. The interlayer resistance after in-situ annealing is shown in the Figure 5.10b.

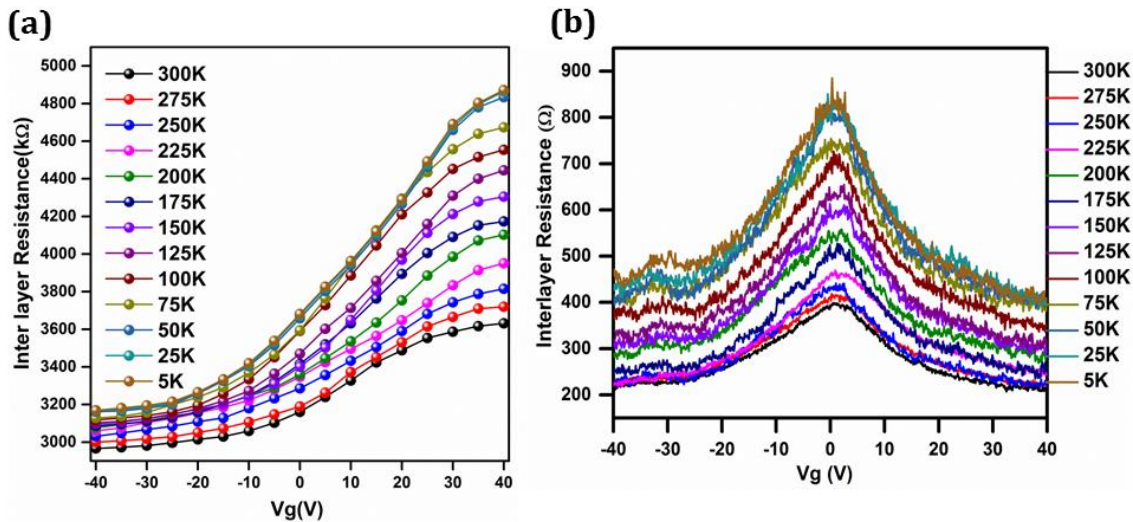


Figure 5.10. Interlayer resistance as a function of the backgate voltage. (a) The interlayer resistance of the graphene crossbar device for the as fabricated sample. (b) Interlayer resistance after the in-situ annealing.

The temperature dependence of the interlayer resistance is shown in Figure 5.11. The interlayer resistance shows a high dependence of temperature. Furthermore, with lowering the temperature, the interlayer resistance saturates beneath a crossover temperature (T^*) ~ 90 K. The negative temperature dependence (semiconducting behavior) is a distinct feature of a twisted bilayer system, and it contrasts with the Bernal-stacked graphene bilayer system (metallic behavior). These results give evidence for incoherent charge conduction between the bottom and the top graphene ribbons [71].

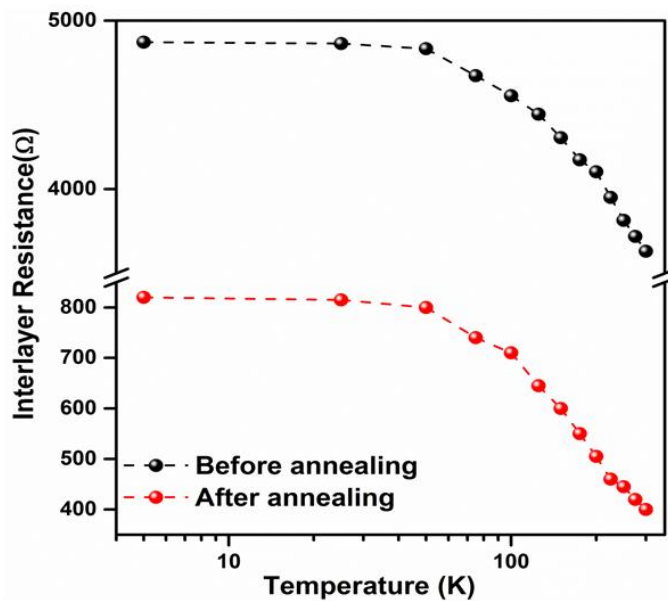


Figure 5.11. Interlayer resistance as a function of the temperature.

At low temperatures, between two graphene layers the interlayer tunneling occurs. Fermi circles of upper and lower graphene layer overlap each other at the extended Brillouin zone. The interlayer tunneling occurs as a result of overlapping between Fermi circles. The interlayer tunneling happens via the excited carriers at higher energies of the overlapped Dirac cones. This is attributed to the temperature independent interlayer conduction at low temperatures [63]. On the other hand, the interlayer conduction is assisted by phonon modes at high temperatures. The phonon abetted tunneling significantly improves the overlap of Fermi circles. At high temperatures, the interlayer conduction was mediated by the phonons [72], [73].

The temperature dependence of interlayer resistance is schematically explained in the Figure 5.12. At low temperatures, the interlayer conduction is mediated by electrons and is almost independent of temperature. At high temperatures, the interlayer conduction is mediated by the phonons and has a strong dependence on the temperature.

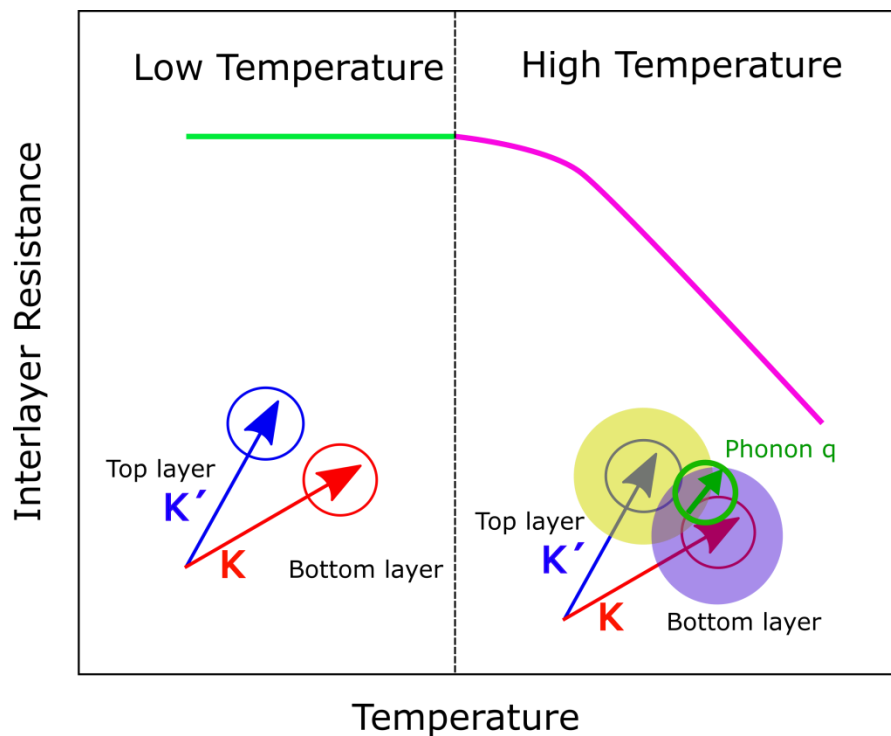


Figure 5.12. Schematic diagram of the temperature dependence of the interlayer conduction mechanism.

The interlayer conduction occurs through the tunneling between the two graphene layers. It is essential to understand the tunneling between the graphene layers. The metal-insulator-metal junction model can describe the interlayer transport between the bottom and top graphene layers. The interlayer tunneling occurs between graphene layers through a potential barrier of height U and width W . The metal-insulator-metal

tunneling model of the graphene layers is schematically explained in the Figure 5.13a. The barrier width w determines the tunneling probability between the Fermi surfaces of the bottom and top graphene layers.

It is evident from the Figure 5.11; the interlayer resistance is reduced significantly after the in-situ annealing process. The effective barrier width W , i.e. the interlayer distance, is reduced by in-situ annealing. Before in-situ annealing, wrinkles are present at the interlayer, and thus the top graphene layer is locally lifted from the bottom layer. Reducing the interlayer distance between two graphene layers simply means reducing the tunneling barrier for carrier transport. The in-situ annealing process effectively reduces wrinkles and in homogeneities at the interlayer junction. The schematic explanation of the effect of in-situ annealing on barrier width of the interlayer tunneling is shown in the Figure 5.13b.

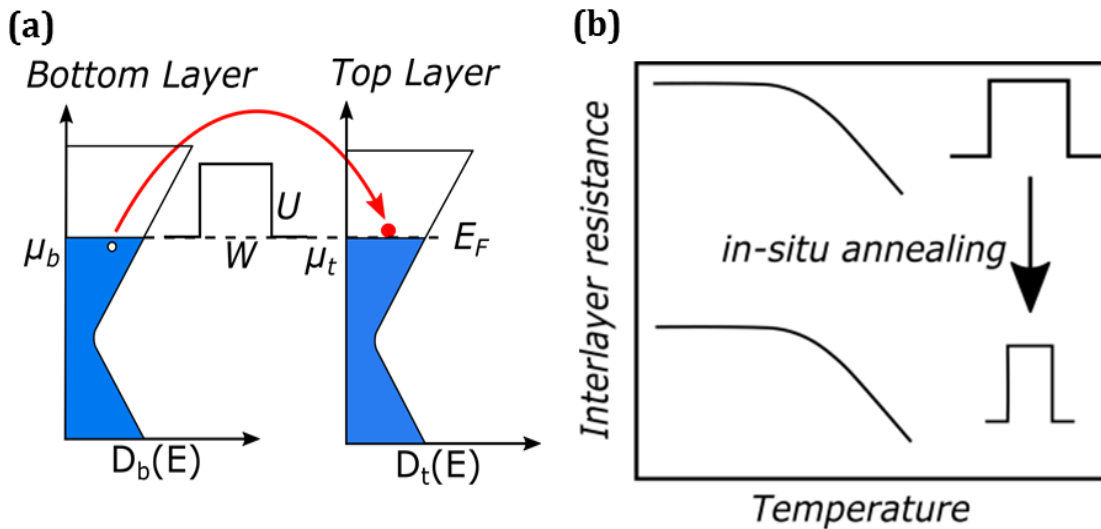


Figure 5.13. Schematic diagram of interlayer conduction. (a) Metal-Insulator-Metal model of interlayer transport. (b) The effect of in-situ annealing in the interlayer transport.

The Figure 5.14 shows the interlayer resistance in the $\text{Ar}+\text{H}_2$ gas environment. The interlayer resistance is increased with lowering temperature. The interlayer resistance increased in the $\text{Ar}+\text{H}_2$ gas environment, this is mainly because the interlayer separation is increased in the $\text{Ar}+\text{H}_2$ gas environment. The tunneling width W is increased in the gas environment.

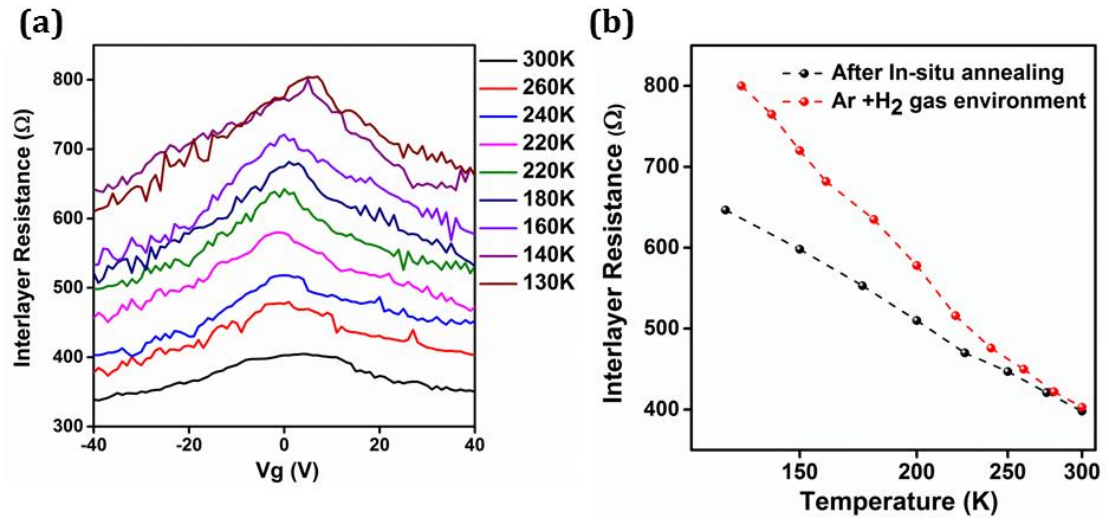


Figure 5.14. (a) Interlayer resistance in the Ar+H₂ gas environment. (b) Interlayer resistance as a function of the temperature in the Ar+H₂ gas environment.

5.6 SUMMARY

The CVD grown was used to fabricate the graphene-to-graphene cross junction device. First, the bottom graphene ribbon was fabricated by using the high resolution negative tone resist HSQ. After that, another layer of the graphene (CVD) was transferred on top of the bottom ribbon by using the wet chemical method. We used FeCl_3 as the copper etchant. The graphene-to-graphene cross junction was realized by removing the SiO_2 between the upper graphene layer and lower graphene layer. Using the graphene-to-graphene crossbar device, the interlayer properties of the two rotated graphene layer was studied. The rotation angle of graphene layer was identified using the Raman spectroscopy. The rotation angle between two graphene layers is ~ 10 degree (Θ). The In-situ annealing measurement was performed for the graphene-to-graphene interlayer crossbar device. We demonstrated the interlayer transport properties of the rotated bilayer graphene. The incoherent charge conduction between twisted graphene layers was observed. The interlayer tunneling is the fundamental conduction mechanism graphene interlayers. Interestingly, at low temperatures the conduction is mediated by the electrons, and at high temperatures the conduction is mediated by the phonons. The clear saturation of the interlayer resistance at the low temperature is the strong observation of the incoherent conduction between the graphene-to-graphene interlayer. The interlayer tunneling between upper and lower graphene layer follows the Metal-Insulator-Metal (MIM) tunneling model. More interestingly, we found that the interlayer tunneling resistance changes significantly after the in-situ annealing. The interlayer layer distance between the two graphene layers changed after the in-situ annealing, in other words, the tunneling width between the bottom and top graphene layer is reduced. In addition, we also studied the effect of the gas on the interlayer transport. We have used $\text{Ar}+\text{H}_2$ (with hydrogen 10%) as the gas environment. We found that the interlayer resistance increases in the hydrogen gas environment. This may be possibly attributed to, the hydrogen interacts with the graphene interlayer. And the hydrogen increases the interlayer tunneling distance.

6 Graphene-to-graphene NEM contact switch: Characterization and Analysis

6.1 INTRODUCTION

In this chapter, the switching characteristic of graphene-to-graphene NEM contact switches is discussed. Graphene NEM contact switches with graphene as the contact material. Owing to the van der Waals (vdW) interaction between the suspended graphene layer and the contact graphene layer, the graphene-to-graphene NEM contact switches exhibit steep switch off characteristics. By using graphene layer as the contact material, the irreversible stiction of NEM contact switch is significantly reduced. The graphene-to-graphene NEM contact switches also exhibit the stable hysteresis in the switching. The stable hysteresis of these switches promises the use of Graphene-to-Graphene NEM contact switches for the memory application.

6.2 DEVICE STRUCTURE AND DIMENSION

In this study, the graphene-to-graphene NEM contact switches are fabricated with Chemical Vapor Deposition (CVD) grown single layer graphene. All the switches reported in this section are double clamped resonator type NEM contact switches. The graphene layer is used as the double clamped suspended active element. The schematic diagram of the graphene-to-graphene NEM contact switch is shown in the figure. It is also worth to mention that, the CVD grown single layer graphene is also used as the contact material as shown in the inset of Figure 6.1.

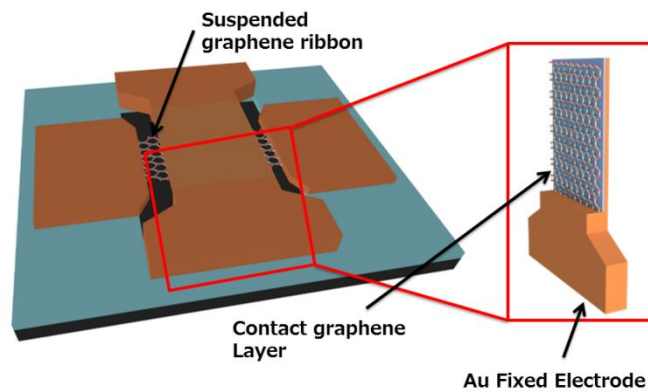


Figure 6.1. Schematic diagram of the graphene-to-graphene to NEM contact switch. The inset shows the fixed gold electrode with graphene as the contact material.

To achieve high mechanical restoring force, the short graphene beam length of $1\ \mu\text{m}$ was used, and the air gap thickness was set to $85\ \text{nm}$. The high mechanical restoring force of the suspended graphene beam ensures the high repeatability of the graphene-to-graphene NEM contact switches. A total of nine devices is considered for the electrical characterization, the electrical characterization of the NEM contact switches discussed in detail in the following section. Table 6.1 gives the complete details of the structural dimension of the fabricated device.

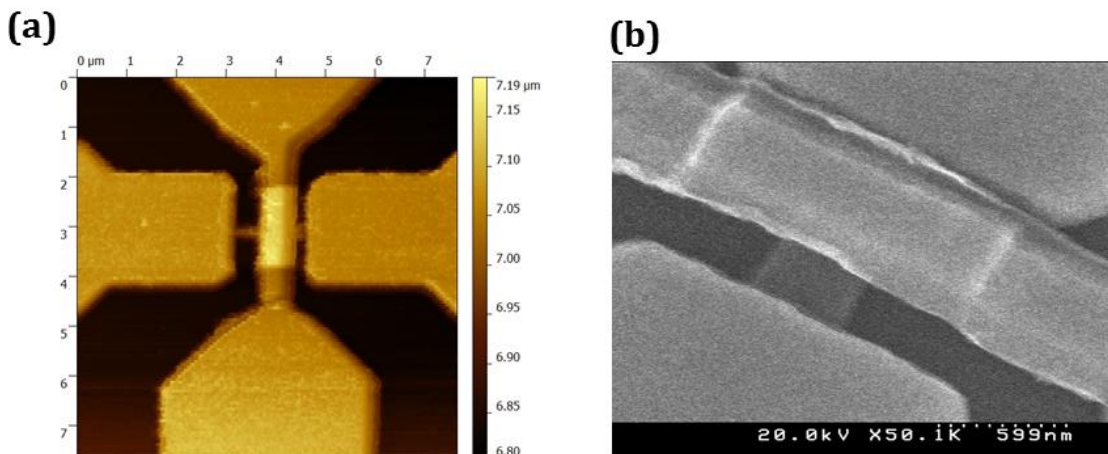


Figure 6.2. (a) AFM image of the device D1. (b) SEM image of the device D1.

Table 6.1. Device parameters of nine measured G_G NEM contact switches.

Device ID	Length (μm)	Width (μm)	Airgap (nm)
D1	1	0.5	85
D2	1	0.5	85
D3	1	0.5	85
D4	1	0.5	85
D5	1	0.5	85
D6	1	0.5	85
D7	1	1	85
D8	1	1	85
D9	1	1	85

6.3 RESULTS AND DISCUSSION

6.3.1 PULL-IN CHARACTERIZATION

The two-terminal measurement configuration characterized the devices listed in Table 6.1. The two terminal measurement configuration was shown in Figure 6.2. The voltage is applied between the top electrode and the bottom electrode, (as labeled indicated in Figure 6.2). The applied voltage was gradually increased from 0 volts, the current between top electrode (with graphene as contact material) and the bottom electrode was measured. The sudden and sharp increase in current was observed for all the electrically characterized graphene-to-graphene NEM contact switches (From D1 to D9). The sharp rise in the current indicated that the double-clamped suspended graphene beam was physically contacted with the top actuation electrode. The compliance of current was set to 200 nA to avoid the Joule heating. The apparent Pull-in effect was observed for all the measured graphene-to-graphene NEM contact switches. The Pull-in voltage highly depended on the structural dimension of the switches.

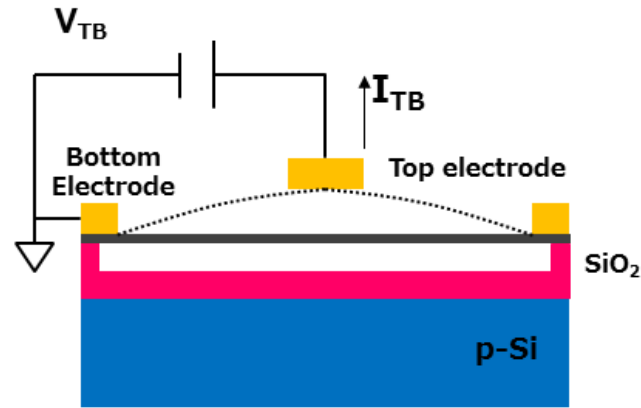


Figure 6.3. Two terminal electrical measurement configuration.

The typical measured pull-in/ pull-out switching characteristics of the graphene-to-graphene NEM contact switch was shown in Figure 6.3. It is evident from the figure 6.3 that the graphene-to-graphene NEM contact switches shown very sharp pull-in. Moreover, stable on current with a steep switching slope (transition from off state to on state), low off state current as well as the steep off switching (transition from on state to off state). The physical condition of the suspended graphene beam in the off state and the on state is illustrated in the inset of Figure 6.3. The switching cycles of all the measured devices are shown in Figure 6.4 and 6.5. Each device exhibit different switching cycles. It is worth to mention that, switching cycle is nothing but the combination of both pull-in sweep (forward sweep) as well as the pull-out sweep (reverse sweep) of the applied voltage

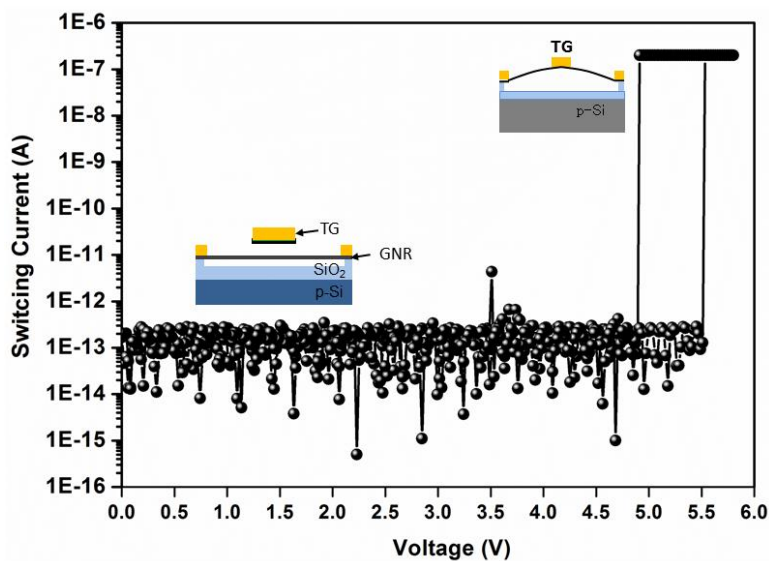


Figure 6.4. Typical switching characteristics of the graphene-to-graphene NEM contact switch. (First switching cycle of device D1)

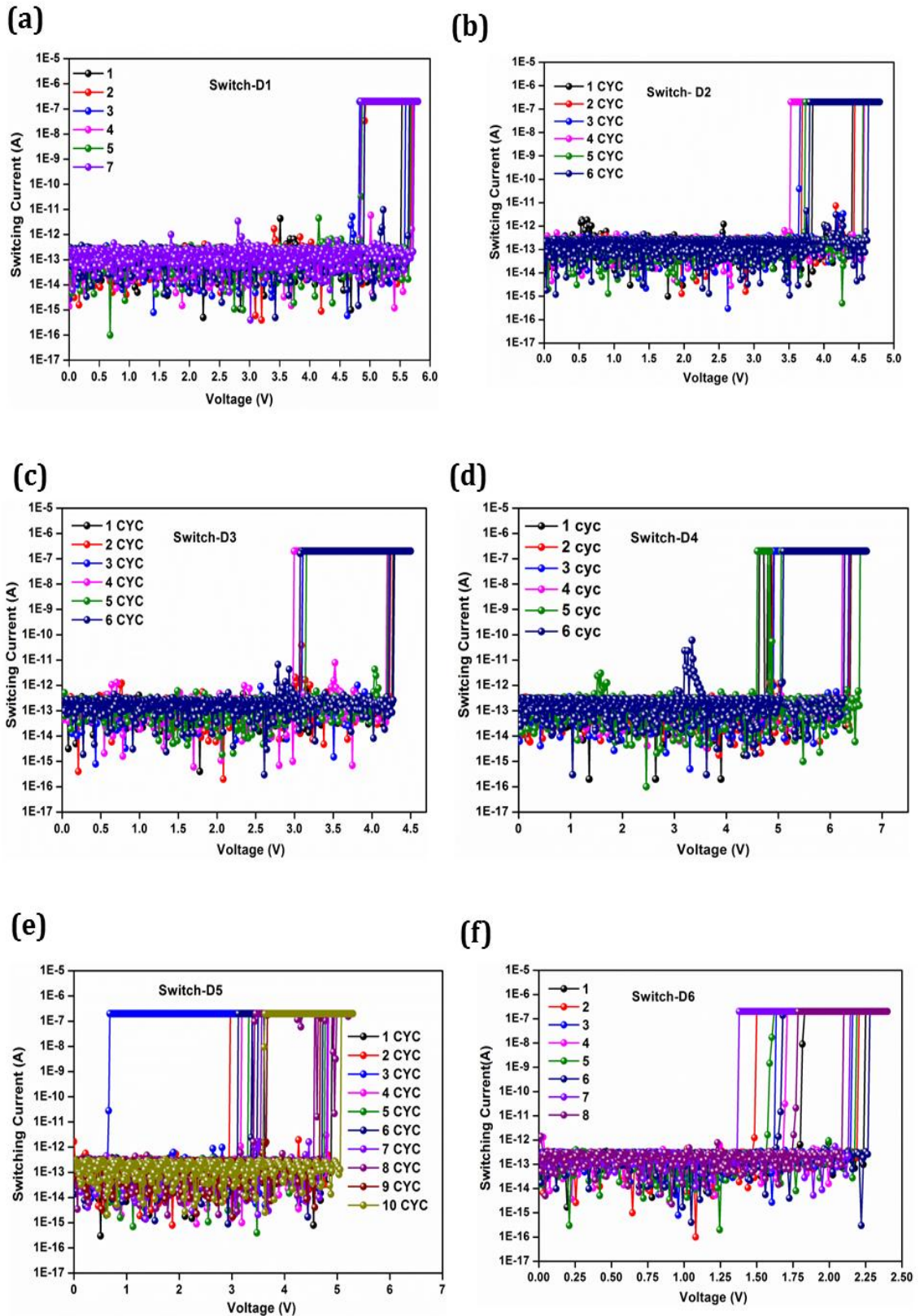


Figure 6.5. Switching characteristics of graphene-to-graphene NEM contact device (device D1 to D6 is shown)

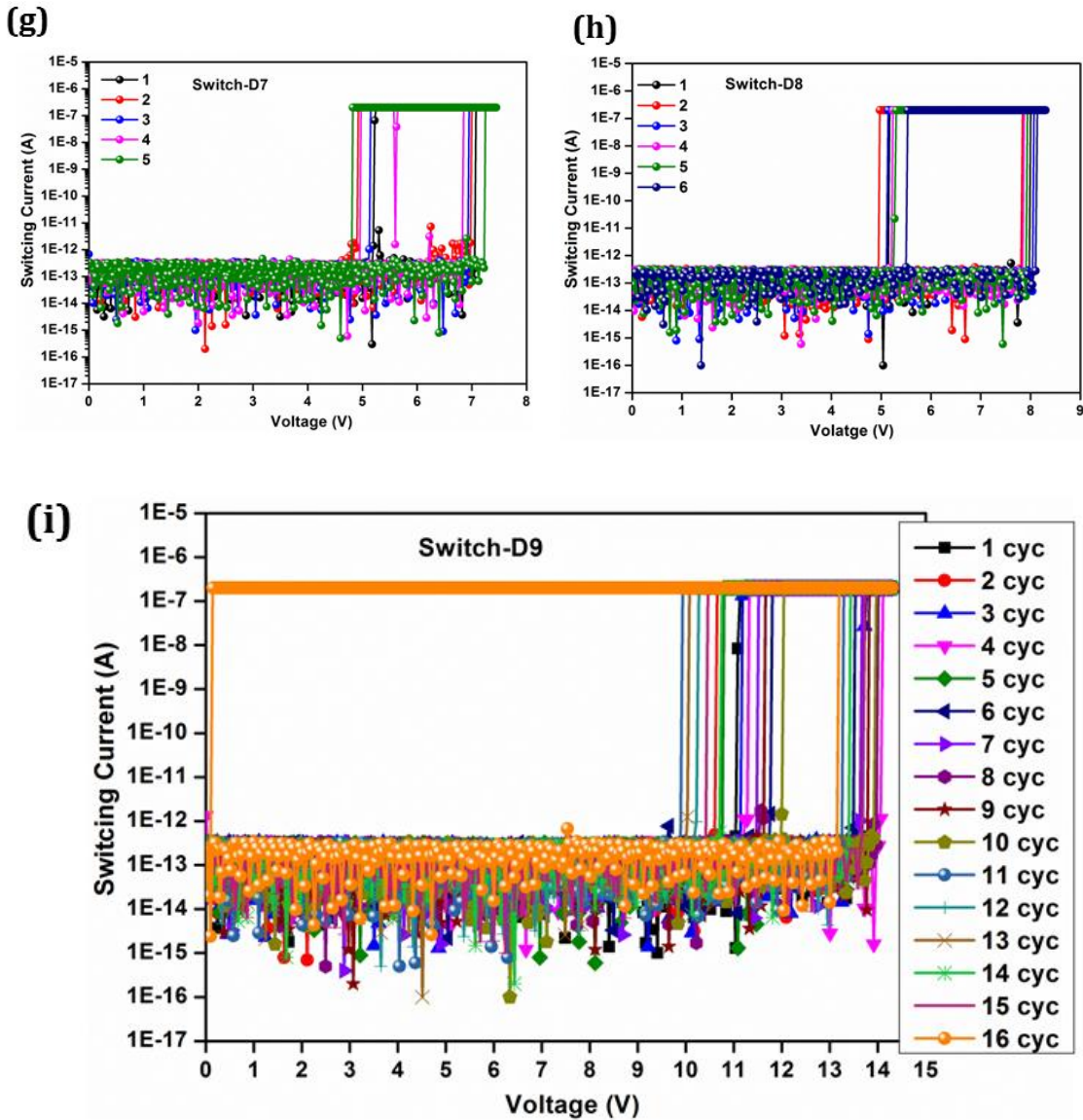


Figure 6.6. Switching characteristics of graphene-to-graphene NEM connect the device (device D7 to D9 is shown).

Even though all the measured devices (from D1 to D9) give very sharp rise in the switching response with steep switching slope, the pull-in voltage is not very stable. This is because of the degradation in mechanical properties of the suspended (graphene beam) due to the high switching speed of the NEM contact devices. To obtain the mean value of the pull-in voltage, the statistical average of the pull-in voltages is carried out. The switching cycles of the NEM contact switch are also different device to device. This is attributed to the structural dimension variation of the each device.

6.3.2 STATISTICAL ANALYSIS OF THE PULL-IN VOLTAGE.

The statistical histograms of the pull-in voltage in all the measured devices (From D1 to D9) are shown in Figure 6.6 and the Figure 6.7. The red lines in the histogram are Gaussian distributions.

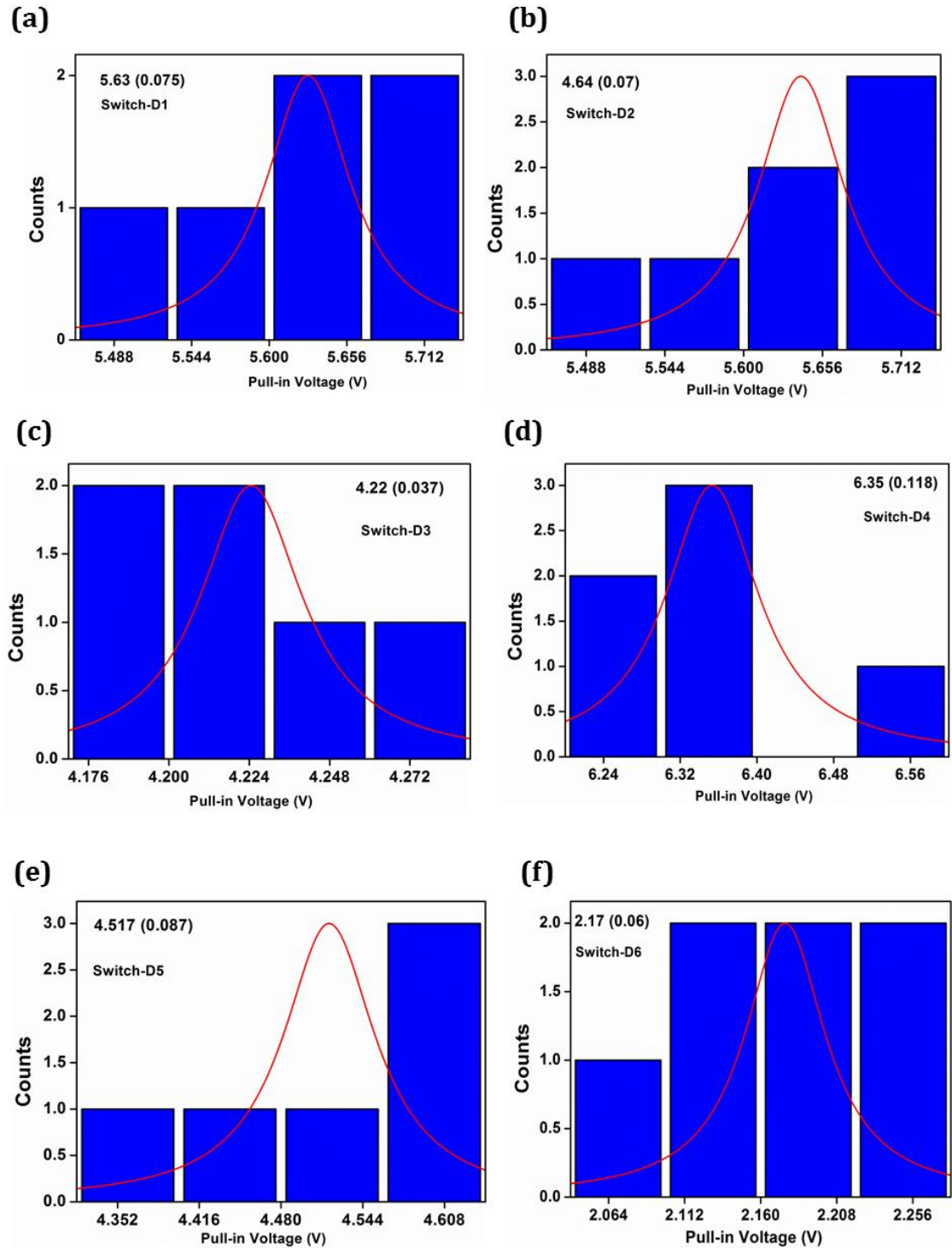


Figure 6.7. Statistical average of the Pull-in voltage for device D1-D6.

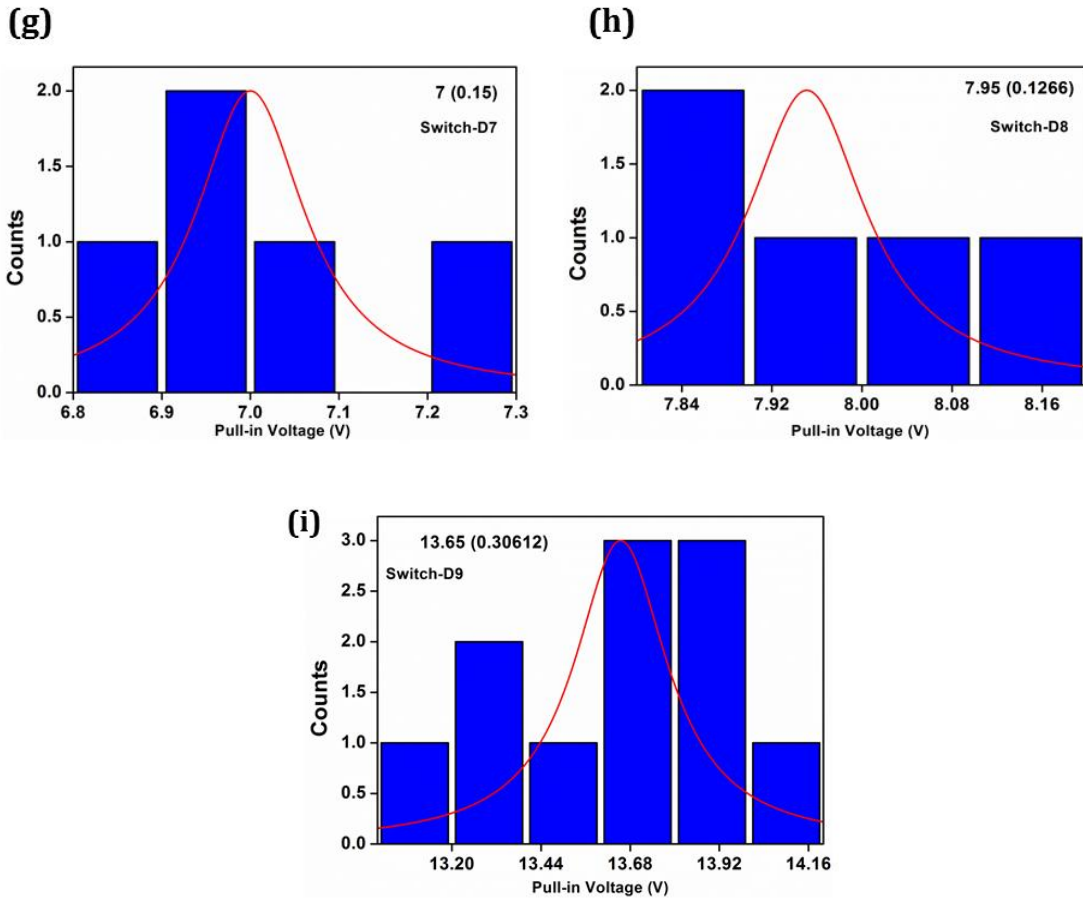


Figure 6.8. Statistical average of the Pull-in voltage for device D7-D9.

Table 6.2. Statistical analysis of the pull-in voltages of all devices.

Device ID	Mean value of the V_{pi}	Standard deviation in V_{pi}
D1	5.63	0.07
D2	4.64	0.075
D3	4.22	0.037
D4	6.35	0.118
D5	4.517	0.087
D6	2.17	0.06
D7	7	0.15
D8	7.95	0.1266
D9	13.65	0.30612

The statistical averages of the pull-voltages (V_{pi}) of all the devices are furnished in the following Table 6.2. From the statistical analysis, it is very evident that all measured devices exhibit low deviation in the pull-in voltages. The deviation in the pull-in voltage varied from a minimum of ~ 0.07 to ~ 0.31 . It is essential to note that, the statistical average highly depends on the number of entries, i.e. the number of switching cycles. Electrical characterizations of all the devices are summarized in Table 6.3.

Table 6.3. Summary of electrical characterization of all the devices.

Device ID	Pull-in voltage (V)	Pull-out voltage ~ (V)	Switching Slope (mV/dec)	ON/OFF ratio
D1	5.63	4.7	<10	$>10^5$
D2	4.64	3.8	<10	$>10^5$
D3	4.22	3.1	<10	$>10^5$
D4	6.35	4.95	<10	$>10^5$
D5	4.517	3.75	<10	$>10^5$
D6	2.17	1.5	<10	$>10^5$
D7	7	5.2	<10	$>10^5$
D8	7.95	5.1	<20	$>10^5$
D9	13.65	11.2	<10	$>10^5$

From the Table 6.3, all the measured NEM contact switches are shown very steep switching slope; almost all the devices are having the switching slope <10 mV/dec. The reported switching slope is much less than the subthreshold switching slope of the conventional CMOS MOSFET device (60 mV/dec @ 300 K). It is also worth to mention that, all the graphene-to-graphene NEM contact switches are measured at the room temperature and high vacuum environment. All the devices also show the prominent on/off ratios, $>10^5$ order magnitude change in the switching current. The Figure 6.9 summaries the electrical performance of the all the devices. The Figure 6.9a illustrates the information of the pull-in voltage and the number switching cycles of various

devices. The pull-in voltage is varied each devices, even for the devices with similar structural dimension. And the numbers of switching cycles are also changed for each device. The Figure 6.9b illustrates the operating voltage window of the devices from D1 to D9. All the devices exhibit, the pull-in voltage window of less than two volts. The operating voltage window is simply referred as the hysteresis of the NEM contact switching devices. Hysteresis in the NEM contact switch is caused by the surface adhesion forces in the contact between the suspended beam the contact graphene. The hysteresis is one of the key parameters for evaluating the switching performance of the NEM contact switch. The graphene NEM contact switches exhibit small hysteresis mainly due to the contact graphene. Owing to the graphene to graphene contact nature the surface adhesion forces are significantly reduced in the graphene-to-graphene NEM contact switches.

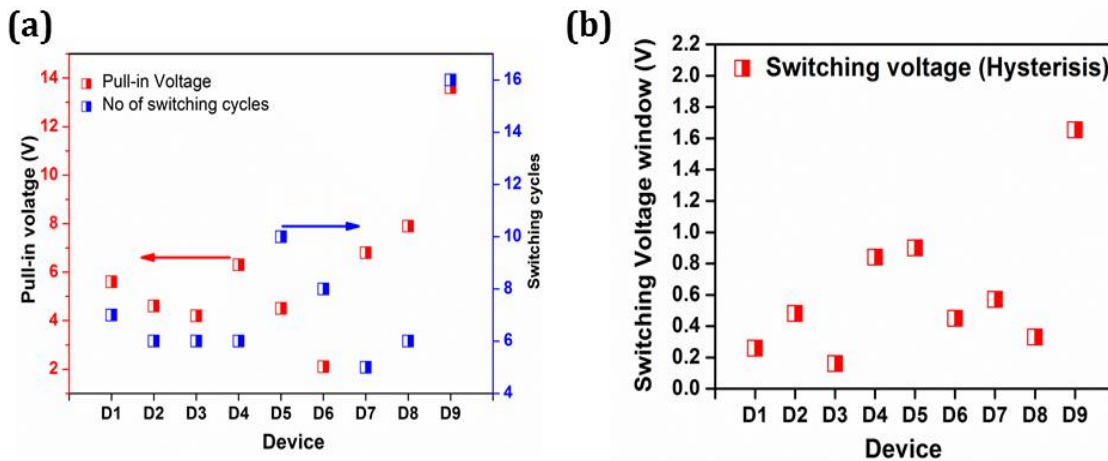


Figure 6.9. Summary of the device D1- D9. (a) Pull-in voltage and the switching cycle of the devices from D1 to D9. (b) The switching voltage window of the devices from D1 to D9.

6.3.3 PULL-IN VOLTAGE VARIATION IN THE DIFFERENT DEVICES WITH SIMILAR STRUCTURAL DIMENSION.

In this section, the pull-in voltage variation between different devices with similar dimension will be discussed. Consider the device D1 and devices D2, both of the devices are having the same structural dimension. The length, width and the Airgap thickness of both devices are 1 μm , 0.5 μm , and 85 nm respectively. The pull-in voltage of the device D1 is 5.6 V, and the pull-in voltage of the device D2 is 4.6 V. One has to understand the variation in the pull-in voltages of devices with similar structural

dimension. The SEM images of the various devices with similar structural dimension are shown in the Figure 6.10.

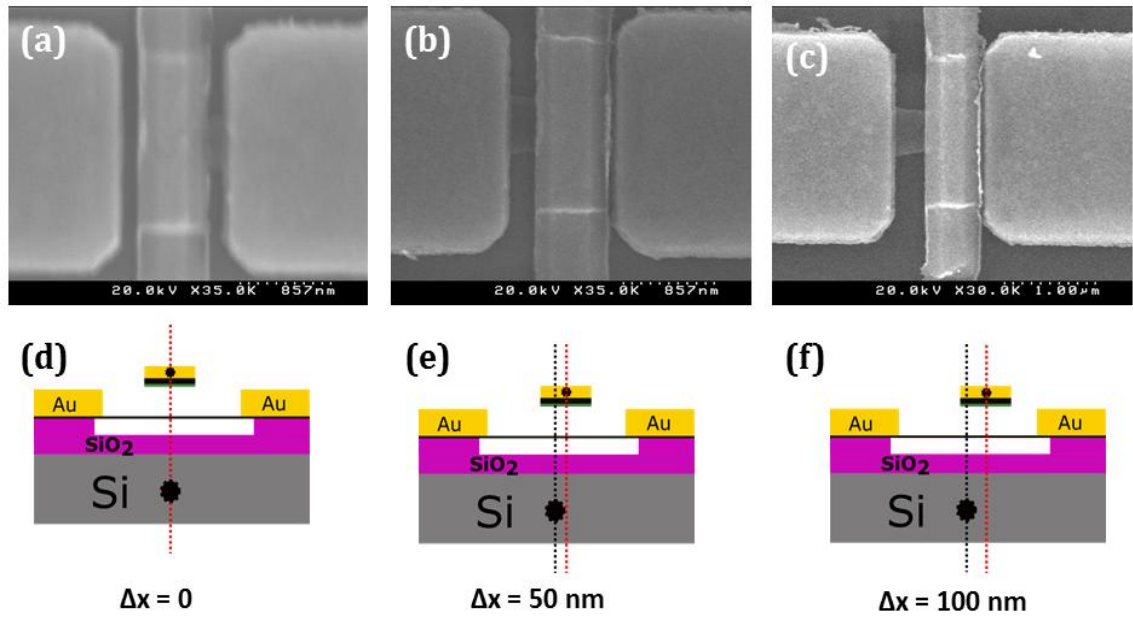


Figure 6.10. (a-f) SEM images of the different devices with a misalignment induced shift in the actuation electrode. (d-f) Schematic representation of the Actuation electrode shift in different devices.

It is very obvious from the SEM images of the Figure 6.10, there is a clear shift in the actuation electrode. The Figure 6.10a shows no misalignment that is the center of the substrate is aligned with the center of the actuation electrode. No misalignment shift condition is schematically represented in Figure 6.10d. From the figure 6.10b, it is evident that the actuation electrode is shift ~ 50 nm in the positive X direction and Figure 6.10c shows the shift of 100 nm. To understand the impact of the actuation electrode shift, the FEM simulation was conducted. The Figure 6.11a shows the 3D schematic of the graphene NEM contact switch. The Figure 6.11b illustrates the pull-in condition of the graphene NEM contact switch. The FEM simulation is conducted with three different values of the ΔX . The ΔX is nothing but the shift of the misalignment in the Au fixed electrode. The table 6.4 gives the misalignment induced shift causes the pull-in voltage variation in the graphene NEM contact switches. The pull-in voltage is increased as the misalignment is increased. Qualitatively the pull-in voltage variation in the devices with similar structural dimension is caused by the misalignment induced shift in the actuation electrode fabrication.

Table 6.4. Misalignment induced pull-in voltage variation

Misalignment (ΔX)	Pull-in (V)
0	3.6
50 nm	4.2
100 nm	4.6

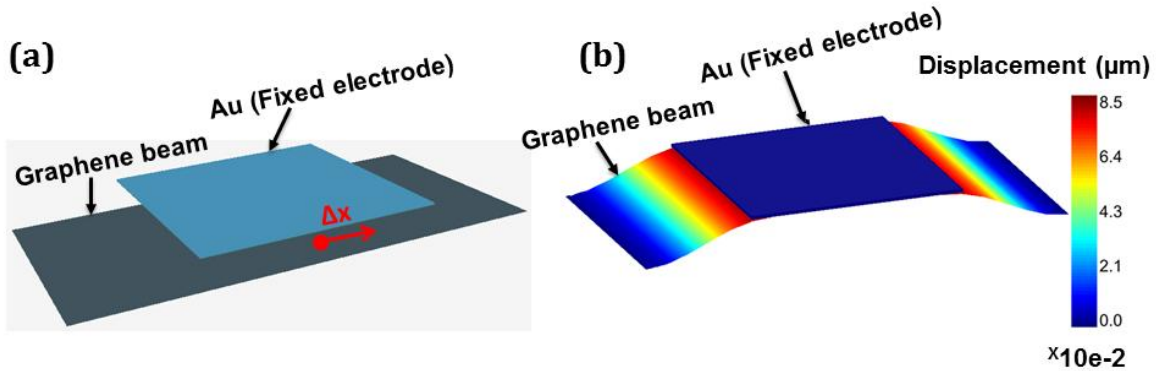


Figure 6.11. The geometry of NEM switch A. (a) Initial structure of double-clamped graphene beam NEM switch with a top metal electrode. (b) Pulled-in state of the graphene beam; color bar indicates the relative displacement with respect to the initial condition.

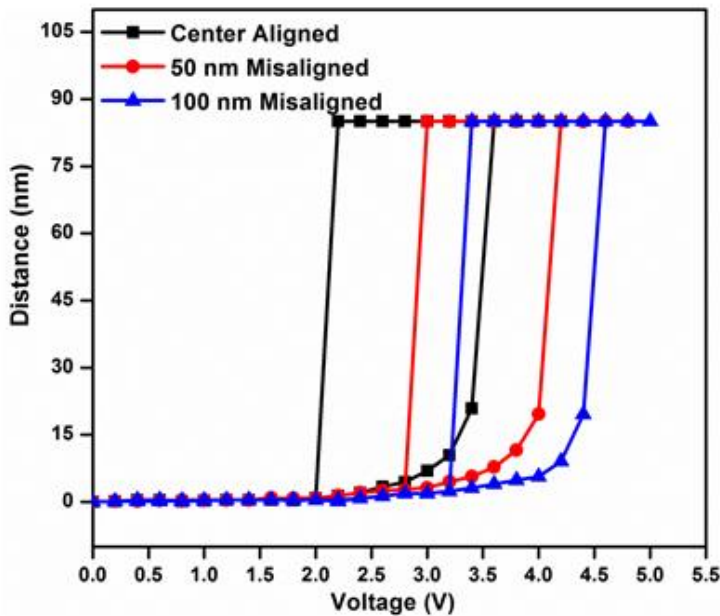


Figure 6.12. Switching characteristics of the graphene NEM contact switch with different misalignment.

6.3.4 FLUCTUATION IN THE PULL-IN AND PULL-OUT VOLTAGES IN DIFFERENT CYCLES OF SWITCH.

The other important aspect of the graphene NEM contact switch is voltage fluctuation both in pull-in cycle and the pull-out cycle. To understand the pull-in/pull-out voltage fluctuation consider the device D9. The device D9 works up to 16 switching cycles. The electrical characterization of the device D9 is shown the Figure 6.12.

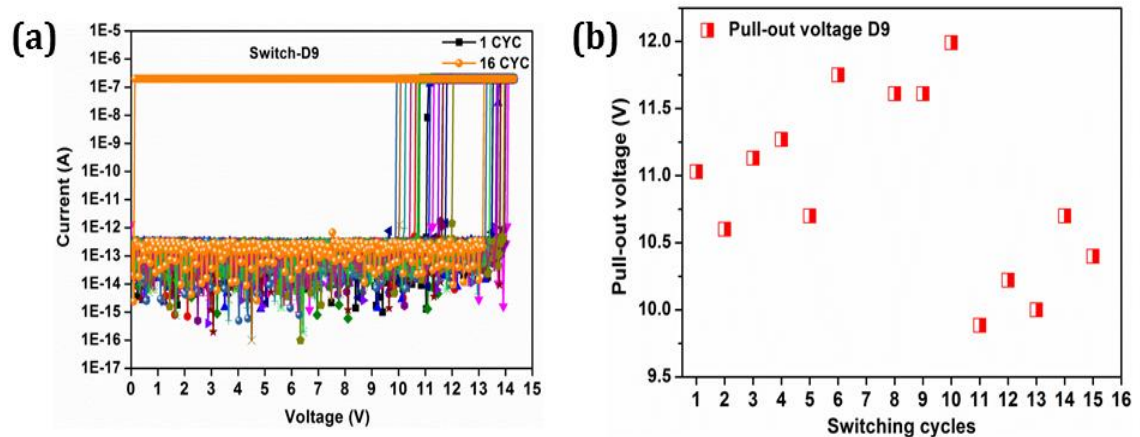


Figure 6.13. (a) Switching characteristics of the device D9. The pull-out voltage fluctuation of the device D9.

The pull-in voltage fluctuation among the various switching cycles is ~ 0.3 V. The fluctuation in the pull-in voltage is maybe due to the under-etching of the SiO_2 during the BHF wet etching. The Figure 6.12b shows the pull-out voltage fluctuation. All the graphene NEM contact switches are fabricated using the CVD grown graphene. The mechanical quality of the CVD graphene influences the switching characteristics of the graphene NEM contact switch. The defects, voids and the grain boundaries are present in the CVD graphene, and all these will change each growth process. The mechanical quality of the CVD graphene beam may degrade in due to the high-speed switching of NEM contact switch. The contact graphene may be broken during the transfer process. This also significantly influences the switching characteristics if the graphene NEM contact switches.

6.3.5 SUB 1-V GRAPHENE NEM CONTACT SWITCH

The pull-in voltages are reduced significantly by reducing the air gap thickness. The Figure 6.14a shows the AFM image of the graphene ribbon with deposited SiO_2 . The thickness of the SiO_2 is ~ 28 nm. Line profile of the SiO_2 thickness is extracted along the black line as shown in the Figure 6.14a. The Figure 6.14b illustrates the line profile of the SiO_2 .

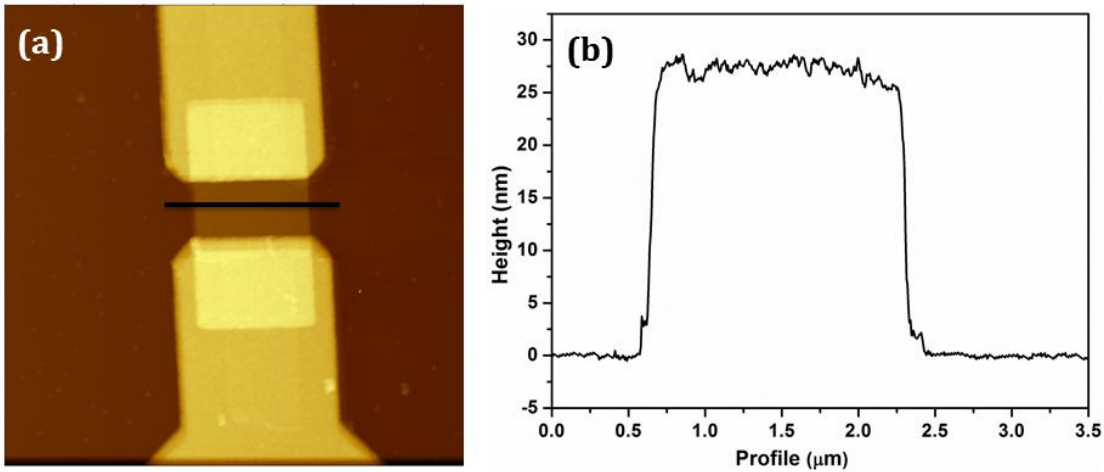


Figure 6.14. (a) AFM image of the graphene ribbon with SiO_2 deposition. (b) AFM line profile of the after SiO_2 deposition.

The electrical characterization was conducted for the device with air gap thickness of 28 nm. The electrical characterization of the two different devices is shown in the Figure 6.15.

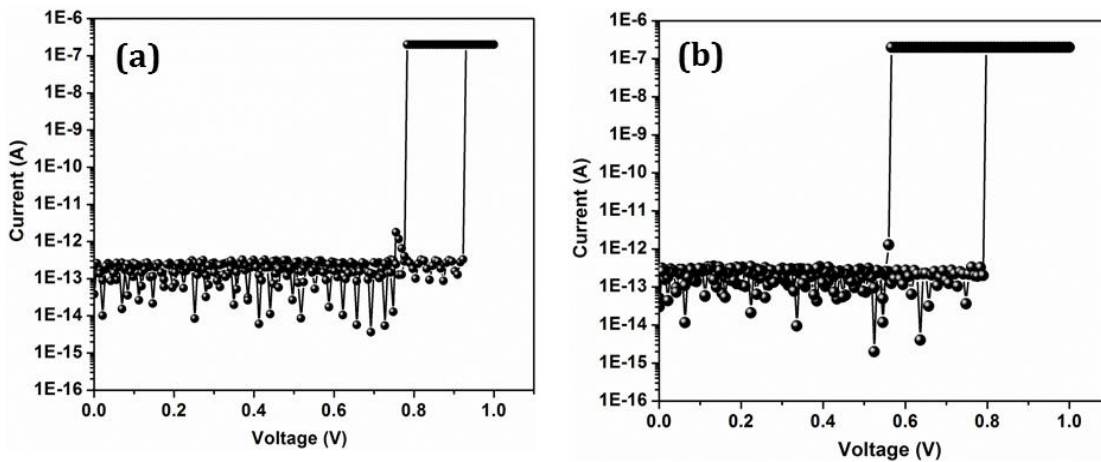


Figure 6.15. Switching characteristics of the sub 1-V switch. (a) Switch with Pull-in voltage of 0.92 V. (b) Switch with pull-in voltage of 0.8 V.

The Figure 6.15a illustrates the graphene NEM contact switch with pull-in voltage of 0.92 V. Figure 6.15b shows the NEM contact switch with pull-in voltage of 0.8 V. Both of the switches are with same structural dimensions with a length of $1 \mu\text{m}$ and the width of $0.5 \mu\text{m}$ and the air gap thickness is around 28 nm. Both switches exhibit clear pull-in and pull-out voltages within the sub one voltage realm. Even though the switch is having the same structural dimension the hysteresis of the switches are not same. The switching voltage window (hysteresis) significantly relies on the contact nature of the switch.

6.3.6 PULL-OUT CHARACTERISATION

The conventional NEM contact switches, as well as the graphene based NEM contact switches, are faces stiction problem. There are several failure modes in the NEM contact switches, such as wear, tear as well as the damage by the electrical discharges. The failure of the NEM contact switch is caused by the surface adhesive forces between the fixed element and the active element (suspended beam). The applied voltage between the active and fixed element is sufficiently increased, the active element pulled on to the fixed element, and gives the sharp rise in the current. When the applied voltage between the active and the fixed element is reduced, the active element should release from the fixed element, and subsequently, the switch should open. However, in general, the adhesive forces acting between the active element and the fixed electrode keep the switch closed even after the applied voltage is completely reduced to zero volts. This is known as stiction. Stiction is an irreversible process. For graphene based NEM contact switches, the stiction is considered as one of failure mode. Particularly for the graphene based NEM contact switches, the stiction is the primary failure mode. Due to the stiction, the graphene based NEM contact switches, in general, does not exhibit clear pull-out characteristics.

Figure 6.9 illustrates the graphene NEM contact switch with gold (Au) as the actuation electrode. The Figure 6.9a shows the pull-in condition of the graphene NEM contact switch, in which the graphene beam is pulled on to the surface of the gold electrode. The Figure 6.9b shows the pull-in curve of the graphene NEM contact switch. Figure 6.9c shows the pull-out curve of the graphene NEM contact switch. There is no clear pull-out.

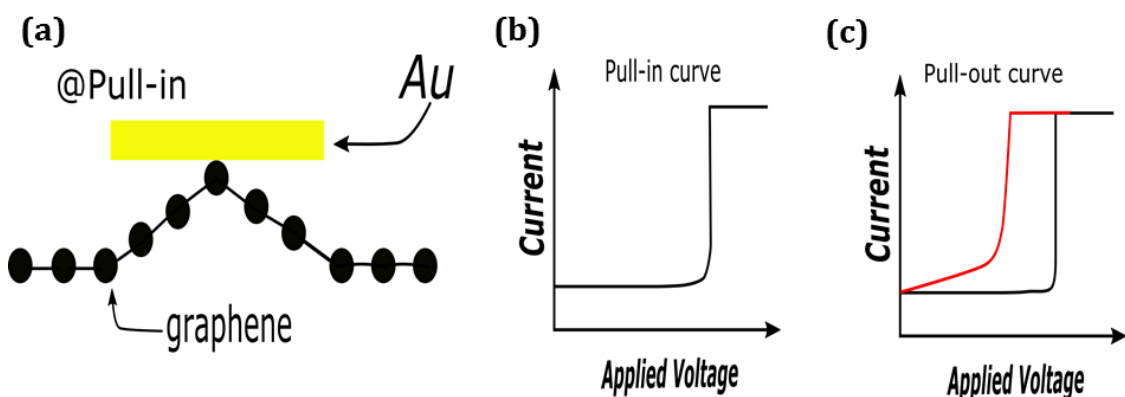


Figure 6.16. Surface adhesion in graphene- gold surface. (a) Graphene beam is pulled on to the surface of the gold. (b) Pull-in characteristics of the NEM contact switch with Au as contact material. (c) Typical pull out characteristics of the pull-out in the NEM contact switch with Au as the contact material.

The graphene NEM contact switch with gold as the contact material fails within very few cycles, and exhibit no clear pull-out characteristics. This is mainly due to the formation of the chemical bond formation between the carbon and the gold atoms. The chemical bond cannot be breakable, so the graphene beam is stick to the gold surface permanently. And the subsequently this will lead to the failure of the NEM contact switch.

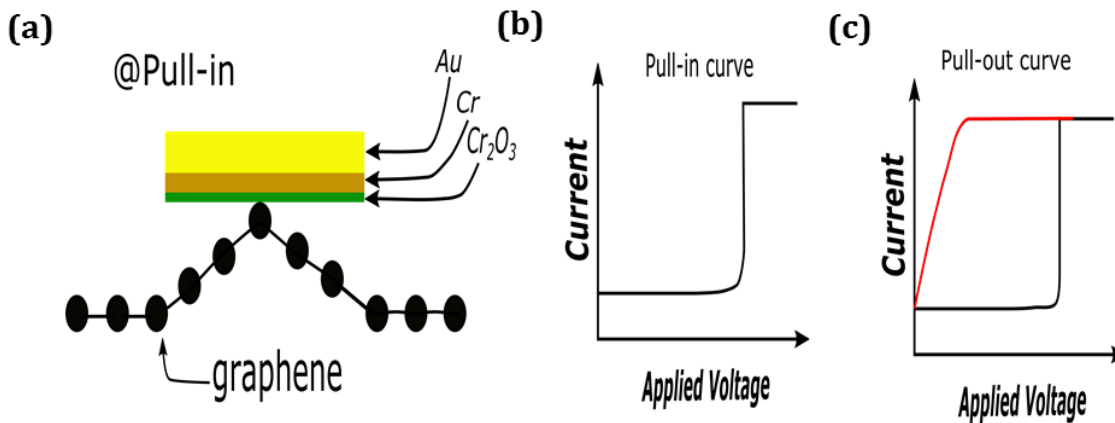


Figure 6.17. Surface adhesion in graphene- Cr₂O₃ surface. (a) Graphene beam is pulled on to the surface of the Cr₂O₃. (b) Pull-in characteristics of the NEM contact switch with Cr₂O₃ as contact material. (c) Typical pull out characteristics of the pull-out in the NEM contact switch with Cr₂O₃ as the contact material.

The Figure 6.10 illustrates the graphene NEM contact switch with Cr₂O₃ as the contact material. The Figure 6.10a shows the pull-in condition of the graphene NEM contact switch, in which the graphene beam is pulled onto the surface of the chromium oxide Cr₂O₃. The chromium oxide Cr₂O₃ is formed during the fabrication process by natural oxidation of the chromium. This chromium is highly disordered and amorphous. This naturally formed chromium oxide has a high amount of defects. These defects act as the charge storage traps. The Figure 6.10b shows the pull-in curve of the graphene NEM contact switch with chromium oxide Cr₂O₃ as the contact material. Figure 6.10c shows the pull-out curve of the graphene NEM contact switch. There is no clear pull-out. The amorphous and disordered surface of the Chromium oxide Cr₂O₃ also leads to the highly uncontrolled pull-out operation and subsequently results in the stiction of the graphene beam to the surface of Chromium oxide Cr₂O₃ contact This is due to the charge storage in the chromium oxide Cr₂O₃. The highly defected Cr₂O₃ layer act as the storage traps.

To achieve the clear pull-out in graphene based NEM contact switches. The graphene is used as the contact material. As the graphene is atomically flat and the

graphene-to-graphene is controlled by the van der Waals (vdW) interaction. The graphene is used as the anti-stiction contact material.

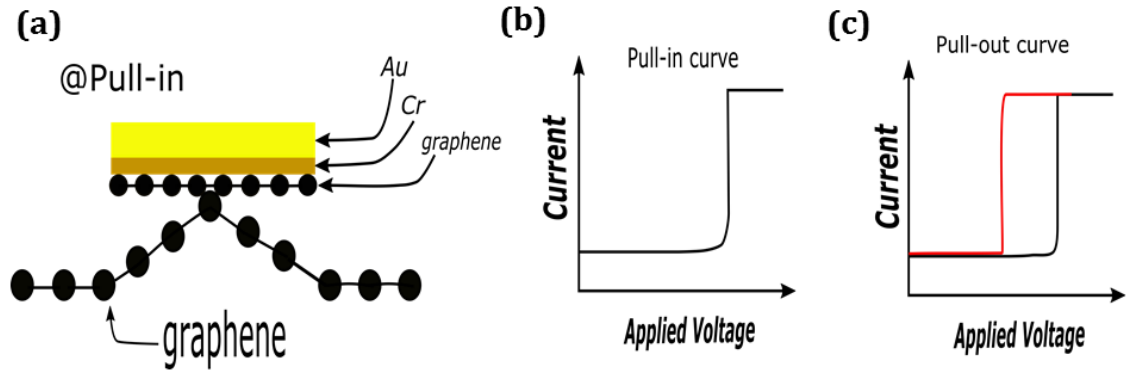


Figure 6.18. Surface adhesion in the graphene-graphene surface. (a) Graphene beam is pulled onto the surface of the graphene. (b) Pull-in characteristics of the NEM contact switch with graphene as contact material. (b) Typical pull out characteristics of the pull-out in the NEM contact switch with graphene as the contact material.

The Figure 6.10 illustrates the graphene NEM contact switch with graphene as the contact material. The Figure 6.10a shows the pull-in condition of the graphene NEM contact switch, in which the graphene beam is pulled onto the surface of the graphene. The Figure 6.10b shows the pull-in curve of the graphene NEM contact switch with graphene as the contact material. The Figure 6.10b shows the pull-out curve of the graphene NEM contact switch with graphene as the contact material. In graphene-to-graphene NEM contact switch the clear pull-out was observed. This is attributed to the low surface adhesion between the two graphene layers. This may be due to the van der Waals force between the graphene-to-graphene contacts. The van der Waals force equation is shown below.

$$F_{vdW} = -\frac{A_H * S_C}{6\pi d^3}$$

A_H is Hamaker constant, S_C is Contact area, and d is the distance between the two surfaces. The separation distance between the graphene-to-graphene layers obtained from the static graphene-to-graphene contact analysis, which is found to be 0.5 nm. The calculated van der Waals force between the graphene-to-graphene contacts is 42 nN. The restoring force double clamped graphene beam is 257 nN, which is higher than the van der Waals force between the graphene-to-graphene contacts. Owing to this high restoring force the graphene beam, the clear pull-in was achieved in graphene-to-

graphene NEM contact switches. This is the origin of the clear pull-out in the graphene-to-graphene NEM contact switches.

6.4 CHAPTER SUMMARY

This chapter summarizes the electrical characterization of the graphene-to-graphene NEM contact switches. Two terminal configurations were used to obtain the switching characteristics of the graphene-to-graphene NEM contact switches. Low pull-in voltage of <2.2 V, with a steep switching slope of <10 mV/dec and excellent reliability is demonstrated. Graphene layer as the contact material significantly reduces the surface adhesion force, which subsequently leads to low potential energy barrier between the suspended graphene beam and the contact graphene beam. The fabricated switches show stiction free switching characteristics owing to low energy barrier between the graphene layers.

7 Conclusion and Future Works

7.1 CONCLUSION

In this thesis, I have demonstrated the study of graphene-to-graphene NEM contact switches from fabrication to device characterization. First of all, graphene NEM switches with graphene as the contact material was introduced. The CVD grown graphene was used to fabricate the graphene-to-graphene NEM contact switches. All the fabricated switches were double clamped resonator type. The suspended graphene ribbon was fabricated using the high resolution positive tone PMMA resist. The contact graphene was achieved by transferring the another layer of the CVD graphene. The wet chemical based transferring technique was used to transfer the CVD graphene from the copper foil. All the fabricated devices were graphene nanoribbons (GNR) device with a local top gate. Also, the graphene-to-graphene crossbar device was fabricated using the high resolution negative tone HSQ resist.

Using the graphene-to-graphene crossbar device, the interlayer properties of the two rotated graphene layer was studied. The rotation angle between the two graphene layer and the bottom graphene layer was identified using the Raman spectroscopy. The rotation angle between the top and bottom layer is ~ 10 degree (θ). The in-situ annealing measurement was performed for the graphene-to-graphene interlayer crossbar device. We measured the interlayer transport properties of the twisted bilayer graphene using four-probe method. The clear saturation of the interlayer resistance at the low temperature is the strong observation of the incoherent conduction between the graphene-to-graphene interlayer. The interlayer tunnelling between two graphene layers follows the Metal-Insulator-Metal (MIM) tunnelling model. More interestingly, we

found that the interlayer tunnelling resistance changes significantly after the in-situ annealing. After the in-situ annealing, the interlayer resistance reduced to 0.8 k Ω from 4.8 k Ω at 5 K. The interlayer layer distance two graphene layers changed after the in-situ annealing, in other words the tunnelling length between the bottom and top graphene layer is reduced. In addition, we also studied the effect of the gas molecules intercalation on the interlayer transport. We have used Ar+H₂ (with hydrogen 10%) as the gas environment. We found that the interlayer resistance increases in the hydrogen gas environment from 650 Ω to 800 Ω at 130 K. This is attributed to the hydrogen intercalation between top and bottom graphene layers, which increased the effective interlayer distance. As a summary, the incoherent charge conduction between the upper and the lower graphene layers was observed and the interlayer tunnelling is the main conduction mechanism between the top and the bottom graphene layers at low temperature. At high temperatures, the interlayer conduction is mediated by the phonons.

The fabricated graphene-to-graphene NEM contact switches showed clear switching characteristics. The graphene-to-graphene NEM contact switch with pull-in voltage as low as ~ 1 V was demonstrated. The fabricated switches also exhibit the high on/off ratio as high as $\sim 10^5$ orders of magnitude with steep switching slope ~ 10 mV/dec. The NEM contact switches are shows stable on current (200 nA). Moreover, all the graphene-to-graphene NEM contact switches have demonstrated the low leakage, in the range of Pico amperes. Furthermore, the graphene-to-graphene NEM contact switches show very steep pull-out characteristics, which is a signature of stiction free switching operation. Owing to the atomically smooth contact between the suspended graphene layer and the contact graphene layer, the stiction was significantly reduced. The GNEM switches were successfully operated more than 15 switching cycles for the first time.

Future works

The contact resistance between the two graphene layers has to be studied using the graphene-to-graphene NEM contact switches. To achieve the high reliability of the graphene based NEM switches, the new structural design has to be introduced and further experimental works have to be done. Based on these two-terminal Graphene NEM switches, three-terminal graphene NEM switching device can be developed. This switch will have significant advantages for the conventional CMOS technology to reduce the off-state leakage current.

8 References

- [1] G. E. Moore, “Cramming more components onto integrated circuits, Reprinted from *Electronics*, volume 38, number 8, April 19, 1965, pp.114 ff.,” *IEEE Solid-State Circuits Soc. Newsl.*, vol. 11, no. 5, pp. 33–35, Sep. 2006.
- [2] W. Haensch *et al.*, “Silicon CMOS devices beyond scaling,” *IBM J. Res. Dev.*, vol. 50, no. 4.5, pp. 339–361, Jul. 2006.
- [3] G. Baccarani, M. R. Wordeman, and R. H. Dennard, “Generalized scaling theory and its application to a #188; micrometer MOSFET design,” *IEEE Trans. Electron Devices*, vol. 31, no. 4, pp. 452–462, Apr. 1984.
- [4] S. Deleonibus, “The Energy and Variability Efficient Era (E.V.E.) is Ahead of Us,” *IEEE J. Electron Devices Soc.*, vol. 4, no. 5, pp. 236–245, Sep. 2016.
- [5] P. Avouris and J. Chen, “Nanotube electronics and optoelectronics,” *Mater. Today*, vol. 9, no. 10, pp. 46–54, Oct. 2006.
- [6] S. Deleonibus, “More moore and more than moore meeting for 3D,” in *2015 30th Symposium on Microelectronics Technology and Devices (SBMicro)*, 2015, pp. 1–4.
- [7] C. Thelander *et al.*, “Nanowire-based one-dimensional electronics,” *Mater. Today*, vol. 9, no. 10, pp. 28–35, Oct. 2006.
- [8] O. Y. Loh and H. D. Espinosa, “Nanoelectromechanical contact switches,” *Nat. Nanotechnol.*, vol. 7, no. 5, pp. 283–295, May 2012.
- [9] N. Abele, R. Fritschi, K. Boucart, F. Casset, P. Ancey, and A. M. Ionescu, “Suspended-gate MOSFET: bringing new MEMS functionality into solid-state MOS transistor,” in *IEEE International Electron Devices Meeting, 2005. IEDM Technical Digest.*, 2005, pp. 479–481.
- [10] Y.-H. Song and J.-B. Yoon, “Micro and Nanoelectromechanical Contact Switches for Logic, Memory, and Power Applications,” in *Nano Devices and Circuit Techniques for Low-Energy Applications and Energy Harvesting*, Springer, Dordrecht, 2016, pp. 65–117.
- [11] A. K. Geim and K. S. Novoselov, “The rise of graphene,” *Nat. Mater.*, vol. 6, no. 3, pp. 183–191, Mar. 2007.

- [12] A. H. Castro Neto, F. Guinea, N. M. R. Peres, K. S. Novoselov, and A. K. Geim, “The electronic properties of graphene,” *Rev. Mod. Phys.*, vol. 81, no. 1, pp. 109–162, Jan. 2009.
- [13] A. V. Rozhkov, A. O. Sboychakov, A. L. Rakhmanov, and F. Nori, “Electronic properties of graphene-based bilayer systems,” *Phys. Rep.*, vol. 648, pp. 1–104, Aug. 2016.
- [14] Y. Liang, X. Liang, Z. Zhang, W. Li, X. Huo, and L. Peng, “High mobility flexible graphene field-effect transistors and ambipolar radio-frequency circuits,” *Nanoscale*, vol. 7, no. 25, pp. 10954–10962, Jun. 2015.
- [15] R. Atif, I. Shyha, and F. Inam, “Mechanical, Thermal, and Electrical Properties of Graphene-Epoxy Nanocomposites—A Review,” *Polymers*, vol. 8, no. 8, p. 281, Aug. 2016.
- [16] R. Venkatasubramanian, S. K. Manohar, and P. T. Balsara, “NEM Relay-Based Sequential Logic Circuits for Low-Power Design,” *IEEE Trans. Nanotechnol.*, vol. 12, no. 3, pp. 386–398, May 2013.
- [17] S. Hourri, C. Poulain, A. Valentian, and H. Fanet, “Performance Limits of Nanoelectromechanical Switches (NEMS)-Based Adiabatic Logic Circuits,” *J. Low Power Electron. Appl.*, vol. 3, no. 4, pp. 368–384, Dec. 2013.
- [18] T. Ernst *et al.*, “High performance NEMS devices for sensing applications,” in *2015 45th European Solid State Device Research Conference (ESSDERC)*, 2015, pp. 31–35.
- [19] M. Li, H. X. Tang, and M. L. Roukes, “Ultra-sensitive NEMS-based cantilevers for sensing, scanned probe and very high-frequency applications,” *Nat. Nanotechnol.*, vol. 2, no. 2, pp. 114–120, Feb. 2007.
- [20] J.-H. Kim, Z. C. Y. Chen, S. Kwon, and J. Xiang, “Three-Terminal Nanoelectromechanical Field Effect Transistor with Abrupt Subthreshold Slope,” *Nano Lett.*, vol. 14, no. 3, pp. 1687–1691, Mar. 2014.
- [21] X. L. Feng, M. H. Matheny, C. A. Zorman, M. Mehregany, and M. L. Roukes, “Low Voltage Nanoelectromechanical Switches Based on Silicon Carbide Nanowires,” *Nano Lett.*, vol. 10, no. 8, pp. 2891–2896, Aug. 2010.
- [22] S. W. Lee *et al.*, “A Three-Terminal Carbon Nanorelay,” *Nano Lett.*, vol. 4, no. 10, pp. 2027–2030, Oct. 2004.
- [23] K. M. Milaninia, M. A. Baldo, A. Reina, and J. Kong, “All graphene electromechanical switch fabricated by chemical vapor deposition,” *Appl. Phys. Lett.*, vol. 95, no. 18, p. 183105, Nov. 2009.
- [24] S. M. Kim *et al.*, “Suspended few-layer graphene beam electromechanical switch with abrupt on-off characteristics and minimal leakage current,” *Appl. Phys. Lett.*, vol. 99, no. 2, p. 023103, Jul. 2011.
- [25] P. Li, Z. You, and T. Cui, “Graphene cantilever beams for nano switches,” *Appl. Phys. Lett.*, vol. 101, no. 9, p. 093111, Aug. 2012.
- [26] J. Sun, W. Wang, M. Muruganathan, and H. Mizuta, “Low pull-in voltage graphene electromechanical switch fabricated with a polymer sacrificial spacer,” *Appl. Phys. Lett.*, vol. 105, no. 3, p. 033103, Jul. 2014.
- [27] “Study of dynamic contacts for graphene nano-electromechanical switches,” *Jpn. J. Appl. Phys.*, vol. 56, no. 4S, p. 04CK05, Mar. 2017.

- [28] J. Yaung, L. Hutin, J. Jeon, and T. J. K. Liu, “Adhesive Force Characterization for MEM Logic Relays With Sub-Micron Contacting Regions,” *J. Microelectromechanical Syst.*, vol. 23, no. 1, pp. 198–203, Feb. 2014.
- [29] F. Niroui *et al.*, “Controlled fabrication of nanoscale gaps using stiction,” in *2015 28th IEEE International Conference on Micro Electro Mechanical Systems (MEMS)*, 2015, pp. 85–88.
- [30] G. Palasantzas, P. J. van Zwol, and J. T. M. De Hosson, “Transition from Casimir to van der Waals force between macroscopic bodies,” *Appl. Phys. Lett.*, vol. 93, no. 12, p. 121912, Sep. 2008.
- [31] H. Dadgour, A. M. Cassell, and K. Banerjee, “Scaling and variability analysis of CNT-based NEMS devices and circuits with implications for process design,” in *2008 IEEE International Electron Devices Meeting*, 2008, pp. 1–4.
- [32] K. Akarvardar *et al.*, “Analytical Modeling of the Suspended-Gate FET and Design Insights for Digital Logic,” in *2007 65th Annual Device Research Conference*, 2007, pp. 103–104.
- [33] S. Chowdhury, M. Ahmadi, and W. C. Miller, “Pull-in voltage study of electrostatically actuated fixed-fixed beams using a VLSI on-chip interconnect capacitance model,” *J. Microelectromechanical Syst.*, vol. 15, no. 3, pp. 639–651, Jun. 2006.
- [34] S. Pamidighantam, R. Puers, K. Baert, and H. A. C. Tilmans, “Pull-in voltage analysis of electrostatically actuated beam structures with fixed–fixed and fixed–free end conditions,” *J. Micromechanics Microengineering*, vol. 12, no. 4, p. 458, 2002.
- [35] S. Chowdhury, M. Ahmadi, and W. C. Miller, “Pull-in voltage calculations for MEMS sensors with cantilevered beams,” in *The 3rd International IEEE-NEWCAS Conference, 2005.*, 2005, pp. 143–146.
- [36] *MEMS Linear and Nonlinear Statics and Dynamics | Mohammad I. Younis | Springer.*
- [37] A. H. Nayfeh, M. I. Younis, and E. M. Abdel-Rahman, “Dynamic pull-in phenomenon in MEMS resonators,” *Nonlinear Dyn.*, vol. 48, no. 1–2, pp. 153–163, Apr. 2007.
- [38] M. I. Younis, E. M. Abdel-Rahman, and A. Nayfeh, “A reduced-order model for electrically actuated microbeam-based MEMS,” *J. Microelectromechanical Syst.*, vol. 12, no. 5, pp. 672–680, Oct. 2003.
- [39] A. H. Nayfeh, M. I. Younis, and E. M. Abdel-Rahman, “Reduced-Order Models for MEMS Applications,” *Nonlinear Dyn.*, vol. 41, no. 1–3, pp. 211–236, Aug. 2005.
- [40] H. M. Ouakad and M. I. Younis, “The dynamic behavior of MEMS arch resonators actuated electrically,” *Int. J. Non-Linear Mech.*, vol. 45, no. 7, pp. 704–713, Sep. 2010.
- [41] S. Chakraborty, A. Bhattacharya, and T. K. Bhattacharyya, “Experimental analysis of pull-out voltage of electrostatically actuated microcantilever beam based on contact-stiction model,” *IET Micro Nano Lett.*, vol. 6, no. 1, pp. 43–47, Jan. 2011.

- [42] H. Kam and T. J. K. Liu, "Pull-In and Release Voltage Design for Nanoelectromechanical Field-Effect Transistors," *IEEE Trans. Electron Devices*, vol. 56, no. 12, pp. 3072–3082, Dec. 2009.
- [43] E. Sifakis and J. Barbic, *Finite Element Method Simulation of 3D Deformable Solids*. Morgan & Claypool Publishers, 2015.
- [44] J. J. H. Miller, W. H. A. Schilders, and S. Wang, "Application of finite element methods to the simulation of semiconductor devices," *Rep. Prog. Phys.*, vol. 62, no. 3, p. 277, 1999.
- [45] X. Tang, Z. Chen, Y. Li, Z. Hu, and Y. Yang, "Theoretical analysis and finite element method simulations on dynamic sensitivity of hemisphere-shaped electrostatic sensors," *Adv. Mech. Eng.*, vol. 8, no. 8, p. 1687814016665050, Aug. 2016.
- [46] P. Li, Z. You, G. Haugstad, and T. Cui, "Graphene fixed-end beam arrays based on mechanical exfoliation," *Appl. Phys. Lett.*, vol. 98, no. 25, p. 253105, Jun. 2011.
- [47] X. Liu *et al.*, "Large Arrays and Properties of 3-Terminal Graphene Nanoelectromechanical Switches," *Adv. Mater.*, vol. 26, no. 10, pp. 1571–1576, Mar. 2014.
- [48] J. Sun, M. E. Schmidt, M. Muruganathan, H. M. H. Chong, and H. Mizuta, "Large-scale nanoelectromechanical switches based on directly deposited nanocrystalline graphene on insulating substrates," *Nanoscale*, vol. 8, no. 12, pp. 6659–6665, Mar. 2016.
- [49] M. E. Schmidt, C. Xu, M. Cooke, H. Mizuta, and H. M. H. Chong, "Metal-free plasma-enhanced chemical vapor deposition of large area nanocrystalline graphene," *Mater. Res. Express*, vol. 1, no. 2, p. 025031, 2014.
- [50] J. Wu and Y. Wei, "Grain misorientation and grain-boundary rotation dependent mechanical properties in polycrystalline graphene," *J. Mech. Phys. Solids*, vol. 61, no. 6, pp. 1421–1432, Jun. 2013.
- [51] Z. Song, V. I. Artyukhov, B. I. Yakobson, and Z. Xu, "Pseudo Hall–Petch Strength Reduction in Polycrystalline Graphene," *Nano Lett.*, vol. 13, no. 4, pp. 1829–1833, Apr. 2013.
- [52] Y. Wei, J. Wu, H. Yin, X. Shi, R. Yang, and M. Dresselhaus, "The nature of strength enhancement and weakening by pentagon–heptagon defects in graphene," *Nat. Mater.*, vol. 11, no. 9, pp. 759–763, Sep. 2012.
- [53] Z. Yang, Y. Huang, F. Ma, Y. Sun, K. Xu, and P. K. Chu, "Size-dependent deformation behavior of nanocrystalline graphene sheets," *Mater. Sci. Eng. B*, vol. 198, pp. 95–101, Aug. 2015.
- [54] T. Zhang, X. Li, S. Kadkhodaei, and H. Gao, "Flaw Insensitive Fracture in Nanocrystalline Graphene," *Nano Lett.*, vol. 12, no. 9, pp. 4605–4610, Sep. 2012.
- [55] A. Shekhawat and R. O. Ritchie, "Toughness and strength of nanocrystalline graphene," *Nat. Commun.*, vol. 7, p. ncomms10546, Jan. 2016.
- [56] I. W. Frank, D. M. Tanenbaum, A. M. van der Zande, and P. L. McEuen, "Mechanical properties of suspended graphene sheets," *J. Vac. Sci. Technol. B Microelectron. Nanometer Struct. Process. Meas. Phenom.*, vol. 25, no. 6, pp. 2558–2561, Nov. 2007.

- [57] W.-M. Zhang, H. Yan, Z.-K. Peng, and G. Meng, “Electrostatic pull-in instability in MEMS/NEMS: A review,” *Sens. Actuators Phys.*, vol. 214, pp. 187–218, Aug. 2014.
- [58] D. H. Kim, M. W. Kim, J. W. Jeon, K. S. Lim, and J. B. Yoon, “Mechanical Reliability of a Digital Micromirror With Interdigitated Cantilevers,” *J. Microelectromechanical Syst.*, vol. 19, no. 5, pp. 1197–1206, Oct. 2010.
- [59] G. Boldeiu, D. Vasilache, V. Moagar, A. Stefanescu, and G. Ciuprina, “Study of the von Mises stress in RF MEMS switch anchors,” in *2015 International Semiconductor Conference (CAS)*, 2015, pp. 219–222.
- [60] P. N. Kambali and A. K. Pandey, “Capacitance and Force Computation Due to Direct and Fringing Effects in MEMS/NEMS Arrays,” *IEEE Sens. J.*, vol. 16, no. 2, pp. 375–382, Jan. 2016.
- [61] S. Dai, Y. Xiang, and D. J. Srolovitz, “Twisted Bilayer Graphene: Moiré with a Twist,” *Nano Lett.*, vol. 16, no. 9, pp. 5923–5927, Sep. 2016.
- [62] R. Bistritzer and A. H. MacDonald, “Transport between twisted graphene layers,” *Phys. Rev. B*, vol. 81, no. 24, p. 245412, Jun. 2010.
- [63] X. Li, K. M. Borysenko, M. B. Nardelli, and K. W. Kim, “Electron transport properties of bilayer graphene,” *Phys. Rev. B*, vol. 84, no. 19, p. 195453, Nov. 2011.
- [64] W. J. Wattamaniuk, J. P. Tidman, and R. F. Frindt, “Tunneling Conductivity in $\text{Hf-Ta}_{\text{S}}_{\text{2}}$,” *Phys. Rev. Lett.*, vol. 35, no. 1, pp. 62–65, Jul. 1975.
- [65] S. Coh, L. Z. Tan, S. G. Louie, and M. L. Cohen, “Theory of the Raman spectrum of rotated double-layer graphene,” *Phys. Rev. B*, vol. 88, no. 16, p. 165431, Oct. 2013.
- [66] R. W. Havener, H. Zhuang, L. Brown, R. G. Hennig, and J. Park, “Angle-Resolved Raman Imaging of Interlayer Rotations and Interactions in Twisted Bilayer Graphene,” *Nano Lett.*, vol. 12, no. 6, pp. 3162–3167, Jun. 2012.
- [67] J. M. Pomeroy and H. Grube, “‘Negative resistance’ errors in four-point measurements of tunnel junctions and other crossed-wire devices,” *J. Appl. Phys.*, vol. 105, no. 9, p. 094503, May 2009.
- [68] “Hydrogen intercalation: An approach to eliminate silicon dioxide substrate doping to graphene,” *Appl. Phys. Express*, vol. 8, no. 1, p. 015101, Dec. 2014.
- [69] T. Iwasaki, M. Muruganathan, M. E. Schmidt, and H. Mizuta, “Partial hydrogenation induced interaction in a graphene–SiO₂ interface: irreversible modulation of device characteristics,” *Nanoscale*, vol. 9, no. 4, pp. 1662–1669, Jan. 2017.
- [70] J.-H. Chen, C. Jang, S. Adam, M. S. Fuhrer, E. D. Williams, and M. Ishigami, “Charged-impurity scattering in graphene,” *Nat. Phys.*, vol. 4, no. 5, pp. 377–381, May 2008.
- [71] Y. Kim *et al.*, “Breakdown of the Interlayer Coherence in Twisted Bilayer Graphene,” *Phys. Rev. Lett.*, vol. 110, no. 9, p. 096602, Feb. 2013.
- [72] Y. Kim *et al.*, “Broken-Symmetry Quantum Hall States in Twisted Bilayer Graphene,” *Sci. Rep.*, vol. 6, p. srep38068, Dec. 2016.

- [73] I. V. Lebedeva, A. V. Lebedev, A. M. Popov, and A. A. Knizhnik, “Dislocations in stacking and commensurate-incommensurate phase transition in bilayer graphene and hexagonal boron nitride,” *Phys. Rev. B*, vol. 93, no. 23, p. 235414, Jun. 2016.